INFORMATION TO USERS

This manuscript has been reproduced from the microfilm master. UMI films the text directly from the original or copy submitted. Thus, some thesis and dissertation copies are in typewriter face, while others may be from any type of computer printer.

The quality of this reproduction is dependent upon the quality of the copy submitted. Broken or indistinct print, colored or poor quality illustrations and photographs, print bleedthrough, substandard margins, and improper alignment can adversely affect reproduction.

In the unlikely event that the author did not send UMI a complete manuscript and there are missing pages, these will be noted. Also, if unauthorized copyright material had to be removed, a note will indicate the deletion.

Oversize materials (e.g., maps, drawings, charts) are reproduced by sectioning the original, beginning at the upper left-hand corner and continuing from left to right in equal sections with small overlaps. Each original is also photographed in one exposure and is included in reduced form at the back of the book.

Photographs included in the original manuscript have been reproduced xerographically in this copy. Higher quality 6" x 9" black and white photographic prints are available for any photographs or illustrations appearing in this copy for an additional charge. Contact UMI directly to order.

UMI

A Bell & Howell Information Company
300 North Zeeb Road, Ann Arbor MI 48106-1346 USA
313/761-4700 800/521-0600

Molecular Beam Laser Stark Spectroscopy of Highly Vibrationally Excited Molecules

by

Marcell Stoer
B.Sc., University of Waterloo, 1989
M.Sc., University of Waterloo, 1991

A Thesis Submitted in Partial Fulfillment of the
Requirements for the Degree of
DOCTOR OF PHILOSOPHY
in the
Department of Chemistry

We accept this thesis as conforming
to the required standard

Dr. T. E. Gough, Supervisor (Department of Chemistry)

Dr. W. J. Balfour, Departmental Member (Department of Chemistry)

Dr. D. A. Harrington, Departmental Member (Department of Chemistry)

Dr. J. M. Roney, Outside Member (Department of Physics & Astronomy)

Dr. M. C. L. Gerry, External Examiner
(Department of Chemistry, University of British Columbia)

University of Victoria

Supervisor: Dr. T.E. Gough

Abstract

The Stark field perturbed spectra of near infrared vibrational overtones of hydrogen fluoride and acetylene have been measured with a high resolution molecular beam laser spectrometer. A high performance laser power build-up cavity (optical resonator) was constructed to measured the weak ro-vibrational transitions of the $\nu_2+3\nu_3$ vibrational combination band of acetylene. The measured gain of the build-up cavity was found to be at least 300 out of a potential 2000. The primary reason for the lower than expected gain was attributed to losses induced by the extreme heat build-up on the mirror surfaces.

The electric dipole moment for the $v = 3$ vibrational overtone of hydrogen fluoride was determined to be 1.9614 ± 0.0021 Debye. This result was compared with predictions from the available theoretical models and some theoretical constants were revised based on the current contribution to dipole moment function of hydrogen fluoride.

The Stark field perturbed spectra of the $\nu_1 + 3\nu_3$ and $\nu_2 + 3\nu_3$ vibrational combination bands of acetylene were analysed for their polarisability tensors. In order to complete the study, the ground electronic state static polarisability and anisotropy of the polarisability were also determined. They were found to be 3.96Å^3 and $1.071 \pm 0.014 \text{Å}^3$, respectively. The $|1030^00^0\rangle$ state ($\nu_1 + 3\nu_3$) was observed to be coupled with the $|0040^00^0\rangle$ infrared forbidden state ($4\nu_3$) in the presence of the Stark electric field. The resultant analysis produced values of $4.62 \pm 0.09 Å^3$ for the polarisability and $1.15 \pm 0.03 Å^3$ for the polarisability anisotropy of the $|1030^00^0\rangle$ state. The difference in energy between $|1030^00^0\rangle$ and $|0040^00^0\rangle$ was determined to be 4.133 cm^{-1}, which compares well with local mode calculations.

The measurements of the $\nu_2 + 3\nu_3$ band indicated that the $|0130^00^0\rangle$ state was strongly coupled with another infrared allowed, unidentified (*rogue*), state in the absence of the Stark field as well as with the infrared forbidden, $|1120^00^0\rangle$ state in the presence of the Stark field. The previously unobserved $J = 5 \leftarrow 4$ transition of the infrared allowed *rogue* state was recorded here for the first time. The Stark field perturbed spectra of the R(3) and R(5) ro-vibrational transitions of the $\nu_2 + 3\nu_3$ band also showed evidence of *rogue* transitions. The ensuing analysis determined that the $|0130^00^0\rangle$ state has a polarisability of $3.5 \pm 0.3 Å^3$ and a polarisability anisotropy of $5.6 \pm 1.8 Å^3$. The Stark field perturbed spectra of the R(3) and R(5) transitions were fit to a non-crossing model and the energy levels of the *rogue* $J = 4$ and $J = 6$ states were determined. The energy level difference between $|0130^00^0\rangle$ and $|1120^00^0\rangle$ was determined to be -11.88 ± 0.22 cm^{-1}. This does not compare well with local mode calculations and it is possible that the perturbations due to the presence of the *rogue* state impeded the accurate determination of the energy level difference. The identity of the *rogue* vibrational state could not be determined from the data presented in this thesis alone. However, collaborative work with another research group suggests that the *rogue* vibrational state is $|0306^03^1\rangle$ (see Chapter 7).

Examiners:

Dr. T. E. Gough, Supervisor (Department of Chemistry)

Dr. W. J. Balfour, Departmental Member (Department of Chemistry)

Dr. D. A. Harrington, Departmental Member (Department of Chemistry)

Dr. J. M. Roney, Outside Member (Department of Physics & Astronomy)

Dr. M. C. L. Gerry, External Examiner
(Department of Chemistry, University of British Columbia)

Table of Contents

List of Tables

List of Figures

Acknowledgements

First of all I would like to thank all of the Chemistry department support staff, without whom it would not be possible to complete any research project. Dick Robinson and Roy Bennett in the Machine Shop have often dropped everything to fix an ailing pump or piece of other equipment requiring emergency care. I know they especially enjoyed machining the Stark electrode spacers from, supposedly, machinable ceramic. Dave Searle, who retired from the Glass Shop a couple of years ago, was always ready to let me tinker around trying to polish a mirror or make anything out of glass, regardless whether it should be or not. Thanks also goes to the Instrument Shop, where Terry Wiley and Bob Dean many times had to fix electronic instruments we managed to incapacitate with a high voltage discharge or two ("Aren't those chips suppose act as fuses?"). Dave Smith and Peter Ward of the Physics & Astronomy department Machine Shop were always very helpful when I tried to machine something myself in the Physics & Astronomy department Machine shop.

I would like to thank my co-graduate students and good friends, Marko Banjavčić, Terry Rowat and Tangyu Wang. Terry Rowat (MSc) and Tangyu Wang (PhD) have graduated in the mean time, I don't blame them. Tangyu forever kept me on my toes, insisting the solution to any problem be kept as simple as possible. His "simple physics" motto, apparently gave him the knack for keeping the computer tied up in seemingly endless FORTRAN calculations. I am thankful to Marko for the numerous times he helped me debug my data collection software and the many, many times

he listened to the latest list of ailments troubling the beam machine/build-up cavity experiments. I have been incredibly fortunate to have Dr. Jack Barnes as a co-worker. Jack seems to be capable of doing just about anything, from designing electronic circuits and machining the most intricate parts, to making sense of all the strange but interesting data we accumulated. In many ways, this thesis is as much his as it is mine. I am very grateful for having Professor Terry Gough as a supervisor. Terry has always allowed me the freedom to try almost anything, which is what has made science exciting for me. He has also taught me to always begin with the simplest measurement that can be done, work my way up from there and let the picture develop on its own. I believe this was a very valuable lesson.

Finally I would like to thank my wife, Felisa, for helping me keep my spirits up during those many times when the project seemed to come to a near standstill. Those frustrating times often proved to be more of a challenge than the science itself.

To my parents

Chapter 1

Introduction

1.1 Vibrational Overtones

In the past decade or so there has been a renewed interest in the spectroscopy of highly vibrationally excited molecules [1]. This may have been in part driven by the fact that a great number of chemical processes (atmospheric chemistry, combustion, chemical lasers and many other chemical reactions) are fueled by highly excited molecules. While it is desirable to study the larger molecules ($\geq$ 12 atoms) that typically partake in most chemical reactions, it is not possible to conduct a thorough investigation of their spectroscopy. For one, the lack of rotationally resolvable spectra makes the determination of changes in geometry with increased excitation difficult; this is an important feature in determining the potentials governing bond dissociation. Smaller molecules (three or four atoms) produce spectra that can easily be fully resolved with today's high resolution instruments and they often contain some of the complexities of the larger polyatomics [2]. Yet their small size makes them amenable to modelling by *ab initio* computations. This allows the validity of the theoretical models to be tested, in order to provide a better approximation for more complex systems.

A typical Arrhenius activation energy (100-250 kJ/mol) corresponds to about 8360—21000 cm^{-1}, or about 3-5 quanta of vibrational excitation for many small molecules. The near infrared region of the spectrum (8000–13000 cm^{-1}) where many of these excited vibrational states lie, has been the subject of comprehensive investigations even as long as 60 years ago [3]. The at the time, long path length, Doppler limited, studies appeared complete in that they seemed to have measured all that was detectable for the molecules under scrutiny. The advent of high resolution lasers has allowed the vibrational overtone region of the spectrum to be re-examined. Most notably, intra-laser-cavity photoacoustic spectroscopy has revolutionised the measurement of these weakly absorbing states. The high power per spectral bandwidth available inside the cavity of a laser has virtually eliminated the need for long path length cells, resulting in numerous studies based upon this new technique [4–9]. These experiments have contributed greatly to our understanding of highly excited vibrational states and have offered many new challenges to the theories used to describe them [2]. The development of a model that can accurately predict the behaviour of a molecule at all levels of vibrational excitation has, however, been somewhat elusive.

Describing the vibrations of a molecule has been traditionally left to normal mode theory. The vibrations in the molecule are approximated as harmonic oscillators and the concerted motion of these oscillators is then reduced to the fundamental vibrational modes. These modes form a complete basis set and are therefore termed "normal modes" [3]. At low excitation energies this approximation has proven to be a good one. The bottom of the potential energy curve for a vibrational mode is well described by a harmonic oscillator potential. Vibrational overtones, not allowed under the harmonic oscillator approximation, owe their existence to anharmonicity and at higher excitation energies the anharmonicity of the vibrational motion becomes much more apparent. This can clearly be seen from the fact that, given sufficient energy, the bond can dissociate, a behaviour not predicted by harmonic oscillator theory. Further, the Hamiltonian describing these high vibrational excitations becomes increasingly off-diagonal, indicating extensive coupling among the normal modes. One result of this coupling is the existence of combination bands, which have one or more quanta in two or more different normal modes. As the amount of vibrational excitation is increased, it becomes increasingly cumbersome to describe these states via normal mode theory.

A new theory was devised which is based upon the localised behaviour of the vibrations at these high excitation frequencies [10]. As the vibrational excitation of the molecule is increased, it appears that single bonds are vibrating rather than oscillating in unison to form the normal modes described earlier. The symmetric and antisymmetric C-H stretching vibrations of benzene are good examples of this localised behaviour. At higher levels of vibrational excitation there is an increase in normal mode coupling, which in turn requires an increased number of anharmonicity constants to accurately describe the spectrum [10]. If, however, a harmonic oscillator description is used vibrational levels can be described quite accurately with only two parameters. Figure 1.1 depicts the observed band centres (ν_{obs}) for the C-H stretching vibrations of benzene from 3000 cm^{-1} to 24000 cm^{-1} [5]. The solid line is a fit to the two parameter local mode expression [5, 10]

$$\nu_{\mathrm{obs}} = n[\omega - \omega x\,(n + 1)] \;, \tag{1.1}$$

where ω is the harmonic vibrational frequency, ωx is the anharmonic vibrational constant and n is the number of C-H stretch quanta. Child and Halonen have carried out local mode calculations on several different X-H systems to demonstrate the effectiveness of this model [11].

In a similar fashion Mecke and Ziegler already introduced a bond mode type model to predict the behaviour of the highly vibrationally excited states of acetylene in 1936 [12]. However, it was not until much more recently that the interest in the bond mode theory has been rekindled [10, 13, 14]. The need to understand the apparently simple vibrational overtone spectra of benzene and similar molecules whose overtone spectrum is dominated by the C–H stretching progression has given this bond mode or "local mode" theory new life and it has been very successful in describing these highly excited states [15–17]. The natural extension of this local mode

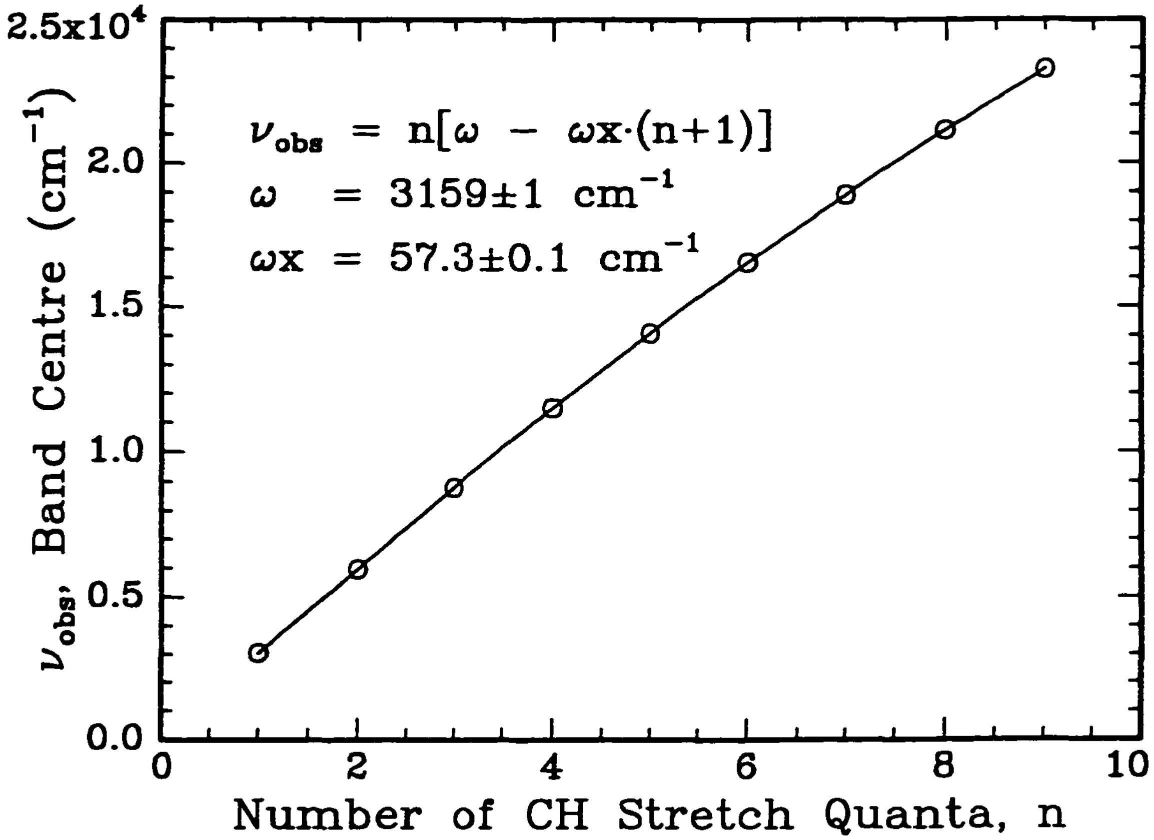

Figure 1.1: The observed band centres ν_{obs} of the benzene C-H stretching vibrations are plotted against the number of C-H stretching quanta (n). The data were taken from reference [5] and is depicted by the circles. The solid line is a fit to the local mode Equation 1.1 [5, 10].

behaviour is to attempt bond selective chemistry. By selectively energising a particular bond, the desired reaction outcome would be enhanced, or so was the thought. However, the bond energised is seldom the one which breaks [13, 14, 18]. The supplied vibrational energy randomises among other vibrational modes on a time scale too fast for bond selective chemistry to take place. The deceptively simple overtone spectra of these molecules lead one to believe that this region of the spectrum is relatively uncongested. In reality there are a great number of states present, but only a few have transitions with sufficient oscillator strength to be detected. These "bath" states draw their intensity from the more easily measurable infrared "bright" state, providing a channel for intramolecular vibrational relaxation (IVR) [14]. In order to understand the dynamics of the highly excited vibrational states it is important to conduct experiments that not only have the sensitivity to probe these weakly absorbing states, but are also able to fully resolve their ro-vibrational structure. Only then can advances of photochemical significance be made.

The ability to obtain high resolution spectra of vibrational overtones allows the precise measurement of a molecule's electrical properties at geometries other than the molecule's equilibrium geometry. The Stark effect has long been used to study the interaction of atoms and molecules with external electric fields. The target of many of these experiments has been the measurement of electric dipole moments and polarisability tensors in the ground and first excited vibrational states [19]. These parameters not only describe how the electronic structure varies with geometry, but form the fundamental basis for the understanding and prediction of molecular interactions [20,21]. Hence, it is important to have the broadest knowledge possible of their behaviour at increasing levels of vibrational excitation [22,23]. Stark field induced shifts and splittings of energy levels are often very small when compared to the Doppler broadened line widths of typical gas phase ro-vibrational transitions [24,25] and the most accurate measurements can only be made with high resolution laser molecular beam experiments [26].

In regions of high state density, such as the near infrared for small molecules, the Stark effect may provide another avenue for study by allowing states to interact in the presence of a static external electric field. The interaction of closely spaced levels is well documented in spectroscopy [27–29]. Fermi resonances in infrared spectra are perhaps some of the most common. Careful analysis of the spectra can provide information regarding the strength of the interaction, the identity of the interacting states and their relative positions. However, due to the lack of control over the strength of the perturbation it is not always possible to extract as much information as one would like. Inducing the perturbation with an external electric field allows one to manipulate the strength of the perturbation by adjusting the magnitude of the applied field.

1.2 The Stark Effect

There are several detailed discussions of the Stark effect in the literature [19, 30–33]. The following description will generally be confined to the Stark effect for a linear molecule in a $^1\Sigma$ electronic state where the total angular momentum is due only to molecular rotation. The Hamiltonian for a molecule in an external static electric field can be expressed as

$$\mathcal{H} = \mathcal{H}^0 + \mathcal{H}_{\mathrm{Stark}} = \mathcal{H}^0 - \hat{\mu} \cdot \mathbf{F} \ , \tag{1.2}$$

where $\hat{\mu}$ is the electric dipole moment operator and $\mathbf{F}$ is the electric field vector. At high electric fields or if the molecule does not have a permanent electric dipole moment, $\hat{\mu}$ may be expanded in a Taylor series in terms of the field [31].

$$\hat{\mu} = \boldsymbol{\mu} + \underline{\alpha} \cdot \mathbf{F} + \frac{1}{2}\underline{\beta} \cdot \mathbf{F}^2 + \frac{1}{6}\underline{\gamma} \cdot \mathbf{F}^3 + \cdots \tag{1.3}$$

The permanent electric dipole moment vector along the molecular symmetry axis in absence of the electric field is $\boldsymbol{\mu}$, $\underline{\alpha}$ is the polarisability, and $\underline{\beta}$ and $\underline{\gamma}$ are the first and second hyperpolarisabilities. $\underline{\alpha}$, $\underline{\beta}$ and $\underline{\gamma}$ are tensor quantities of rank 2, 3 and 4, respectively. Of primary concern here are the terms containing $\boldsymbol{\mu}$ and $\underline{\alpha}$. The higher order terms, $\underline{\beta}$ and $\underline{\gamma}$, and terms involving field gradients (omitted for simplicity) are important to other optical processes, such as second order harmonic generation, the Faraday effect and other nonlinear phenomena [34]. These higher order terms are less significant when compared to the effects that result from the interaction of $\boldsymbol{\mu}$ and $\underline{\alpha}$

with a Stark electric field. The interaction of the electric field with $\boldsymbol{\mu}$ and $\underline{\alpha}$ will each be dealt with separately in the following two sections.

1.2.1 The Electric Dipole Moment

The quantum mechanical treatment of the effect of a external electric field on the motion of a molecule is usually approached with perturbation theory. For example, the energy of a symmetric top molecule in a uniform electric field (F) to second order is [19]

$$W_{JKM}(\mathbf{F}) = W^0_{JK} + W^{(1)}_{JKM}(\mathbf{F}) + W^{(2)}_{JKM}(\mathbf{F}) + \cdots , \tag{1.4}$$

where W^0_{JK} is the energy of the molecule in absence of the electric field and K is the projection of the rotational angular momentum, J, on the symmetry axis of the molecule. $W^{(1)}_{JKM}(\mathbf{F})$ and $W^{(2)}_{JKM}(\mathbf{F})$ are the first and second order perturbation corrections to the zero order energy (W^0_{JK}) due to the presence of the electric field. M is the projection of J along the electric field. The first order perturbation term can be evaluated by taking the average interaction energy as follows

$$\begin{aligned} W^{(1)}_{JKM}(\mathbf{F}) &= -\langle JKM|\boldsymbol{\mu}\cdot\mathbf{F}|JKM\rangle \\ &= -\mu F\langle JKM|\cos\theta|JKM\rangle , \end{aligned} \tag{1.5}$$

where θ is the angle between the permanent electric dipole moment (μ) and the electric field. The $\langle JKM|\cos\theta|JKM\rangle$ term can be evaluated by use of the direction cosine matrix elements. The motion of a molecule can be described in two distinct coordinate systems; one is body (molecule) fixed and the other is space (laboratory) fixed. The direction cosines relate the angular momentum components and their respective matrix elements in these two coordinate systems [35]. For $\boldsymbol{\mu}$ parallel to the molecular axis, z, and $\mathbf{F}$ along the space fixed Z direction, $\cos\theta$ is represented by the direction cosine matrix Φ_{Zz}. The elements of Φ_{Zz}, ϕ_{Zz}, are available in tabular form in many spectroscopy books (Table 4-4 in reference [30], for example). Upon consultation of one of these tables, Equation 1.5 can be re-written as

$$\begin{aligned} W^{(1)}_{JKM}(F) &= -\mu F \langle JKM|\Phi_{Zz}|JKM\rangle \\ &= -\mu F \phi_{JJ}\,\phi_{JK}\,\phi_{JM} \\ &= -\mu F \frac{MK}{J(J+1)} . \end{aligned} \tag{1.6}$$

For a linear molecule $K = 0$, since it does not have a component of angular momentum along the symmetry axis and the first order Stark effect vanishes. Symmetric top molecules with $K = 0$ also do not have a first order Stark effect. This then leads to the second order perturbation energy which is

$$W^{(2)}(F) = \sum_{J \neq J'} \frac{|\langle JKM|\boldsymbol{\mu}\cdot\mathbf{F}|J'KM\rangle|^2}{W^0_{JKM} - W^0_{J'KM}} \tag{1.7}$$

where the only non-zero direction cosine matrix elements come from $J' = J \pm 1$. In terms of the direction cosines, the above equation becomes

$$W^{(2)}(F) = \mu^2 F^2 \left[\frac{(\phi_{J;J+1}\, \phi_{J,K;J+1,K}\, \phi_{J,M;J+1,M})^2}{W^0_{JKM} - W^0_{J+1,KM}} + \frac{(\phi_{J;J-1}\, \phi_{J,K;J-1,K}\, \phi_{J,M;J-1,M})^2}{W^0_{JKM} - W^0_{J-1,KM}} \right] . \tag{1.8}$$

Once again, consulting tables of direction cosine matrix elements the result is

$$W^{(2)}(F) = \frac{\mu^2 F^2}{2hB} \left[\frac{(J^2 - K^2)(J^2 - M^2)}{J^3(2J+1)(2J-1)} - \frac{[(J+1)^2 - K^2][(J+1)^2 - M^2]}{(J+1)^3(2J+1)(2J+3)} \right] \tag{1.9}$$

which for a linear molecule ($K = 0$) simplifies to

$$W^{(2)}_{J,M}(F) = \frac{\mu_v^2 F^2}{2hB} \frac{J(J+1) - 3M^2}{J(J+1)(2J-1)(2J+3)} \tag{1.10}$$

where B is the rotational constant of the molecule. One of the first noticeable effects the Stark field has on the rotational spectrum of a molecule is the increase in the number of observable transitions. This is a direct result of the removal of the degeneracy of J, splitting the energy levels into $2J + 1$ (M_J) states. Figure 1.2 depicts a $J = 2 \leftarrow 1$ transition in the presence of a Stark field.

The selection rules for M arise during the development of the direction cosine matrix elements; non-zero matrix elements are produced only when $\Delta M = 0, \pm 1$ [35]. Figure 1.2 depicts both types of transitions, differentiating them by dashed and solid lines. As a rule of thumb, a $J + 1 \leftarrow J$ rotational transition may have $2J + 1$

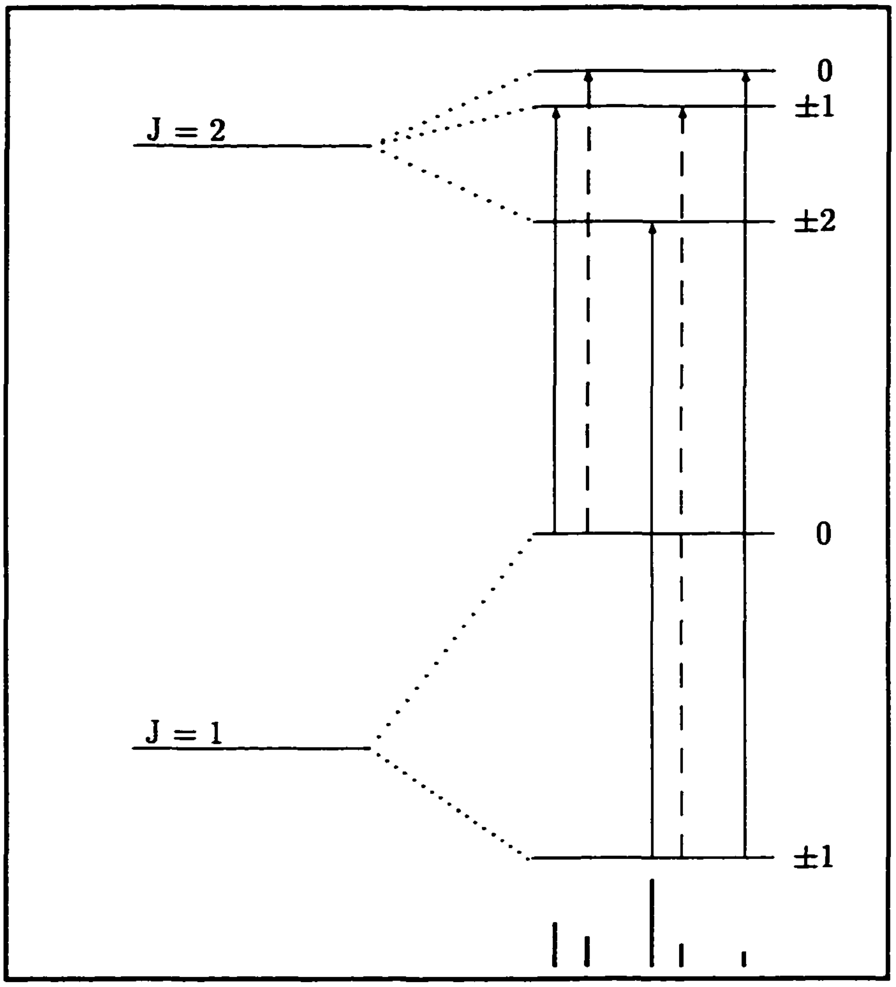

Figure 1.2: The second order Stark split energy levels of a $J = 2 \leftarrow 1$ transition of a linear molecule with a permanent electric dipole moment according to Equation 1.10. Each energy level is split into $2J+1$ M_J states. The dashed lines represent the two $\Delta M = 0$ transitions and the solid lines the three $\Delta M = \pm 1$ transitions. The $\Delta M = 0$ transitions are termed "parallel", while the $\Delta M = \pm 1$ transitions are called "perpendicular". Below the transitions is a "stick spectrum" of their relative intensities. From left to right, 6:4:12:3:2.

$\Delta M = \pm 1$ transitions and $J+1$ $\Delta M = 0$ transitions making a total of $3J+2$ possible transitions. Below the transitions depicted in Figure 1.2 is a "stick spectrum" of the relative intensities of these transitions. The relative intensities can readily be calculated from the direction cosine matrix elements and are often provided in tabular form (see Table 10-1, reference [30]). However, both parallel and perpendicular M transitions are not always observed. The intensities of the transitions are affected by the angle of the polarisation of the incident electromagnetic (laser) field relative to the Stark electric field. Remembering that M is the projection of J on the Z axis (direction of Stark field), consider the following. Classically, a laser field polarised in the Z direction cannot exert any torque about the Z axis, hence $\Delta \mathrm{M} = 0$. Rotating the laser polarisation 90° with respect to the Stark field would result in transitions with $\Delta \mathrm{M} = \pm 1$ and setting the laser electric field to be polarised 45° with respect the Z axis would result in an equal mixture of $\Delta \mathrm{M} = 0$ and $\Delta \mathrm{M} = \pm 1$ transitions.

For a linear molecule the higher *odd* order perturbation terms are zero [30]. The fourth order term for a linear molecule has been been evaluated by Muenter *et al.* [36],

$$\begin{aligned} W^{(4)}_{J,M}(F) &= \frac{\mu_v^4 F^4}{8h^3B^3}\left[-\frac{[(J+1)^2-M^2][(J+2)^2-M^2]}{(2J+1)(2J+5)(J+1)^2(2J+3)^3}\right. \\ &+ \frac{[(J-1)^2-M^2][J^2-M^2]}{(2J-3)(2J+1)J^2(2J-1)^3} + \frac{[J^2-M^2][(J+1)^2-M^2]}{(2J-1)(2J+3)(2J+1)^2J^2(J+1)^2} \\ &+ \left.\frac{[(J+1)^2-M^2]^2}{(2J+3)^2(2J+1)^2(J+1)^3} - \frac{[J^2-M^2]^2}{(2J+1)^2(2J-1)^2J^3}\right] . \end{aligned} \tag{1.11}$$

This term typically contributes much less than 0.5% of the Stark energy. For a diatomic molecule with an electric dipole moment of 2 Debye, a rotational constant of 20 cm^{-1} and an applied Stark Field of 40 kV/cm the fourth order Stark energy of the $(J, M) = (1, 0)$ energy level is 0.12 MHz, compared with the 270 MHz contributed by the second order term. In many cases the fourth order term can be neglected without any significant loss of accuracy of the desired constant. There is, however, a second order contribution from the polarisability of the molecule which is discussed in the next section.

1.2.2 The Electric Dipole Polarisability

A contribution to the Stark energy will also come from the polarisability ($\underline{\alpha}$) of a molecule. However, the polarisability is not a property that can be measured directly. The external electric field not only distorts the electron distribution in a molecule, it perturbs the entire molecule. This can be seen from the fact that a Stark field drives all allowed transitions off resonance. Hence, along with the electronic wavefunction, the vibrational and rotational wavefunctions have also been perturbed. In order to accurately describe the effect of a Stark field on a molecule, and measure the relevant electrical properties, all states (electronic, vibrational and rotational) that can interact with the electric field must be taken into consideration. Only states with an electric dipole allowed transition need be included in the sum over all ro-vibronic states approach, since only they provide a non-zero contribution [33].

The distortion of the charge distribution gives rise to an induced dipole moment

($\boldsymbol{\mu}_{\text{ind}} = \underline{\alpha} \cdot \mathbf{F}$) which can interact with the electric field, $\boldsymbol{\mu}_{\text{ind}} \cdot \mathbf{F}$. Classically, the energy of the system becomes

$$W = -\int \boldsymbol{\mu}_{\text{ind}} \, d\mathbf{F} = -\frac{1}{2}\underline{\alpha}\mathbf{F}^2 \,. \tag{1.12}$$

A quantum mechanical treatment using second order perturbation theory will give the correct $\mathbf{F}^2$ dependence and also take the perturbed motion of the electrons into account. The optical polarisability tensor for a molecule in state m is then [31]

$$\alpha^{(m)}_{\xi\eta}(\omega) = \sum_{k \neq m} \frac{2E_{km}}{E^2_{km} - (\hbar\omega)^2} \langle m|\mu_\xi|k\rangle\langle k|\mu_\eta|m\rangle \tag{1.13}$$

where ξ and η denote the tensor components, ω is the oscillation frequency of the electric field, E_{km} is the energy difference between states k and m and $\mu_{\xi \text{ or } \eta}$ is the dipole moment operator. The above sum is carried out over the entire set of intermediate states k (electronic, vibrational and rotational). $\alpha_{\xi\eta}(\omega)$ is known as the *dynamic* polarisability (discussed in more detail later) and setting $\omega = 0$ gives the *static* polarisability $\alpha_{\xi\eta}(0)$. To introduce a more compact notation, $\alpha_{\xi\eta}(\omega)$ will be written as $\underline{\alpha}(\omega)$ and $\alpha_{\xi\eta}(0)$ simply as $\underline{\alpha}$ when the individual tensor components need not be identified.

Static Polarisability

The Stark effect measures the static polarisability since the molecule is subjected to a static electric field. Setting $\omega = 0$ in Equation 1.13 results in

$$\alpha_{\xi\eta}^{(m)} = \sum_{k \neq m} \frac{2}{E_{km}} \langle m|\mu_\xi|k\rangle\langle k|\mu_\eta|m\rangle \,. \tag{1.14}$$

Often the second order perturbation energy is evaluated using a sum-over-states approach. In a sum-over-states methodology the polarisability for a given rovibronic state is comprised of contributions from other electronic states, from other vibrational states within the same electronic state and from other rotational states within the same vibrational state [33]. In a rigorous treatment, Brieger carried out this sum for a diatomic molecule [32]. Rather than using direction cosines to correlate the laboratory and molecule fixed frames, Brieger uses 3*j*-symbols which function in a manner similar to the direction cosines [37]. Brieger determined the second order correction to the Stark energy for a diatomic molecule to be [32]

$$W_{JKM}^{(2)}(F) = -\frac{1}{2}F^2 \sum_{J'} (2J'+1)(2J+1) \begin{bmatrix} J' & J & 1 \\ M & -M & 0 \end{bmatrix}^2 \left(\begin{bmatrix} J' & J & 1 \\ 0 & 0 & 0 \end{bmatrix}^2 \times \right.$$
$$\left. \{\alpha_{||}^{e}(J,J') + \alpha_{||}^{v}(J,J') + \alpha_{||}^{r}(J,J')\} + \begin{bmatrix} J' & J & 1 \\ -1 & 0 & 1 \end{bmatrix}^2 \alpha_{\perp}^{e}(J,J') \right) . \tag{1.15}$$

The $3j$-symbols are denoted by the "arrays", and $\alpha^e_{\parallel}(J,J')$, $\alpha^e_{\perp}(J,J')$, $\alpha^v_{\parallel}(J,J')$ and $\alpha^r_{\parallel}(J,J')$ are the electronic, vibrational and rotational *branch* polarisabilities. These branch polarisabilities arise from the various contributions to the polarisability taken into account by the sum-over-states method and are defined as follows :

$$\alpha^e_{\parallel}(J,J') = -\sum_{n'\neq n}\sum_{v'} \frac{2|\langle nv(J)|\mu_{\parallel}|n'v'(J')\rangle|^2}{E_{nvJ}-E_{n'v'J'}} \tag{1.16}$$

$$\alpha^e_{\perp}(J,J') = -\sum_{n'\neq n}\sum_{v'} \frac{2|\langle nv(J)|\mu_{\perp}|n'v'(J')\rangle|^2}{E_{nvJ}-E_{n'v'J'}} \tag{1.17}$$

$$\alpha^v_{\parallel}(J,J') = -\sum_{v'\neq v} \frac{2|\langle nv(J)|\mu_{\parallel}|nv'(J')\rangle|^2}{E_{nvJ}-E_{nv'J'}} \tag{1.18}$$

$$\alpha^r_{\parallel}(J,J') = -2\frac{|\langle nv(J)|\mu_{\parallel}|nv(J')\rangle|^2}{E_{nvJ}-E_{nvJ'}}\,, \tag{1.19}$$

where the n, v and J are the electronic, vibrational and rotational states in the summation, E_{nvJ} is the energy of the respective state and $\mu_{\parallel/\perp}$ is the component of the dipole moment operator connecting the corresponding parallel $(\Sigma-\Sigma)$ or perpendicular $(\Sigma-\Pi)$ transitions [32]. A polyatomic molecule will have an additional term [38]

$$\alpha^v_{\perp}(J,J') = -\sum_{v'\neq v} \frac{2|\langle nv(J)|\mu_{\perp}|nv'(J')\rangle|^2}{E_{nvJ}-E_{nv'J'}}\,, \tag{1.20}$$

which arises from perpendicular vibrational transitions. The rotational dependence of the energy denominators in Equations 1.16 and 1.17 is negligible in comparison to the electronic energies. The electronic branch polarisability differences due to different J' can therefore be ignored. This simplifies Equation 1.15 and the usual electronic contribution to the Stark energy results [31]

$$W_{JM}^{(2)}(F) = -\frac{1}{2}\alpha F^2 - \frac{J(J+1)-3M^2}{3(2J-1)(2J+3)}\Delta\alpha F^2 \,. \tag{1.21}$$

In this equation α ($= \frac{1}{3}[\alpha_{\parallel} + 2\alpha_{\perp}]$) is the mean or scalar polarisability and $\Delta\alpha$ ($= \alpha_{\parallel} - \alpha_{\perp}$) is the anisotropy of the polarisability. The polarisability has two "visible" effects on the energy levels. The first is to introduce an M independent shift and the second is to remove the $2J+1$ degeneracy. Linear symmetric polyatomic molecules can only exhibit a purely polarisability induced Stark field perturbed spectrum when the transitions involve more than one vibrational state. Figure 1.3 is an example of a $J = 2 \leftarrow 1$ transition between the ground vibrational state and an excited vibrational state (v') depicting only the $\Delta M = \pm 1$ transitions. The correction to the total Stark energy for a heteronuclear diatomic molecule due to the polarisability is much smaller than that generated by the dipole moment. For the example given earlier ($J = 1$, $M = 0$) the contribution for $\Delta\alpha = 1 \mathring{A}^3$ is 0.36 MHz, compared to 270 MHz and 0.12 MHz from the second and fourth order dipole moment contributions. However, since non-polar polyatomic molecules do not have a permanent electric dipole moment, the polarisability is the sole contributor to the Stark effect for these molecules. Typically high electric fields (greater than 100 kV/cm) must be used to be able to easily observe this effect and obtain accurate measurements of the static polarisability tensor.

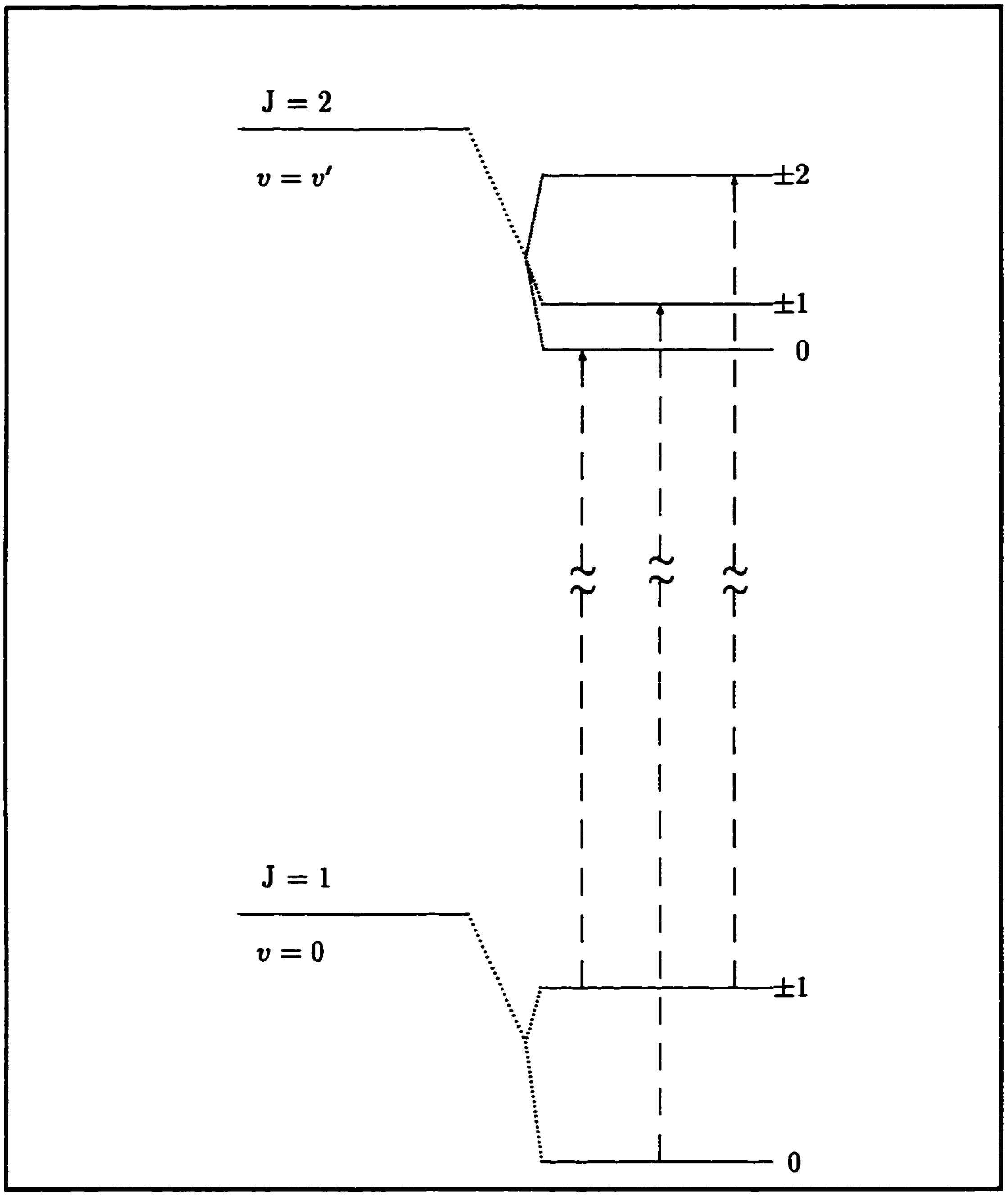

Figure 1.3: The second order Stark split energy levels of a $J = 2 \leftarrow 1$ transition of a linear symmetric polyatomic molecule according to Equation 1.21. Each energy level is split into $2J+1$ M_J states. The dashed lines represent the three $\Delta M = \pm 1$ transitions.

Dynamic Polarisability

An oscillating electric field, such as that of a laser, interacts with the dynamic polarisability. An example of this is the interaction of a beam of light of frequency ω with the molecules of a gas. This will induce a dipole proportional to $\underline{\alpha}$ oscillating at frequency ω. The oscillating dipole of each molecule emits radiation in a spherical scattered wave and the interference of the scattered waves of all molecules of the gas produces coherent and incoherent scattered light. The constructive interference results in a wave that is retarded in phase relative to the incident light beam and is responsible for refraction. Hence, refractive indices are a direct measure of the dynamic polarisability. Other phenomena, such as Raman and Rayleigh scattering also owe their existence to the dynamic polarisability. For a detailed discussion of the dynamic polarisability and related phenomena see references [31, 33, 39]. The present discussion will be limited to the difference in the determination of static polarisability by direct measurement (Stark effect) or by extrapolation from dynamic polarisabilities.

Just as the static polarisability was expressed as a sum of various electronic, vibrational and rotational contributions, the same approach can be employed for the dynamic polarisability, $\underline{\alpha}(\omega)$, [33]:

$$\underline{\alpha}(\omega) = \underline{\alpha}^{e}(\omega) + \underline{\alpha}^{v}(\omega) + \underline{\alpha}^{r}(\omega)\ . \tag{1.22}$$

Equation 1.22 is a very simplified form, however, it conveys an essential point regarding the common techniques used to measure the dynamic polarisabilities. Rayleigh measurements of $\underline{\alpha}(\omega)$ are usually made at common laser frequencies in the visible region of the spectrum [40, 41]. At visible wavelengths, the vibrational and rotational ($\underline{\alpha}^v(\omega)and\underline{\alpha}^r(\omega)$) contributions to the dynamic polarisability are negligible due to the small transition dipole moments involved. Extrapolation of these measurements of the dynamic polarisability to zero frequency yields therefore a "zero frequency" electronic polarisability ($\underline{\alpha}^e(\omega = 0)$) rather than a static polarisability ($\underline{\alpha}(\omega = 0)$). Although a linear symmetric molecule will have a "zero" rotational contribution, the vibrational component is typically 10% of the static polarisability [42]. Kerr and Stark effect measurements probe the static polarisability and hence include all contributions. However, a comparison with Stark effect measurements can still be made, if the other (vibrational) contributions are accounted for [38].

1.3 Thesis Outline

This thesis will present the results of Stark experiments on the $v = 3$ vibrational overtone of hydrogen fluoride, and the $\nu_1 + 3\nu_3$ and $\nu_2 + 3\nu_3$ vibrational combination bands of acetylene. First a description of the apparatus used to carry out the experiments is provided in Chapter 2. Since the $\nu_2 + 3\nu_3$ vibrational overtone band was too weak to easily measure with a single pass of the laser, an optical resonator with a gain of at least 300 was constructed. The details of the design and performance of this high gain laser power build-up cavity are in Chapter 3. The measurements of the hydrogen fluoride $v = 3$ dipole moment and the vibrational dependence of the hydrogen fluoride dipole moment is discussed in Chapter 4. Chapters 5 and 6 describe the measurements of state mixing among highly excited, vibrational states of acetylene, some of which are not accessible by direct infrared transition from the ground vibrational state. The method of analysis used to extract the polarisability data from the spectra of the $\nu_1 + 3\nu_3$ and $\nu_2 + 3\nu_3$ bands allowed some of the interacting states to be identified as well as the strength of the interaction. Chapter 7 contains a short summary of the findings in this thesis.

Chapter 2

Experimental Details

2.1 The Molecular Beam Apparatus

A schematic of the molecular beam apparatus used in the experiments described in this thesis is depicted in Figure 2.1. It consists of four separate chambers, namely, the source, interaction, detector, and mass spectrometer chambers. The source and detector chambers were each pumped by a Varian VHS–10 (31 cm) oil diffusion pump, capable of a pumping speed of approximately 5500 ℓ/s. The source chamber diffusion pump was backed by an Edwards model EH500 mechanical booster pump (Roots blower) and an Edwards E2M40 mechanical pump. An Edwards E2M8 mechanical pump was sufficient to back the detector chamber, since only a small fraction of the gas escapes the source chamber to form the molecular beam. The detector chamber contained a water-cooled baffle to reduce backstreaming of the hot oil vapour, which could contaminate the detector. This baffle reduced the pumping speed to about 2000 ℓ/s.

Both the interaction and the mass spectrometer chambers could be isolated from the adjacent chambers via gate valves. The gate valve separating the source and interaction chamber was a simple custom-built sliding shutter, that relied on atmospheric pressure in the interaction chamber to provide a proper vacuum seal. It was also used to block the molecular beam when necessary. The interaction chamber was pumped by a liquid nitrogen trapped Edwards mechanical pump. Once the maximum vacuum obtainable with the mechanical pump had been reached, the gate valve to the detector chamber was opened slowly until the pressure equilibrated with that of the detector chamber. The ability to let the interaction chamber up to atmospheric pressure while keeping the other chambers under high vacuum, was a great convenience. It allowed one to make final adjustments to any devices contained within the interaction chamber, such as a Stark cell or the laser power build-up cavity, without significantly interrupting the experiment in progress.

The molecular beam source and the gas handling system were constructed out of stainless steel to prevent corrosion when using hydrogen fluoride. The source nozzle consisted of a 100 μm diameter hole in a thin stainless steel diaphragm which was mounted within a modified SwageLok VCO fitting. The feed tube for the nozzle passed through the end of a capped stainless steel bellows which allowed for a vacuum tight adjustment of the nozzle to skimmer distance by simply sliding the tubing back

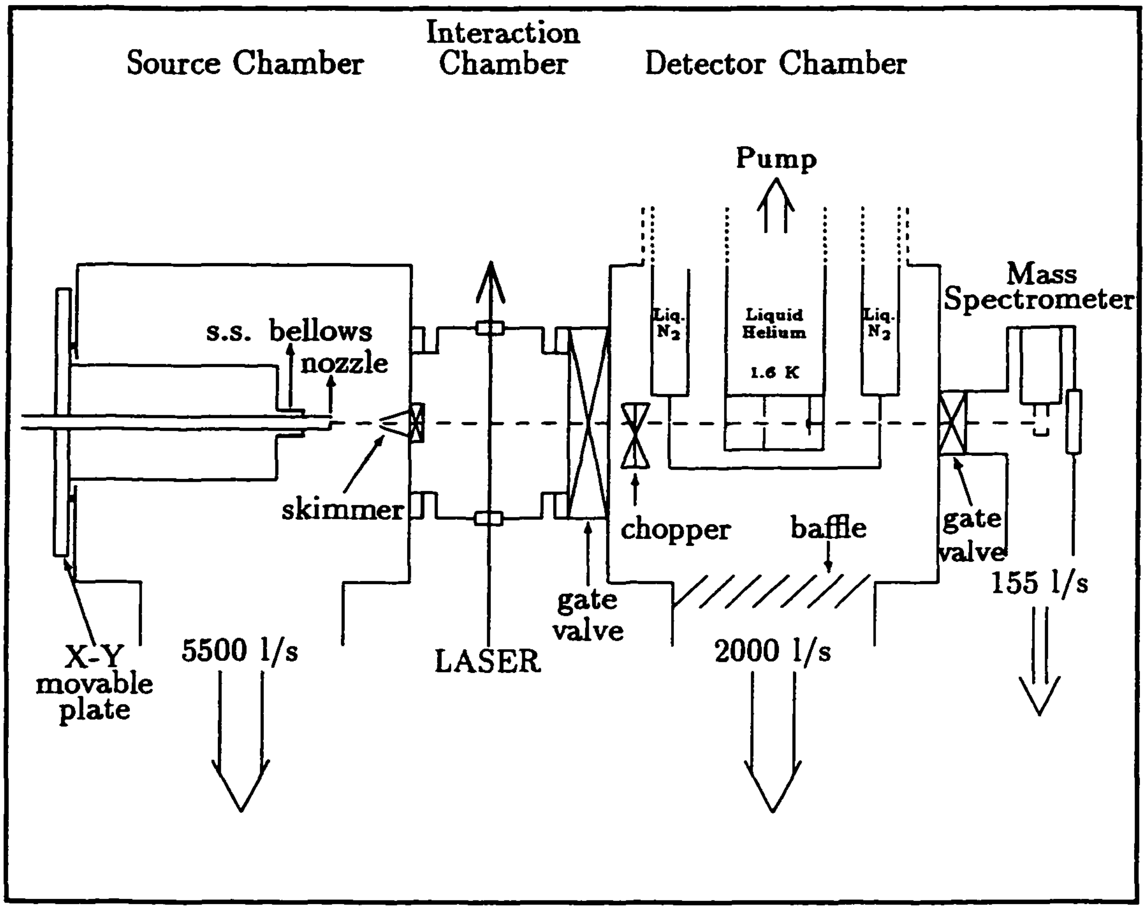

Figure 2.1: This schematic shows a cross-sectional view of the molecular beam apparatus. S.S. is an abbreviation for Stainless Steel. Ionisation pressure gauges were mounted on all chambers except for the interaction chamber. The rubber o-ring which provides the seal between the movable plate and the source chamber flange protruded only slightly from an o-ring groove. The diagram exaggerates this protrusion to make the o-ring more visible. The X–Y movable plate was bolted loosely to the source chamber flange through four oversized holes in the plate. Two pairs of opposing sliding blocks set 90° apart were used to adjust the position of the nozzle plate assembly, while keeping the source chamber under high vacuum.

and forth. The nozzle assembly was mounted on a plate which slid on a well greased o-ring set into the rear flange of the source chamber. Source motion in the X-Y plane was accomplished by sliding the nozzle plate on the o-ring using two pairs of opposing sliding blocks set 90° apart. The nozzle plate was secured to the source chamber flange by four loosely tensioned bolts which passed through oversized holes in the nozzle plate. The 500 μm diameter skimmer was mounted on the flange separating the source and interaction chambers.

The non-corrosive gases to be studied were pre-mixed with helium and the source pressure was maintained with a non-corrosion resistant vacuum regulator. For the experiments on hydrogen fluoride, the source pressure was regulated directly with the supply cylinder regulator and required periodic adjustment. A mechanical chopper located within the detector chamber was used to modulate the molecular beam during the nozzle alignment and optimisation of the source pressure. This allowed the molecular beam intensity to be monitored using phase sensitive detection of the bolometer signal.

A nozzle skimmer distance of approximately 10 mm produced the maximum, chopped, molecular beam signal. The optimum source pressures were found to be between 300 to 500 Torr for the gases studied.

During operation, the source and detector chambers were typically 10^{-6} Torr and 10^{-7} Torr and the ultimate pressures were 10^{-7} and 10^{-8} Torr, respectively. The chamber pressures were measured with MKS ionisation gauges.

The mass spectrometer chamber was pumped by an Edwards 63/150MM oil diffusion pump (135 ℓ/s) and contained a Balzers QMG511 quadrupole mass spectrometer. The lowest background pressure attainable without the molecular beam entering the chamber was 10^{-8} Torr. The mass spectrometer was intended to be used at a future date to assist in the studies of van der Waals molecules. However, the measured signal to noise ratio for single molecules was very low, possibly due to the higher than desired background pressure. The mass spectrometer was not used for any of the experiments described in this thesis.

2.2 The Cryogenic Bolometer Detector

A bolometer is a microcalorimeter capable of detecting minute changes in temperature. It is usually composed of a semiconductor substrate cooled to liquid helium temperatures where its resistance is an exponential function of temperature. Upon impact, the molecular beam raises the temperature of the bolometer primarily through the heat of adsorption. The translational, rotational and vibrational energies of the molecule increase the temperature further, producing a larger change in resistance. Excitation of, for example, a ro-vibrational energy transition of the species under investigation with a laser increases the internal energy of the molecules in the beam, which in turn is detected by the bolometer.

The bolometer (Infrared Laboratories Inc.) used in the experiments described in this thesis consisted of a small silicon element (0.01 cm^2) thermally bonded onto the centre of a 2.0 mm × 5.0 mm diamond slab and suspended by thin wire leads from a detector mount secured to the bottom of the cryostat. The bolometer was located approximately 84 cm downstream from the skimmer. This entire bolometer assembly was contained within a copper box mounted to the bottom of the liquid helium cryostat so as to shield against extraneous thermal radiation (Figure 2.2). The copper box had four ports at various locations which served either to allow passage of the molecular beam or to allow non-condensable carrier gas to be pumped away. One port was baffled and located adjacent to the bolometer. A pair of opposing ports located in the centre of the copper box allowed the molecular beam to travel through the box, missing the bolometer when the cryostat was rotated 90° with respect to the molecular beam axis. One port, located directly opposite the detector mount, allowed the molecular beam to reach the bolometer.

A liquid nitrogen cooled shield was used to insulate the liquid helium cryostat and bolometer from the surroundings. A 1 mm horizontal slit mounted on the outside of the liquid nitrogen cryostat shielded the bolometer from molecules travelling with a significant component of their velocity parallel to the laser beam travelling vertically through the interaction chamber. This further reduced the Doppler shift induced broadening of the transition line shapes.

The bolometer was cooled to the operating temperature of about 1.6 K by pumping on the liquid helium bath with a mechanical pump until a bolometer resistance of approximately 35 MΩ was reached. In addition to the pre-amplifier, a JFET-amplifier was required to operate this bolometer. To reduce microphonic noise and excess input capacitances, it was mounted close to the bolometer on a stand-off and held at 77 K. Under these conditions the measured responsivity was typically 5×10^6 V/W, with a noise equivalent power (N.E.P.) of approximately 4×10^{-13} W/Hz$^{1/2}$ [43]. Although the liquid helium cryostat had a capacity of approximately two litres, once the operating temperature was reached, much less than this remained. Typically a good liquid helium transfer resulted in about 10-12 hours of operating time.

With the detector rotated 90°, a diode laser could be shone through the window in the mass spectrometer chamber, through the hole in the copper bolometer box and directly at a photodiode mounted behind the skimmer in the source chamber. Once the alignment laser was positioned correctly, two apertures with removable irises were placed in the interaction chamber along the molecular beam axis using the diode laser as a guide. This provided a precise alignment of other instrumentation with the axis of the molecular beam while the entire system was at atmospheric pressure. The infrared laser, used in the experiments, entered the interaction chamber from below and exited at the top. The precise intersection point of the molecular beam and the infrared laser could be determined by observing the crossing position of the alignment diode laser and the infrared laser. A window installed in the gate valve separating the interaction and detector chambers allowed this same alignment procedure to be performed on devices within the interaction chamber, while the detector and source chambers were under high vacuum. Instruments could be added to or removed from

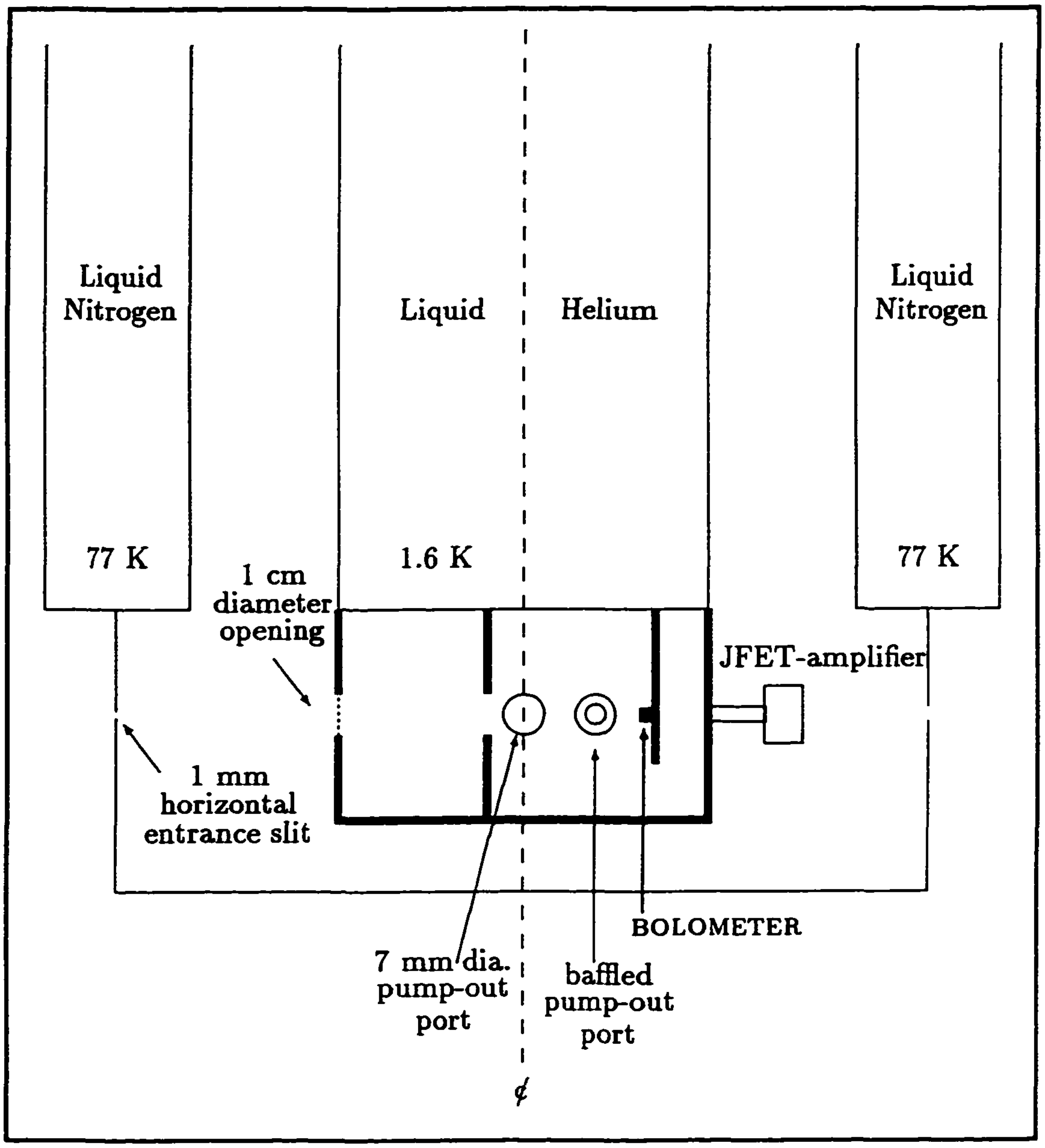

Figure 2.2: This diagram depicts a vertical cross-section of the bolometer detector assembly along the molecular beam axis. The thick outlines represent the copper box. The liquid helium cryostat was surrounded by a liquid nitrogen shroud to reduce the thermal load on the inner cryostat. The ¢ denotes the rotation axis of the entire detector cryostat.

the interaction chamber without compromising their alignment with the molecular beam. This was a common task while using the laser power build-up cavity.

2.3 The Stark Cell

The Stark cell used in these experiments consisted of two 5 cm diameter aluminum plates held apart by a fixed ceramic spacer (See Figure 2.3). This arrangement did not allow for a simple adjustment of the Stark electrode gap. Either the spacer or the electrodes had to be modified or replaced. The electrodes were polished and all sharp edges were rounded to reduce arcing. A Bertan model 205A-30P, 0–30 kV high voltage supply was used to generate the electric field. For molecules with an appreciable dipole moment (e.g. hydrogen fluoride) a 5 mm gap was sufficient and produced electric fields on the order of 40 kV/cm. However, for acetylene a much smaller gap of approximately 0.6–0.7 mm was needed and new electrodes were made. With flat, highly polished electrodes, fields as high as 350 kV/cm were generated.

2.4 The Laser System and Experiment Controls

The laser system was a Coherent 899 Ti:Sapphire (titanium doped sapphire) laser pumped by a Coherent Innova 200 Argon Ion laser. Figure 2.4 depicts the arrangement of the entire experiment. The Ti:Sapphire laser provided tunable near infrared radiation (11300—13300 cm^{-1}), with a peak power of approximately two Watts single

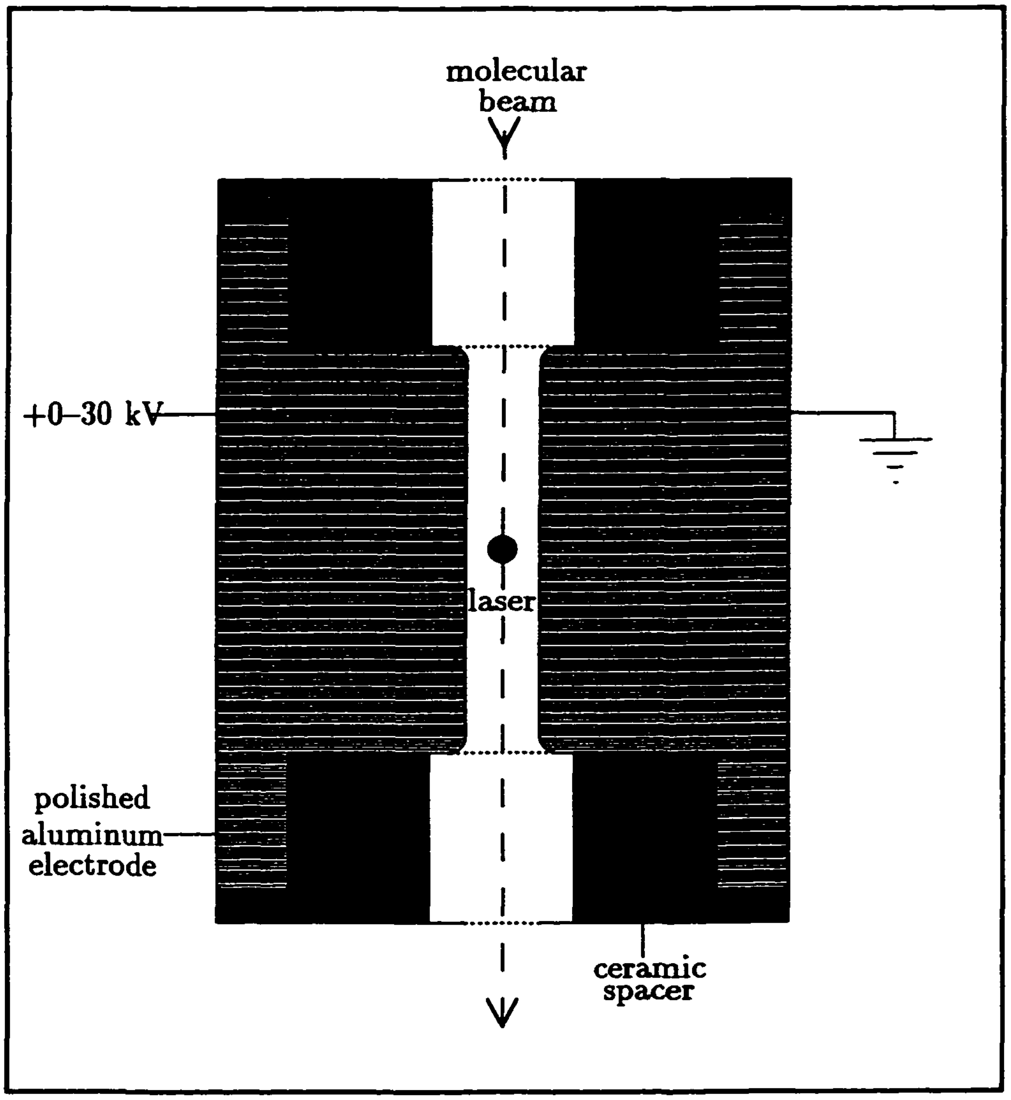

Figure 2.3: A cross-section of the Stark cell used in the experiments as viewed from above. The ceramic spacer held the aluminum electrodes at a fixed distance. To change the spacing of the electrodes, new electrodes had to be machined.

frequency and a minimum frequency line width of approximately 5 MHz. The line width was determined by measuring a ro-vibrational molecular beam transition (see for example, Chapter 4, Figure 4.1, page 62). Although the Ti:Sapphire laser was designed to be frequency stabilised, an external reference etalon was used to verify the linearity of the laser scan. The free spectral range of the etalon was 274.21±0.05 MHz, determined by measuring the spacing (54.65±0.01 cm) of the etalon mirrors with a set of vernier calipers. Despite the use of an external reference etalon, slow drifts of the frequency of the laser were still the principal source of error in these experiments. To minimise these errors the laser was scanned repetitively up and down over the spectral region under investigation. Systematic frequency drifts could therefore be detected and averaged out.

In order to locate the molecular beam transitions, the laser was passed through a photoacoustic cell before entering the molecular beam machine. The laser frequency was measured with a Burleigh WaveMeter accurate to ±0.01 cm^{-1}. An optical chopper was used to modulate the laser intensity to allow for the use of phase sensitive detection of the laser induced bolometer signal. The photoacoustic gas cell equipped with a Knowles Electronics BL 1785 microphone, the wavemeter and literature values for the transition frequencies of the molecules of interest were used to position the laser on the peak of the bulk gas absorption frequency. The photoacoustic cell was then removed and the laser scanned repetitively over the central part of the absorption profile until the lock-in amplifier registered a laser induced signal from the bolometer.

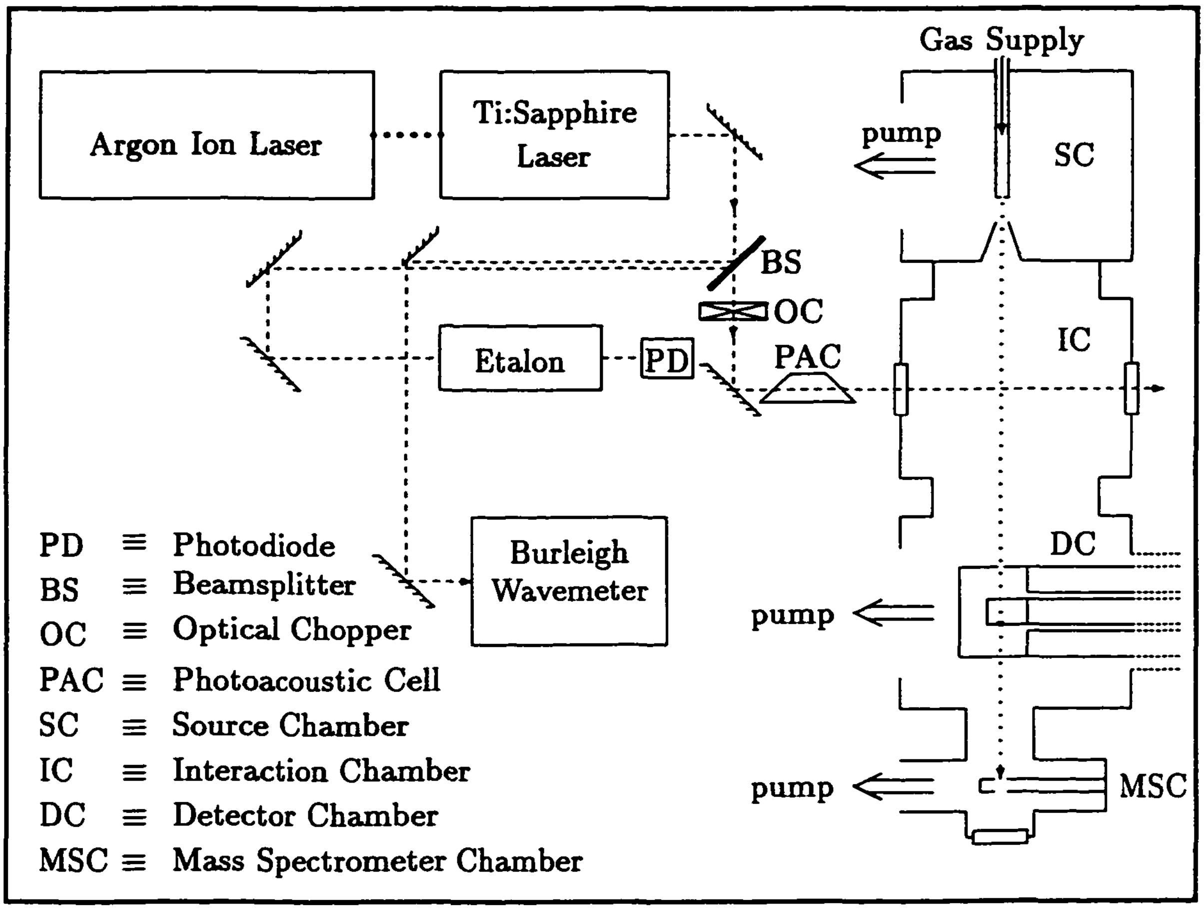

Figure 2.4: This is a cross-sectional view of the molecular beam apparatus along with the rest of the instrumentation on the adjacent optical tables. The interaction chamber can be isolated from the rest of the vacuum system with two gate valves (not depicted here), allowing the insertion or extraction of Stark electrodes or the laser power build-up cavity. For simplicity the components used primarily for the build-up cavity experiments have been left out. They are illustrated in Figure 3.3.

A mirror could be mounted on the exit (top) side of the interaction chamber, allowing the laser to be retro-reflected. This helped establish a perpendicular laser–molecular beam crossing.

The microphone was not corrosion resistant and could therefore not be used when working with hydrogen fluoride. However, hydrogen fluoride's large transition dipole moment allowed molecular beam absorptions to be detected easily using fast scans over larger frequency regions. Generally, the lock-in amplifier's sensitivity was set to a sensitive scale, such as 1 mV full scale or less, and the laser was scanned manually in the vicinity of the reported literature value. Even when the line position was only briefly encountered during these manual scans, the overload warning lit up on the lock-in amplifier, identifying the presence of an absorption line.

An 80386 IBM PC compatible computer controlled the laser scan, turned on or off the Stark field and collected the data using custom software written specifically for the instrumentation at hand.

Chapter 3

The Laser Power Build-up Cavity

3.1 Preamble

Normally the description of this device would have been included in the chapter on "Experimental Details", as the intention was to use it as any other piece of laboratory equipment. However, the design, construction, re-design, re-construction and so on, along with constant testing of the build-up cavity turned out to be more than a project in itself. Hence, a separate chapter has been devoted to describe the design, function and performance of the laser power build-up cavity.

3.2 Introduction

The measurement of vibrational overtone bands in the near infrared and visible regions of the spectrum often requires the use of some sort of laser power enhancement device due to the weak nature of the transitions. The never ending search for techniques and devices to make these measurements possible has led to a variety of solutions. Multipass cells, such as White cells were, and still are, often used. However, the resulting Doppler broadened line shapes obscure some of the most interesting aspects of these highly congested spectra [44–48]. High resolution (sub-Doppler) spectra may be measured in a molecular beam laser spectrometer, but the typical 1–2 Watts of power available from most continuous wave lasers is not sufficient to detect all the transitions of interest. To increase sensitivity of the measurement, the trend has been to either pass the molecular beam directly through the cavity of the laser [49] or to develop a separate optical resonator that can be placed inside the vacuum chamber of the molecular beam apparatus [50]. The former method is inherently difficult and limited to the gain available inside the laser cavity. The latter technique is by no means easy; however, the potential for a much larger gain exists.

The use of such optical resonators or laser power build-up cavities (BUC) is not new. In 1980 Brillet and Gallagher were among the first when they placed a rubidium cell inside a BUC [51]. Wieman and Gilbert extended this by crossing the standing wave laser field of their BUC with a beam of cesium atoms [50]. Both of these methods produced modest gains of approximately twenty. Neusser and Riedle designed a

BUC that provided a gain of fifty [52] and Reilly *et al.* constructed one with a potential gain of one hundred [48]. Ultimately only a gain of fifty could be used due to a necessary modification required for the measurement of the Stark effect on ro-vibrational transitions. Full details of this BUC may be found in the dissertation by Douketis [53]. Wieman *et al.* designed a self-locking BUC for laser diodes that relied on a little optical feedback to lock the laser frequency to the cavity resonance. The aim was to eliminate the need for the "feedback" electronics required to keep the cavity on resonance [54]. Some electronics were still necessary to avoid having small (MHz) gaps in the tuning range and a gain of 1000 was achieved. This was a substantial advance in laser power enhancement. However, it was designed using low-power laser diodes and, as will be shown later, this is much different from higher power laser systems.

3.3 Design and Construction

During this project many different BUC designs were tested with varying degrees of success. A "sandwiched" arrangement was finally chosen due to its mechanical stability and simplicity (See Figure 3.1). The principal assumption behind this arrangement was that the mirrors are clamped parallel to one another and the only alignment required is that of the axis of the BUC with the propagation direction of the laser through the vacuum chamber. The mirrors were ion beam coated for 99.95% reflectivity at 850 nm (see Figure 3.2) with an absorption of less than 20 ppm

(Research Electro-Optics). The mirrors (2.54 cm diameter, 50 cm radius of curvature), were sandwiched together in an aluminum housing held apart only by a 2.54 cm diameter ceramic cylinder, 1.826 cm long, and a 0.42 mm thick teflon shim. Three piezoelectric (PZT, lead-zirconate-titanate) elements mounted 120° apart on an aluminum ring bore down on the upper mirror and adjusted the mirror spacing by deforming the soft teflon shim. The PZTs had a displacement of 5 nm/V up to a maximum displacement of $5\mu m$. Since the aluminum ring was in electrical contact with the PZTs, it was insulated from the aluminum body with a Delrin (nylon) sleeve on the sides and boron nitride tube on top. An aluminum end cap threaded onto the BUC body clamped the entire assembly rigidly together.

The ceramic spacer also had another function. It was designed to hold the Stark electrodes at a fixed distance of approximately 0.85 mm (calibrated later, see page 97 in Chapter 6). The Stark electrodes were machined from 0.625 inch tool steel. The face diameter was reduced to 0.5 inches, leaving a shoulder which rested on a lip machined into the ceramic spacer. The electrode surfaces were ground and polished and all edges were rounded over. One Stark electrode was held in place by a 6-32 cap screw at ground potential. The other was secured by a high voltage brass electrode (0-30 kV).

The BUC housing was designed to fit within a 2.54 cm (1 inch) mirror mount which, in turn, was mounted on an XY translation stage. The mirror mount allowed the entire BUC to be tilted in the XZ and YZ planes and the translation stage

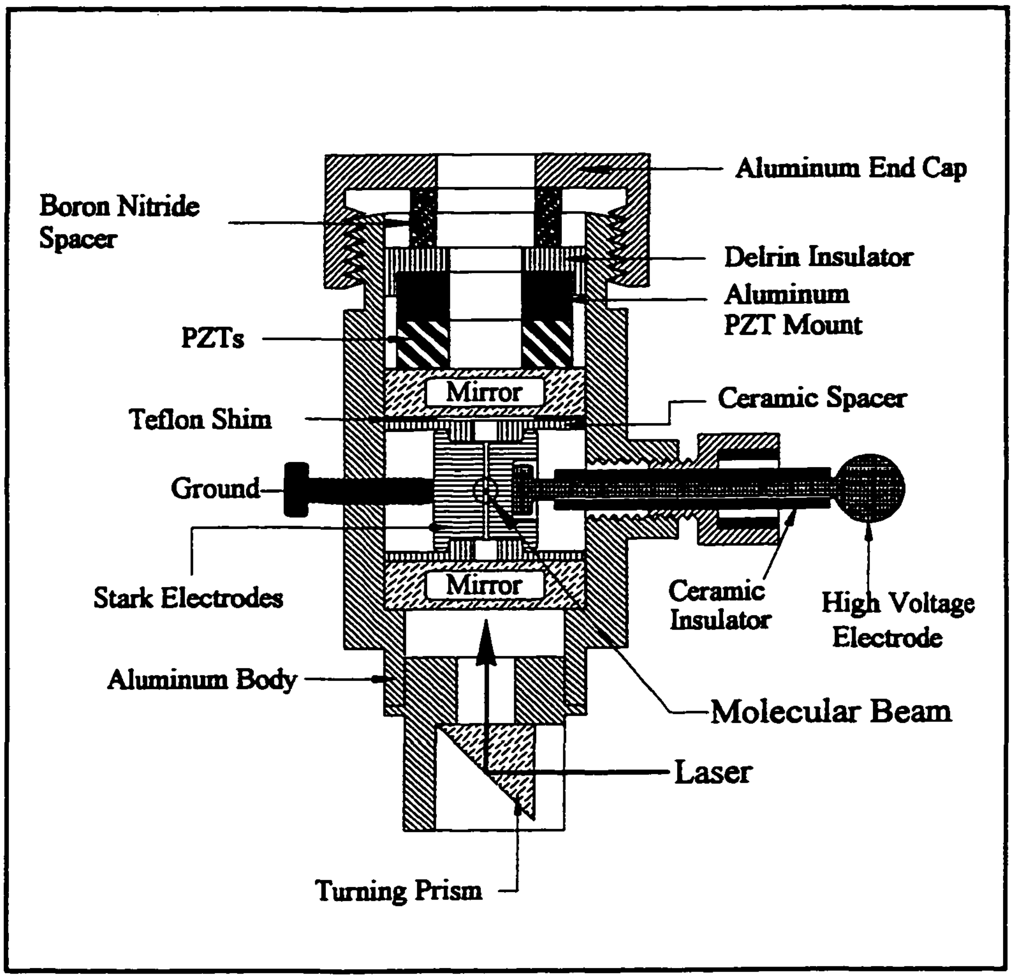

Figure 3.1: This is a cross-section of the laser power build-up cavity drawn to scale. Only two of the PZTs are depicted. There are three in total, situated in a circle 120° from one another.

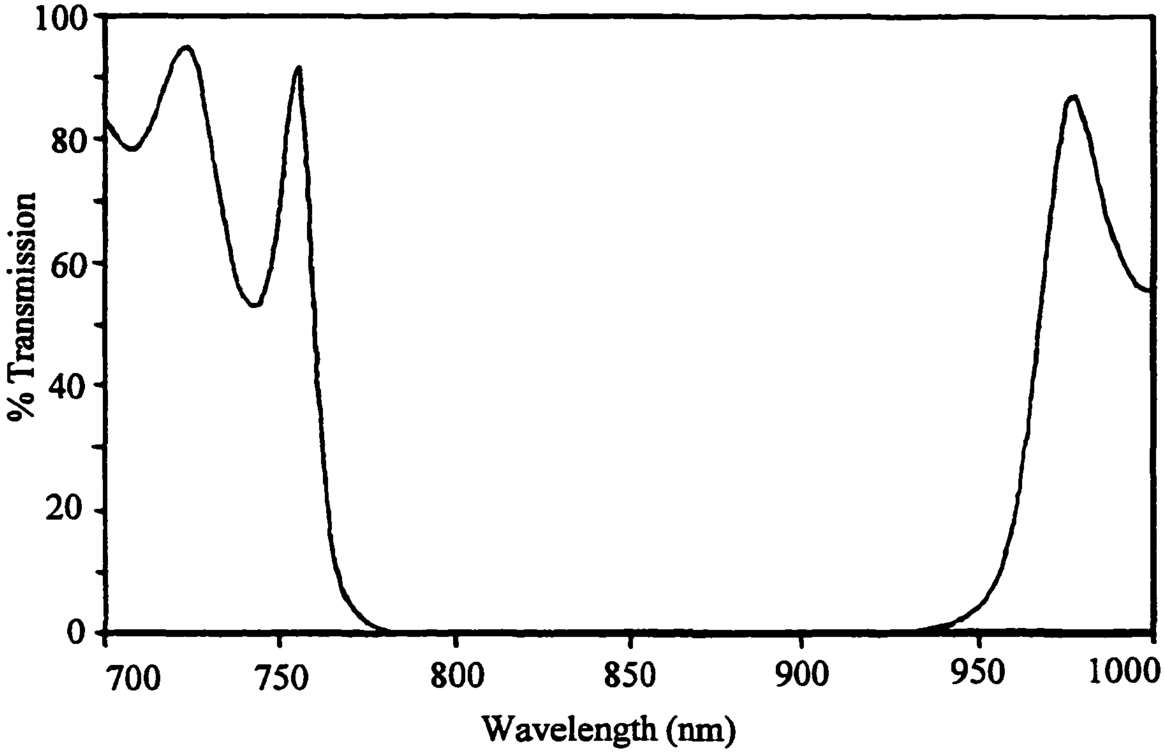

Figure 3.2: Transmission curve of the mirrors used in the laser power build-up cavity supplied by Research Electro-Optics. The mirrors were coated for a reflectivity of 99.95% with an absorption of less than 20 ppm.

provided separate movement in the X and Y directions (See Figure 3.3). The 90° turning prism (P_1) fastened to the bottom of the BUC together with the second prism (P_2), mounted on the base plate of the interaction chamber enabled the BUC to be translated across the molecular beam (X direction) without significant loss of alignment. This allowed the laser induced signal to be maximised by adjusting the overlap of the cavity waist inside the resonator with the molecular beam.

An optical isolator was used to prevent optical feedback from the BUC into the Coherent 899-21 Ti:Sapphire laser. The optical isolator rotated the vertically polarised laser field 45°. The plane of polarisation was rotated another 45° by the half-waveplate, to provide a laser electric field polarisation perpendicular to the Stark electric field (allowing $\Delta M = \pm 1$ transitions only, see page 13).

A 40 cm focal length lens was placed approximately 40 cm from the centre of the BUC to increase the throughput intensity by helping to match the BUC modes to those of the incident laser. A photodiode was used to monitor the transmitted light and provide a signal for the electronic lock-circuit used to keep the BUC on resonance. It was necessary to use a diffuse reflector for monitoring the transmitted intensity rather than observing it directly. If monitored directly, the exact position of the photodiode was critical, since it was possible to place the photodetector in a position that preferentially observed the higher order transverse modes instead of the lowest order mode (TEM_{00}). In such a case, the intensity distribution among the transmitted modes was no longer a reliable indicator of the BUC alignment. A diffuse

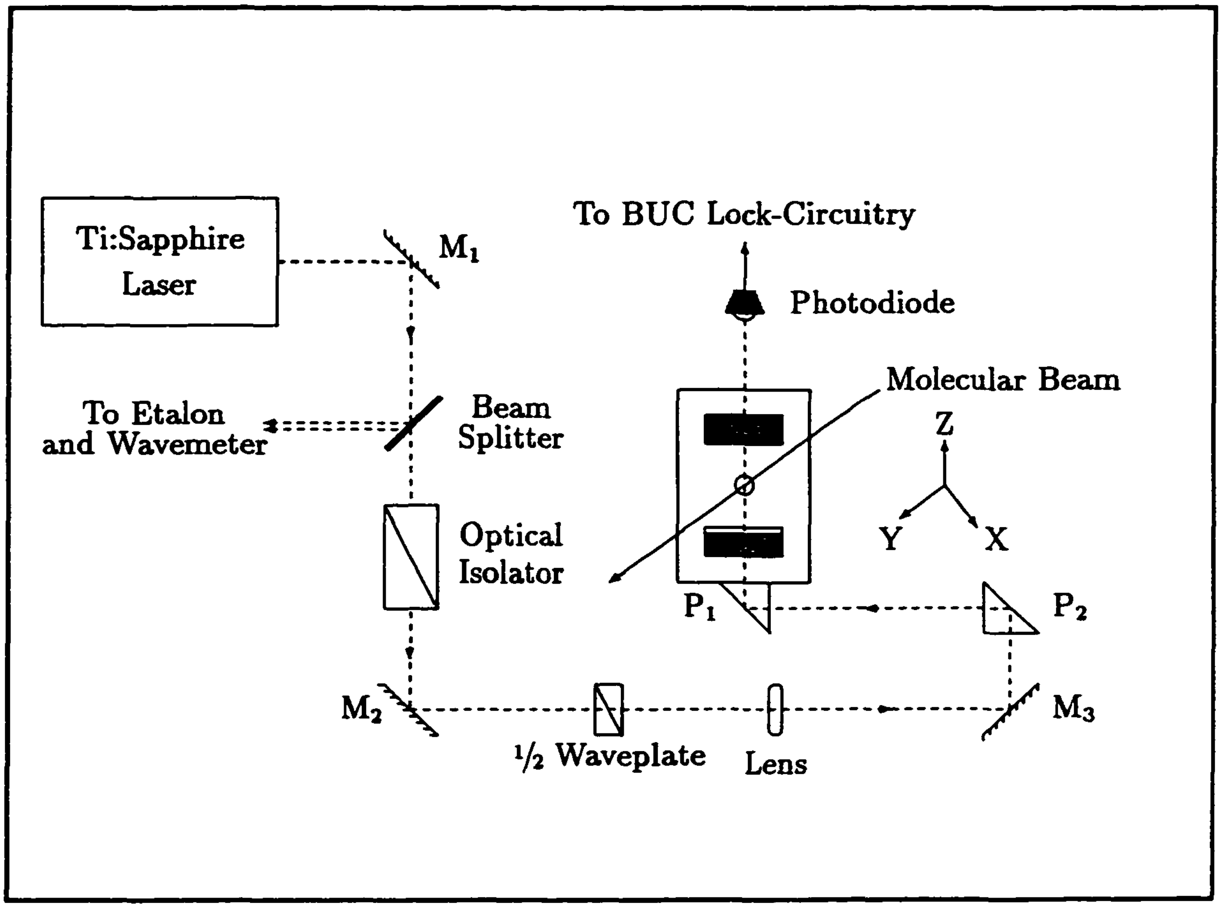

Figure 3.3: Optical layout for the laser power build-up cavity experiments. For simplicity, the molecular beam apparatus and other unrelated components have been omitted. The direction of the molecular beam is indicated with an arrow and is orthogonal to the BUC z-axis. (M_1, M_2 and M_3 are mirrors, while P_1 and P_2 are prisms.)

reflector eliminated the position sensitivity by scattering the transmitted laser light from all modes equally.

Rather than using a mechanical chopper to modulate the intensity of the laser light for the lock-in amplifier, the laser was frequency modulated. This was accomplished by applying a small amplitude oscillation (107 Hz) to the scan control electronics of the laser. Initially the amplitude of the laser light was modulated, but the BUC resonance locking electronics would frequently lose lock of the laser frequency during a chopper "off" cycle. The reason for this will be made clear later.

3.4 Electronic Feedback Controls

The circuitry designed to keep the BUC on resonance while the laser was scanning was relatively simple. Conventionally the electronics used to keep the BUC on resonance are designed to maximise the transmitted light through the BUC (locking to a transmission peak). For the present system a "lock-point" on the low frequency side of a resonance peak was selected and its position could be varied as desired. Obviously this does not allow one to attain the maximum gain available, but as will be shown later it was the only option for this particular BUC. Typically the lock-point chosen was at about 75% of the transmission peak height as measured by an external photodiode.

To avoid introducing noise from external AC power sources, the BUC PZTs were biased by using battery supplies. An adjustable 600 V battery pack biased one side of the PZT stack and was used to bring a BUC longitudinal mode into resonance at the chosen laser frequency by changing the length of the PZTs. The error signal generated by a comparator circuit referenced to the lock point on the transmission fringe was amplified and applied to the other side of the PZT stack. This fast tracking was limited to a maximum of 90 V. The 5 μm/1000 V response of the PZTs made it possible to use such a small voltage for tracking the resonance. If the 90 V supply approached its limit during a laser frequency scan, a manual adjustment with the 600 V supply was made to bring the tracking voltage back within the range of the 90 V supply. Typically this was only required for the longer frequency scans ($\geq$1 GHz). Two separate bias supplies were necessary, because the low noise electronic components used to keep the BUC on resonance were not designed to withstand high voltage.

3.5 Results and Discussion

3.5.1 Build-up Cavity Diagnostics

The alignment of the BUC was monitored by observing the intensity distribution among the transverse modes. This was accomplished by keeping the BUC mirror spacing fixed and scanning the laser rapidly (60 GHz/s). Translation and tilt controls were adjusted in turn until the TEM_{00} mode was predominant. Figure 3.4 depicts a typical transmission spectrum of the aligned BUC. The "zero" frequency refers to

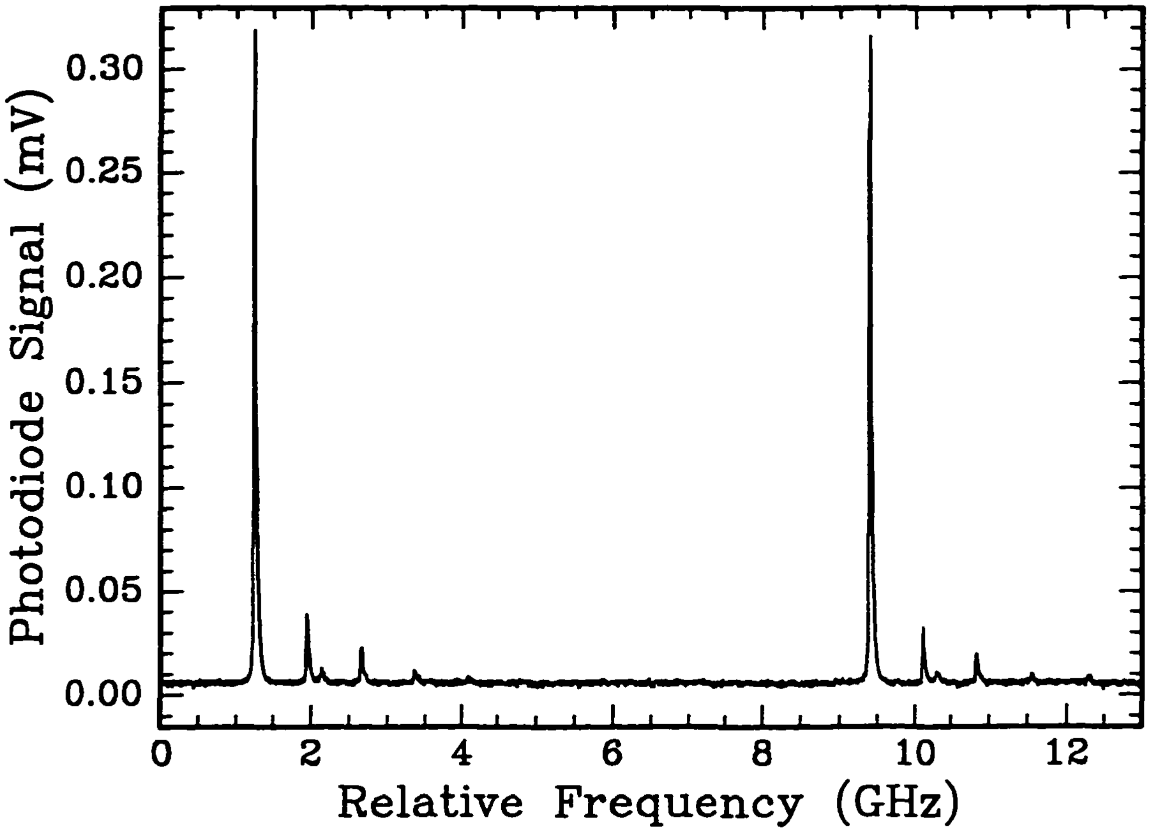

Figure 3.4: This diagram depicts the transmission spectrum of the BUC when illuminated by the Ti:Sapphire laser. The spacing between the two most intense peaks corresponds to the FSR (8.15 GHz) and the smaller peaks are higher order transverse modes. The "zero" frequency refers to the start of the laser scan. The laser was scanned at a rate of 60 GHz/s.

the start of the laser scan. The high intensity peaks are two successive longitudinal modes (TEM_{00}), while the smaller peaks are higher order transverse modes. It was impossible to completely eliminate these higher order modes with the present system.

The free spectral range (FSR) of the BUC (FSR = c/2L, where c is the speed of light and L is the mirror spacing [55]) was calculated to be 8.02 GHz, which compares well with the measured value of 8.15 GHz. The discrepancy is likely due to the non-uniform nature of the teflon shim used as part of the spacer for the mirrors. It was difficult to accurately measure the thickness of the teflon shim since it was very soft. High spots on the teflon shim increase the mirror spacing, which in turn decreases the FSR of the BUC. From Figure 3.4 the finesse $\mathcal{F}$ of the BUC can also be measured. It is simply the ratio of the FSR to the full-width at half maximum height (FWHM) of a transmission peak ($\mathcal{F}$ = FSR/FWHM [55]), which in this case is 250. This number is typically used to describe the resolving power of a Fabry-Perot cavity (interferometer). It can also be used to judge the potential gain of a BUC, since it increases with mirror reflectivity, as does the circulating power inside the BUC, and is relatively simple to measure experimentally. One important aspect of the finesse is that a very high finesse resonator will typically have a very sharp line width (FWHM). The theoretical expression for the finesse ($\mathcal{F} = \pi\sqrt{R}/(1\text{-}R)$) indicates that the present BUC has a potential finesse of 6282 and, therefore, a FWHM of 1.3 MHz. Considering that Coherent Laser Group claims a line width of 0.5 MHz for their laser, it will become increasingly difficult to lock the resonant frequencies of a high finesse

BUC to such high resolution lasers.

Close examination of the transmission peaks revealed that they are somewhat asymmetric. To ensure this was not simply due to the slow response of the photodetector, a second slower scan (100 MHz/s) of the transmission spectrum was taken (Figure 3.5). This spectrum was a result of scanning the laser past a longitudinal resonance and then reversing the scan direction to measure the same resonance again. In this case the "zero" frequency case marks the turning point of the laser. The resonance peak is much broader when the laser scans to higher frequency than when the laser scans in the reverse direction (33.5 MHz versus 12.2 MHz). One possible explanation is that the mirror coatings absorb some of the light circulating in the cavity, even though mirrors were designed to have an absorption of no more than 20 ppm. If the circulating power in the cavity is great, this could still amount to a significant quantity of heat being deposited on a very small area of the mirror surface. The mirror coatings would expand, resulting in a slight decrease of the mirror spacing and a shift of the resonance to a slightly higher frequency. Thus, the combination of the cavity resonance drifting to a higher frequency and the laser scanning to a higher frequency results in a prolonged period of resonance and a broad peak. There will come a point when the mirror coatings can no longer expand, when some sort of "steady-state" has been reached. Then, when the laser scans over the top of the resonance peak the mirror surfaces will begin to cool and suddenly shrink back, resulting in a sharp decrease in transmitted light. During the reverse scan the cavity

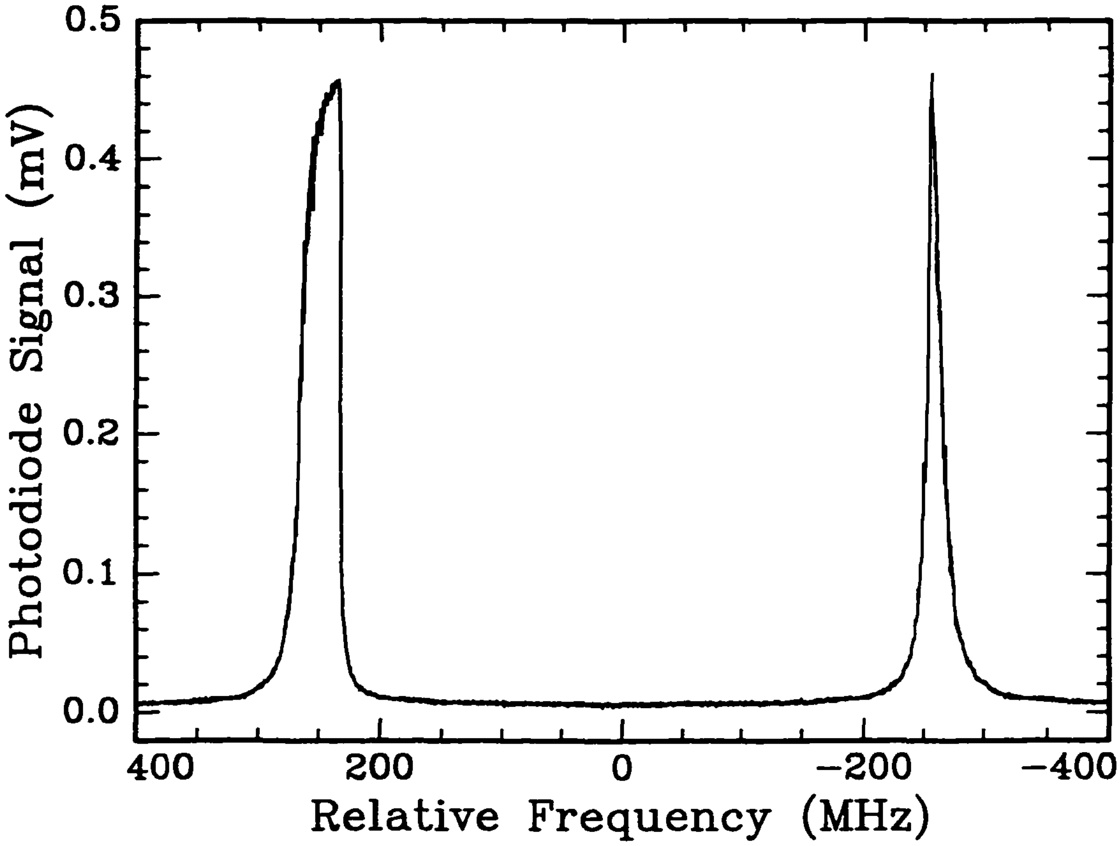

Figure 3.5: In this illustration the laser is scanned to increasing frequency just past a BUC longitudinal resonance and then the scan is reversed. The turn-about position was at "zero" frequency. The scan speed used was 100 MHz/s, 600 times slower than that used in Figure 3.4.

resonance frequency opposes the direction of the laser scan and the peak is much sharper. This "heating" phenomenon can be exaggerated if the laser is scanned very slowly, to produce resonances with an apparent width of 500 MHz! It is for this reason that the lock-point for the electronics was chosen to be on the low frequency side of the transmission peak. When a mechanical chopper was used to modulate the amplitude of the laser beam, the BUC went through a series of heating and cooling cycles, expanding and contracting, that made it very difficult for the tracking electronics to keep a BUC resonance locked to the laser frequency. The distortion of the mirror coatings will limit the gain of the cavity and also the circulating power.

The intense heat build-up on the mirror is a result of the laser illuminating only a small area of the mirror surface. The intracavity laser beam spot size at the mirrors is given by the following equation [55] :

$$w_1^2 = \frac{L\lambda}{\pi}\sqrt{\frac{1}{1-g^2}}, \tag{3.1}$$

where g is the stability parameter (g = 1-R/L), L is the mirror spacing and R is the reflectivity of the mirrors. The laser spot size on the mirror is calculated to be 272 μm in diameter. If only 10% of the incident laser power (approximately 1.7 Watts) were coupled into the BUC and the gain were unity, the mirrors would endure approximately 290 Watts/cm^2. This is not an exceptionally large quantity, since mirrors typically have a 1000 Watts/cm^2 damage threshold. However, a gain of only four would exceed this limit and the following sections will show that the actual gain is much higher.

3.5.2 Build-up Cavity Performance

The most notable characteristic of any BUC is its gain. If the cavity were loss-less, the gain could simply be calculated from the mirror reflectivities. An ideal symmetric resonator has a maximum magnification of 1/(1-R), where R is the reflectivity of the mirrors [55]. The mirrors chosen for this BUC have a reflectivity of 99.95% and, ideally, a maximum gain of 2000. The losses of the cavity, either due to absorption or a mismatch of the incident laser and BUC modes, can be determined by measuring the ratio of transmitted (I_{trans}) to the incident (I_{inc}) laser power. The following equation relates these quantities [55]

$$\frac{I_{\text{trans}}}{I_{\text{inc}}} = \frac{(1-R)^2 e^{-\alpha_0 p}}{(1-Re^{-\alpha_0 p})^2}. \tag{3.2}$$

In Equation 3.2 the losses (e.g. absorption losses) are represented by α_0 (cm^{-1}) and p is the cavity round-trip length ($p = 2L$, in cm). By carefully adjusting the PZTs it was possible to hold the cavity near the peak of its resonance long enough to measure the transmitted power with a calibrated power meter. The ratio of transmitted to incident laser power was measured to be 0.514, resulting in a value of $5.4 \times 10^{-5}\text{cm}^{-1}$

for α_0. This value can be substituted into ([55])

$$\frac{I_{\text{circ}}}{I_{\text{inc}}} = \frac{1-R}{(1-Re^{-\alpha_0 p})^2} \tag{3.3}$$

where I_{circ} is the power circulating in the BUC. The gain is then established at 1030. This implies that there were 900 Watts (1030 × 0.514 × 1.7 Watts) of laser light concentrated on a very small portion of the mirror surface (5.81×10^{-4} cm^2). The mirror coating was subjected to 1.54 MW/cm^2. For obvious reasons it was not possible to keep the cavity locked to the peak of its resonance. The lock-point method used in the present experiment reduced the gain and the heating of the mirrors, but not substantially. Even at 75% of the maximum, the mirror coatings are required to withstand more than 1 MW/cm^2. Using this BUC in an application requiring laser diodes that typically have 100 times less power may reduce this problem. However, using a less powerful laser does nothing to help the measurement of weakly absorbing molecular transitions.

3.5.3 Build-up Cavity Gain

Depicted in Figure 3.6 are two spectra of the $J = 4 \leftarrow 3$ ro-vibrational transition (11609.01 cm^{-1}) of the $\nu_2 + 3\nu_3$ band of acetylene. For simplicity the spectra were centred about the absorption frequency of the transition. Spectrum **A** was measured using the BUC and spectrum **B** was a result of a single crossing of the laser and molecular beam.

The first-derivative type line shape in spectrum A was a result of the frequency modulation (FM) technique used for detecting the laser-induced signal [56, 57]. The laser frequency was modulated by adding a 107 Hz oscillation to the voltage ramp that controlled the laser scan. Adjusting the amplitude of the oscillation therefore also adjusted the frequency modulation amplitude. The maximum laser induced signal was observed for a frequency modulation amplitude of approximately 5 MHz. Theory predicts the maximum signal to be generated by FM amplitudes equal to the FWHM of the spectral transitions [56]. This indeed compared well to the FWHM of the absorption lines measured by laser intensity modulation (5.4 MHz, Section 2.4).

Although it had the appearance of a first derivative (Figure 3.7A), as can be seen in Figure 3.7B a simple integration did not necessarily produce the true line shape. This discrepancy was largely attributed to the fact that frequency modulating the laser also modulated the intensity of the BUC. The resulting "true" line shape (Figure 3.7B) was not easily integrated for comparison of transition intensities. When intensity comparisons were required, the frequency modulation amplitude was reduced and sometimes even the average of several line shape measurements was taken to obtain a near symmetric line shape. The peak-to-peak intensities of lines of identical line width could also be compared, but the transitions of interest rarely had identical line widths.

The amount of frequency modulation also affected the line shape, but in this

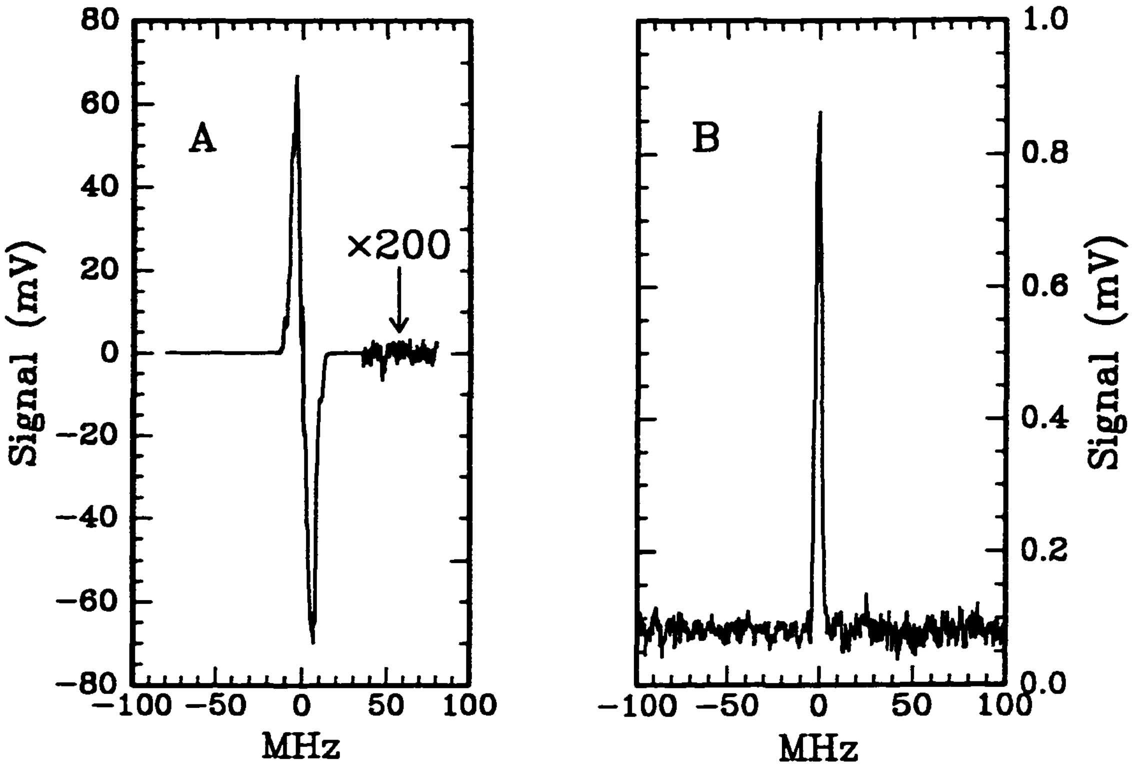

Figure 3.6: The high resolution spectrum of acetylene's $\nu_2+3\nu_3$ R(3) transition at 11609.014 cm^{-1} is depicted here. Spectrum **A** was recorded using the BUC, while spectrum **B** was the result of a single crossing of the laser and the molecular beam. The baseline noise in **A** was magnified by a factor of 200 while recording the spectrum to provide a more accurate measure of the signal-to-noise ratio (S/N). The S/N ratio of **A** was approximately 4500:1 and **B** was 15:1. The result was a gain of at least 300.

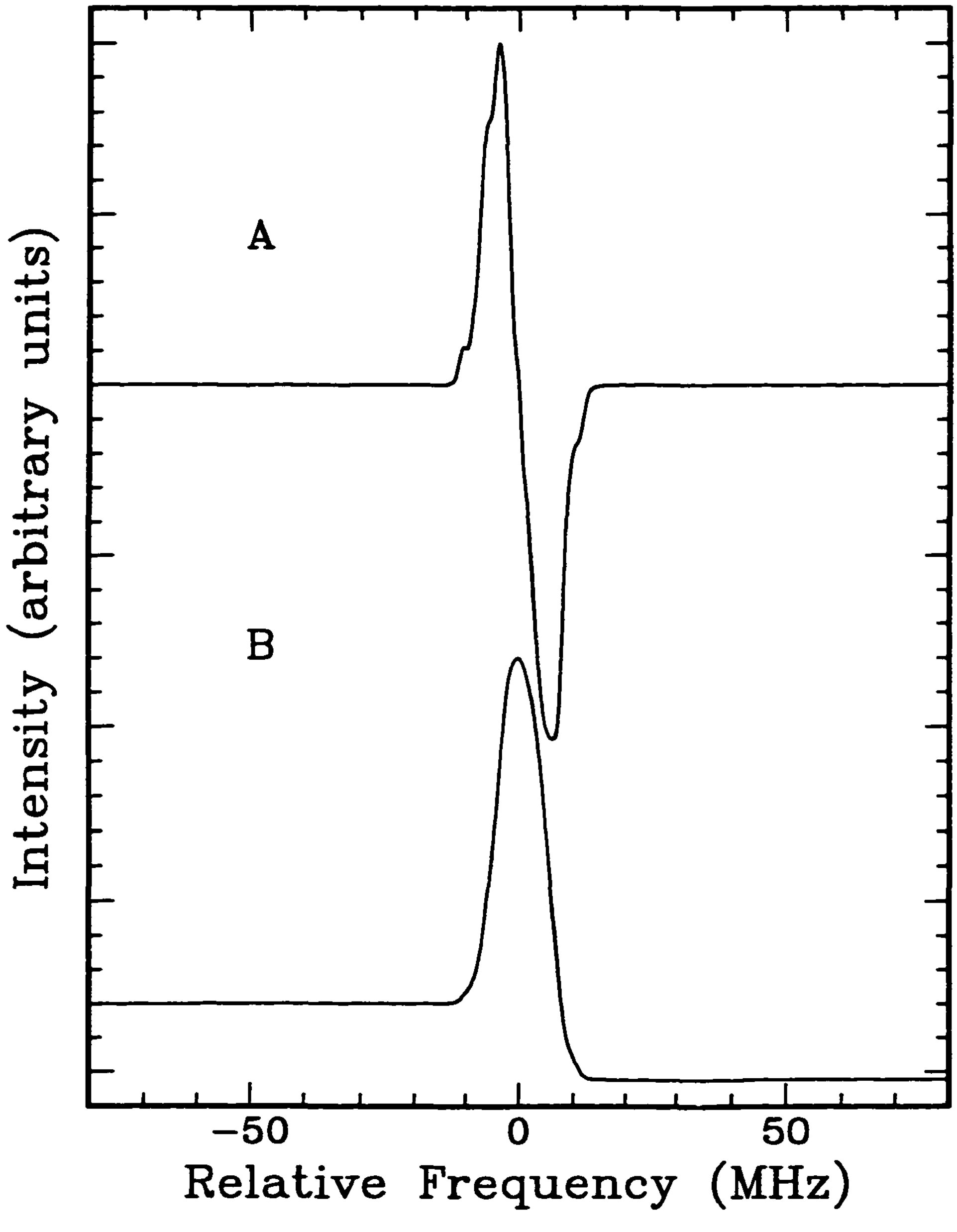

Figure 3.7: Line shape of the R(3) $\nu_2+3\nu_3$ ro-vibrational transitions measured with the BUC while frequency modulating the Ti:Sapphire laser. **A** is the measured first derivative type signal, while **B** is the result of integrating **A**.

case, it was not possible to achieve a perfectly symmetric line shape by adjusting the frequency modulation amplitude. Figure 3.8 depicts the line shape as a function of frequency modulation amplitude for the R(4) $\nu_2 + 3\nu_3$ ro-vibrational transition of acetylene. The integrated signal increased linearly with an increase in frequency modulation amplitude, but the line shape also became much more asymmetric. Even at low amplitudes of frequency modulation (0.33 MHz), the line shape was not perfectly symmetric and the signal-to-noise ratio was only about 2:1.

The broadening and asymmetry of the line shapes was not necessarily a problem for well resolved spectra. However, the maximum FM amplitude was rarely used, since the large frequency excursions often caused the BUC electronics to lose lock of the resonance. Spectrum **A** in Figure 3.6 was measured using an FM amplitude approximately two-thirds of the maximum. The precise loss of signal due to using a lower than optimal FM amplitude is not known. The single pass experiment used the conventional laser amplitude (intensity) modulation method. Comparison of the signal-to-noise ratios of the two spectra (4500:15) leads one to believe the gain of the cavity was 300. However, the signal in spectrum **B** was enhanced by a factor of approximately 2.5, by using a cylindrical lens to create a better overlap between the molecular beam and the laser. Taking this into account, the BUC had a gain of approximately 750, close to the estimated value of 773 based on the lock-point position of 75% of the transmission peak.

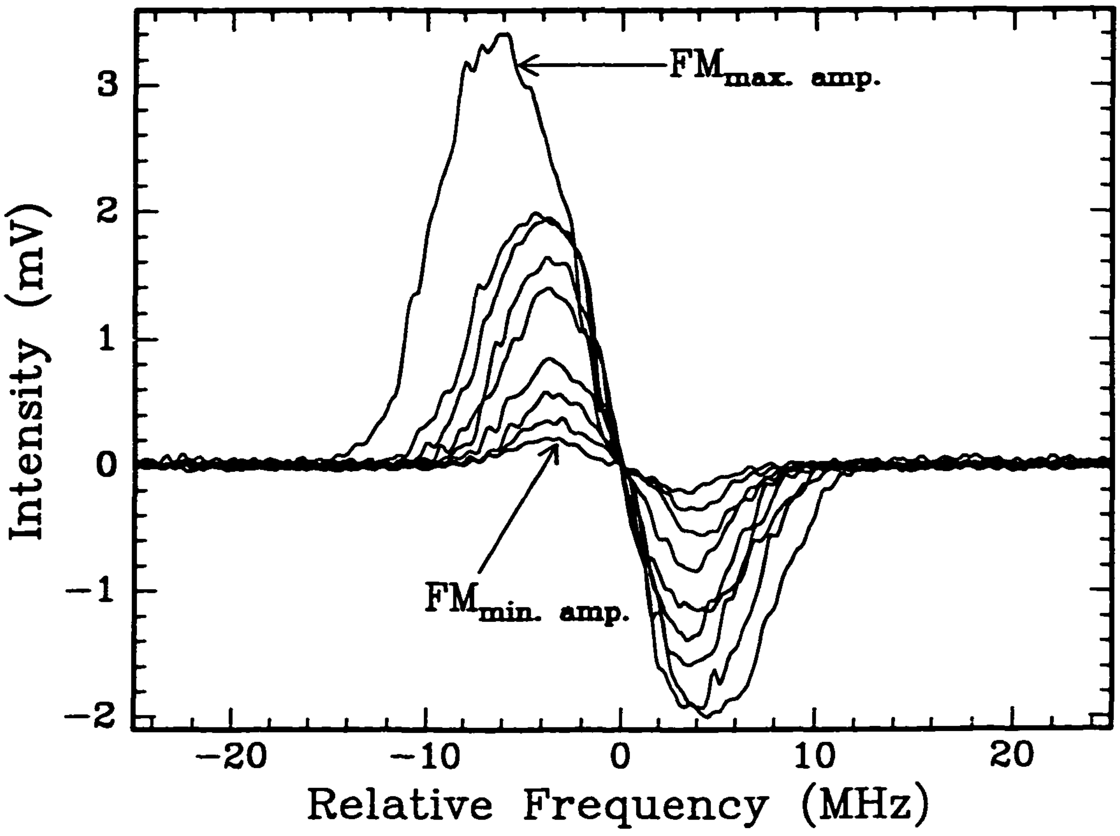

Figure 3.8: The dependence of the line shape on the frequency modulation amplitude for the R(4) $\nu_2 + 3\nu_3$ ro-vibrational transition of acetylene. The maximum signal was measured using a frequency modulation amplitude of 5.4 MHz (FM$_{\text{max. amp.}}$), resulting in a strongly asymmetric line shape. The most symmetric line shape was produced with minimal frequency modulation amplitude (FM$_{\text{min. amp.}}$), however the signal-to-noise ratio was only slightly better than 2:1. Increasing the FM amplitude, not only increased the measured signal, but also increased the line width. It also had the adverse affect of destabilising the BUC.

Chapter 4

Hydrogen Fluoride

4.1 Introduction

The dipole moment function of hydrogen fluoride continues to be a topic of interest, partly because the molecule is sufficiently small to be amenable to high quality theoretical treatment, and partly because of the availability of significant amounts of relevant experimental data. In addition, the central role of emission from vibrationally excited hydrogen fluoride in chemical lasers [58–60], and as a probe of reaction dynamics provides incentive for as quantitative an understanding of the dipole moment of hydrogen fluoride as is possible.

The dipole moment function obtained by Werner and Rosmus using highly correlated SCEP/CEPA (Self Consistent Electron Pair/Coupled Electron Pair Approximation) wavefunctions long provided the best agreement between *ab initio* and experimental functions up to the $v = 9$ level [22]. More recently, Zemke *et al.* have taken a potential energy function of hydrogen fluoride based on spectroscopic measurements [61] and imposed upon it the proper long range behaviour by including both dispersion and exchange effects [62]. This potential energy function was then combined with a new *ab initio* dipole moment function, complete for all internuclear distances, to calculate line intensities and dipole moments [63]. The results were in excellent agreement with experimental data, particularly that of Sileo and Cool [64]. For high levels of vibrational excitation, the results of Zemke *et al.* represent a marked improvement over those of Werner and Rosmus. That this improvement is largely due to the more realistic potential energy function used can be inferred from the fact that the dissociation limit determined by this function (D_e = 49,362±5 cm^{-1}) differs markedly from that obtained from the full CI (Configuration Interaction), "benchmark" calculations of Bauschlicher *et al.* (48,960 cm^{-1}) [65].

A calculation using density functional techniques [66], which are computationally more efficient, was found to improve upon the results obtained from self consistent field methods which neglect electron correlation. However, the calculations were confined to the equilibrium geometry and seem less accurate than those performed using the SCEP/CEPA method, which included large excursions from the equilibrium geometry.

Sileo and Cool performed an extensive series of measurements of overtone emission intensities for hydrogen fluoride [64], and these have been the main source of experimental data to which theoretical results have been compared. Many of the systematic errors inherent in measuring emission intensities are less important in Sileo and Cool's analysis which only uses ratios of such intensities. However, one experimentally determined dipole moment is necessary to establish absolute values of dipole moments from Sileo and Cool's data [64]. Measurements of the dipole moments of the $v = 0$ and $v = 1$ states of hydrogen fluoride provide a second source of experimental information which, although more limited, is both more precise and more accurate than that of emission intensities [67,68]. In addition, the intensity of the fundamental vibrational absorption of hydrogen fluoride has been carefully re-measured, once again providing precise but limited information [69]. Comparison between experiment and theory is most conveniently done by converting the combined body of experimentally measured quantities, appropriately weighted, into an experimental dipole moment function. This is normally expressed as a power series in the internuclear distance, preferably augmented by some expression to enable extrapolation outside of the range of internuclear distances covered by the experiment. Ogilvie has published the coefficients of such a power series up to sixth order, and has also carefully analysed standard errors for these coefficients using a Monte Carlo method [70].

Zemke *et al.* claim that their calculated dipole moments are numerically significant to 10^{-4} Debye. This precision exceeds that of available infrared intensity measurements which are also subject to systematic errors on the order of a few percent. Therefore, it is of interest to measure the dipole moments of hydrogen fluoride in higher vibrational states than the $v = 0$ and $v = 1$ states so far reported. The apparatus described in this thesis is capable of interrogating the $v = 3$ state and, with some modifications, higher vibrational states.

4.2 Experimental Results and Data Analysis

A Faraday rotator was used to rotate the output polarisation of the laser electric field 45° with respect to the Stark electric field, to allow observation of transitions obeying $\Delta M = 0, \pm 1$ selection rules (Section 1.2.1, page 13).

A 5% hydrogen fluoride in helium gas mixture and a stagnation pressure optimised at 0.5 atm were used to produce the molecular beam. The HF rotational line positions for the $v = 3 \leftarrow 0$ vibrational transition were located using results from Fishburne and Rao [71] and the Burleigh Wavemeter to set the laser frequency. The $J = 2 \leftarrow 1$ ro-vibrational transition at 11441.41 cm^{-1} was split with Stark fields of approximately 40 kV/cm. A typical spectrum is shown in Figure 4.1 with the transitions labelled according to Figure 4.2. Absolute frequencies were not needed and the Stark electrode spacing did not need to be known exactly, because as is shown later only the ratio of the line splittings $(b - c)/(a - b)$ was of interest. This ratio was found to be 1.6793 ± 0.0018 experimentally, gathered from the analysis of forty separate scans.

For a diatomic molecule in an electric field, the electrical energies of the J and M

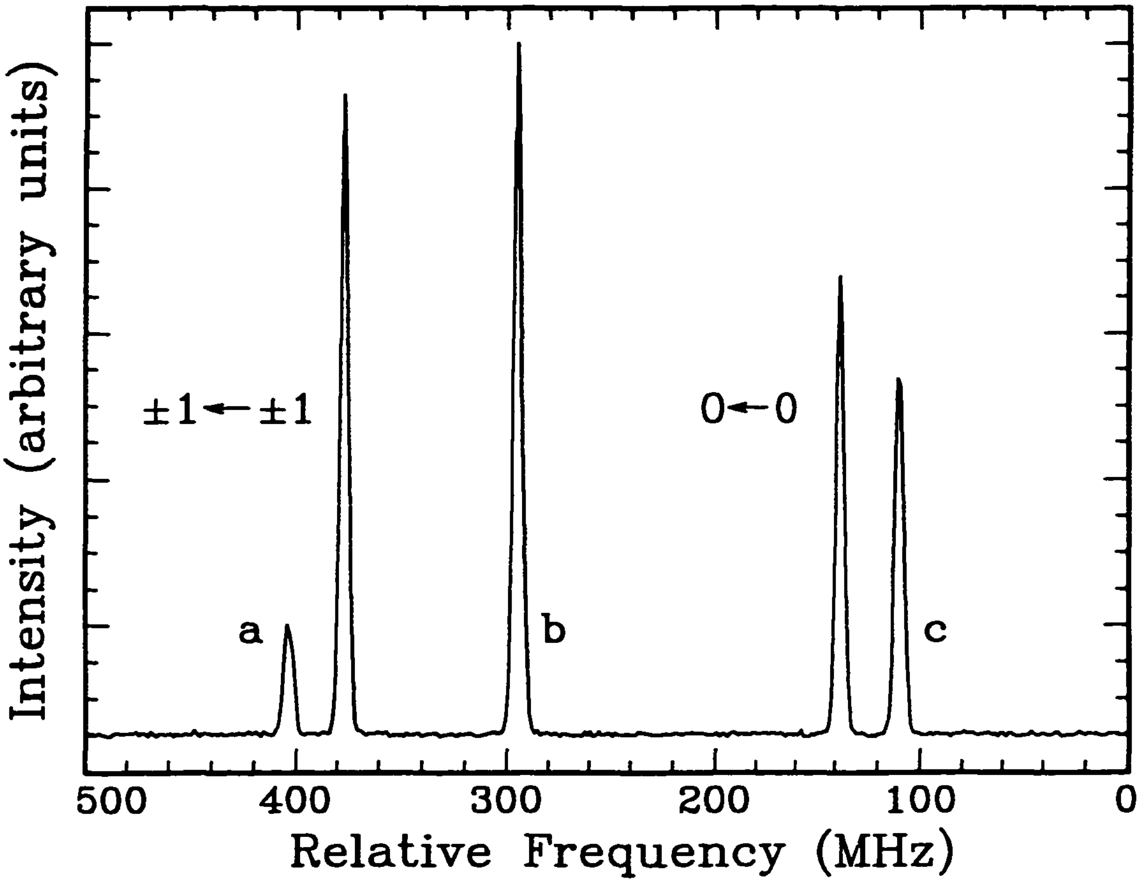

Figure 4.1: Experimental Stark split spectrum of the R(1) transition of the $v = 3$ band of hydrogen fluoride, induced by an applied field of 36 kV/cm. The $\Delta M = \pm 1$ transitions are labelled **a**, **b** and **c** as identified in Figure 4.2.

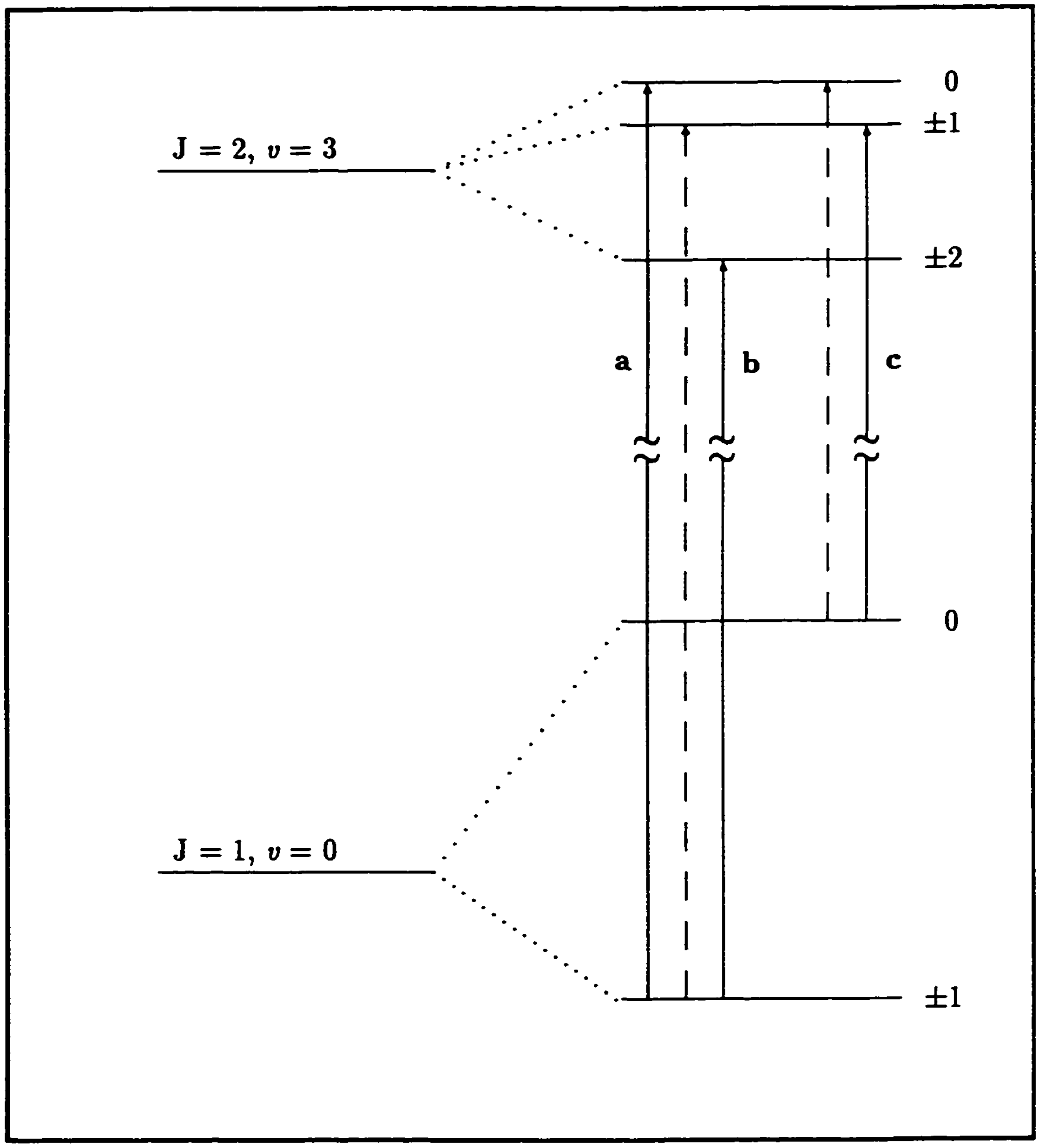

Figure 4.2: Energy levels and transitions corresponding to the Stark split spectrum of hydrogen fluoride depicted in Figure 4.1.

levels will be given by [19, 31]

$$W_{v,J,M} = W^{(2)}_{v,J,M} + W^{(PA)}_{v,J,M} + W^{(4)}_{v,J,M}, \tag{4.1}$$

where the dominant term is the second order dipole moment–applied electric field interaction [30] :

$$W^{(2)}_{v,J,M} = \frac{\mu_v^2 F^2}{2hB_v} \frac{J(J+1) - 3M^2}{J(J+1)(2J-1)(2J+3)} \tag{4.2}$$

The dipole moment (μ_v) and the rotational constant (B$_v$) are for the specified vibrational state v, and the appropriate selection rules for the present experiment are given in Figure 4.2. The mean polarisability induced shift ($-\frac{1}{2}\alpha_v F^2$) has been left out of the Equation 4.1, not because it is negligible, but because only differences in transitions are of interest. The shift is not M_J dependent and will therefore cancel when the differences $\mathbf{a} - \mathbf{b}$ and $\mathbf{b} - \mathbf{c}$ are taken. The effects due to the polarisability anisotropy ($W^{(PA)}_{v,J,M}$) and the fourth order dipole–applied electric field interaction $W^{(4)}_{v,J,M}$ are less than 0.5% for applied electric fields on the order of 40 kV/cm. It is therefore not necessary to know the exact electric field for the fourth order correction. The electric field was estimated from the second order term after calculating the upper state dipole moment based on second order perturbations alone.

The effects of the anisotropy of the polarisability are compensated for by applying the following correction [31]

$$W_{J,M}^{(PA)} = -\frac{(\alpha_{\parallel} - \alpha_{\perp})F^2}{3}\frac{J(J+1) - 3M^2}{(2J+3)(2J-1)}, \tag{4.3}$$

where $(\alpha_{\parallel} - \alpha_{\perp})$ or $\Delta\alpha$ is the anisotropy of the polarisability of the molecule. The vibrational dependence of $\Delta\alpha$ has been ignored, since $W_{J,M}^{(PA)}$ is much less than $W_{v,J,M}^{(2)}$. Omitting the contribution from $W_{v,J,M}^{(4)}$, one can write the Stark energies as

$$W_{v,J,M} = \left[\frac{C_S\mu^2F^2}{2B_vJ(J+1)} - \frac{C_P\Delta\alpha F^2}{3}\right]\left[\frac{J(J+1) - 3M^2}{(2J-1)(2J+3)}\right], \tag{4.4}$$

where C_S and C_P are conversion constants that give units of MHz for $W_{v,J,M}$ (see Table 4.1). The equations for the individual M_J transitions, **a**, **b** and **c**, depicted in Figure 4.1 are as follows:

$$\mathbf{a} = \left[\frac{C_S\mu_3^2}{42B_3} + \frac{C_S\mu_0^2}{20B_0} - \frac{17C_P\Delta\alpha}{105}\right]F^2 \tag{4.5}$$

$$\mathbf{b} = \left[\frac{C_S\mu_0^2}{20B_0} - \frac{C_S\mu_3^2}{42B_3} + \frac{3C_P\Delta\alpha}{105}\right]F^2 \tag{4.6}$$

$$\mathbf{c} = \left[\frac{C_S\mu_0^2}{20B_0} - \frac{C_S\mu_3^2}{42B_3} + \frac{9C_P\Delta\alpha}{105}\right]F^2 \tag{4.7}$$

With a little algebraic manipulation, the excited state dipole moment can be expressed in terms of the ratio $(\mathbf{b} - \mathbf{c})/(\mathbf{a} - \mathbf{b})$, the ground state dipole moment and the appropriate rotational constants:

$$\mu_3^2 = \frac{B_3}{C_S}\left[\frac{63\mu_0^2}{20B_0}C_S + \Delta\alpha C_P\left(4\left(\frac{\mathbf{b}-\mathbf{c}}{\mathbf{a}-\mathbf{b}}\right) - \frac{42}{35}\right)\right]\left[\left(\frac{\mathbf{b}-\mathbf{c}}{\mathbf{a}-\mathbf{b}}\right) + \frac{3}{4}\right]^{-1} \tag{4.8}$$

where C_S and C_P are the second order Stark and polarisability constants, respectively.

Once the second order corrections had been evaluated the electric field was estimated by comparison of the measured splitting (a − c) with the splitting calculated from the second order determination of the dipole. The fourth order correction was then calculated using Equation 4.9 [36],

$$\begin{aligned} W^{(4)}_{v,J,M} &= \frac{\mu_v^4 F^4}{8h^3B_v^3}\left[-\frac{[(J+1)^2-M^2][(J+2)^2-M^2]}{(2J+1)(2J+5)(J+1)^2(2J+3)^3}\right. \\ &+ \frac{[(J-1)^2-M^2][J^2-M^2]}{(2J-3)(2J+1)J^2(2J-1)^3} + \frac{[J^2-M^2][(J+1)^2-M^2]}{(2J-1)(2J+3)(2J+1)^2J^2(J+1)^2} \\ &+ \left.\frac{[(J+1)^2-M^2]^2}{(2J+3)^2(2J+1)^2(J+1)^3} - \frac{[J^2-M^2]^2}{(2J+1)^2(2J-1)^2J^3}\right]. \end{aligned} \tag{4.9}$$

Table 4.1 lists the required variables and the results of all of the calculations.

4.3 Discussion

Figure 4.3 provides a convenient format for assessing the information available concerning the dependence upon vibrational quantum number of the dipole moment of hydrogen fluoride. In this figure, the theoretical results of Zemke *et al.* [63] have been subtracted from the corresponding experimental values. The circles denote measure-

Table 4.1: Experimentally Measured Dipole Moment for Hydrogen Fluoride

Constant	Value	Units	Reference
B_0	20.5597299	cm^{-1}	[72]
B_3	18.26930	cm^{-1}	Calculated from [72]
μ_0	1.826567	Debye	[68]
$\alpha_{\parallel} - \alpha_{\perp}$	0.220±0.020	$10^{-24}cm^3$	[73]
C_S	0.253415	MHz $D^{-2}(V/cm)^{-2}$	
C_P	1.67917×10^{15}	MHz $cm^{-3}(V/cm)^{-2}$	
F	36	kV cm^{-1}	
μ_3	1.9612	Debye	From Equation 4.8
μ_3	1.9614±0.0021	Debye	Corrected for Equation 4.9

ments made using Stark splitting of spectra using various molecular beam techniques : the diamonds are dipole moments as reported by Sileo and Cool. The discrepancy between the two sets of data arises because of the incorrect value of μ_e used in their analysis. It is perfectly valid to adjust the diamonds upward a constant amount so that the two sets of data overlap at $v = -1/2$; it is essential to make such an adjustment before attempting comparisons with theoretical predictions of the quality claimed by Zemke *et al.* After the adjustment is made, the two sets of experimental data are in excellent agreement and it seems clear that the theory underestimates μ_e (1.8022 ± 0.0001) by 0.004 Debye and overestimates the rate at which μ_v increases with v at least for $v < 4$. Nevertheless, the agreement over the full range of available data of better than ± 0.005 Debye is most impressive.

The triangle in Figure 4.3 (page 68) represents the value for μ_2 calculated by Muenter from an experimental dipole moment function based on Molecular Beam

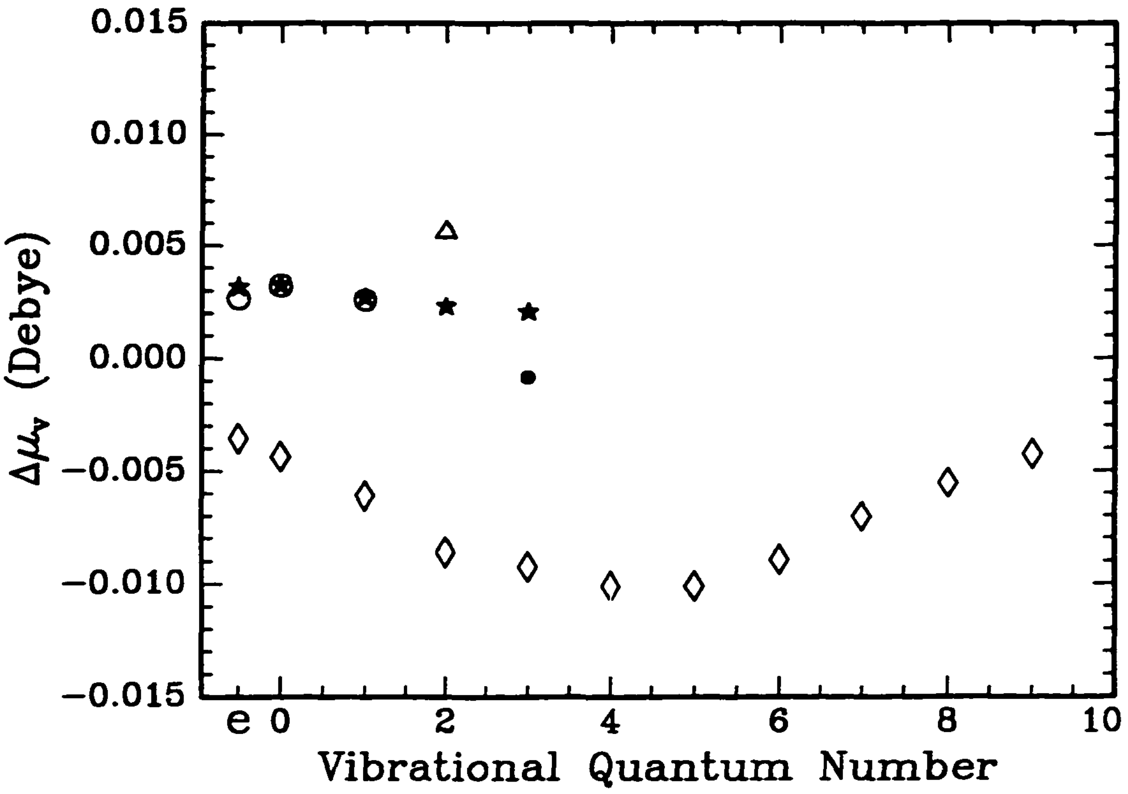

Figure 4.3: Plot of the difference between the experimentally determined dipole moments and the *ab initio* dipole moment data taken from Zemke *et al.* [63] for hydrogen fluoride (see Table 4.2). The ◇ represent data from Sileo and Cool [64], the ○ are from Muenter *et al.* [68] and the ● represents the present work, and the △ was calculated by Muenter *et al.* based on the, at the time, existing experimental data. To date no direct experimental measurement of the $v = 2$ dipole moment exists. The ★ were calculated using the Herman and Short theory together with values for the M_j and a_j taken from Ogilvie [70]. e represents the equilibrium position.

Electric Resonance measurements of μ_0, μ_1, and the transition dipole moments $\langle 0|\mu|1\rangle$ and $\langle 0|\mu|3\rangle$ [68]. It seems clear that this value of 1.9232 Debye for μ_2 is in error: in fact, the *ab initio* value of 1.9176 is five times closer to the interpolated value of 1.9185 ± 0.0001 Debye established by the present measurement of μ_3. The problems encountered in establishing dipole moment functions have been discussed by Muenter *et al.*: what follows examines the accuracy with which dipole moments may be extracted from these functions.

Experimental values for the dipole moment, observed for several vibrational states, are most conveniently expressed as a power series in $(v + {}^1\!/\!_2)$ where v is the vibrational quantum number [68, 74, 75].

$$\mu_v = \sum P_j \left(v + \frac{1}{2}\right)^j \tag{4.10}$$

The dipole moment function, on the other hand, is normally expressed as a Taylor series in the reduced internuclear displacement from equilibrium [64, 70].

$$\mu(x) = \sum M_j\, x^j \qquad ; \qquad x = \frac{(R - R_e)}{R_e} \tag{4.11}$$

With this choice of dipole moment function, expressions for dipole moments and transition dipole moments can be written as a series of linear equations and thus experimental values of these quantities can be used to determine a set of values of M_j. The maximum value of j in either approach is determined by the quantity and

Table 4.2: Experimental and Theoretical Dipole Moments for Hydrogen Fluoride

	Theory		Experiment		
(Debye)	Zemke *et al.* [63]	Ogilvie *et. al.* [70]	Sileo & Cool [64]	Muenter *et al.* [68]	This Work
μ_e	1.7996	1.8027	1.796	1.80309	1.8022
μ_0	1.8234	1.8265	1.819	1.826567	
μ_1	1.8711	1.8738	1.865	1.873693	
μ_2	1.9176	1.9199	1.909	1.9232	1.9185
μ_3	1.9622	1.9643	1.953		1.9614

quality of the available experimental data. Because the number of measurements of transition intensities greatly exceeds the number of measurements of vibrationally state specific dipole moments, the power series (Equation 4.11) is the most commonly used. Indeed, for hydrogen fluoride the present measurement allows, for the first time, the determination of P_2 (Table 4.4) whereas values for M_j up to $j = 6$ are available in the literature. A third form of expansion, the "wavefunction approximation", has been shown to be equivalent to the power series (Equation 4.11) [70].

Interconversion between the coefficients of the two expansions is possible following the paper of Herman and Short who showed that P_j may be expressed in terms of M_j, (B_e/ω_e), and a_j, the potential energy coefficients in the Dunham function [75, 76]. Previous work seems to have over-estimated the rate of convergence of this approach, partly perhaps in deference to the tedious algebra involved. Programs capable of implementing symbolic computation have removed this latter obstacle: accordingly, a Maple^{TM} program was written to re-derive the expressions given by Herman and

Short, but including terms up to $(B_e/\omega_e)^4$ and Dunham potential energy coefficients up to a_6. These limits were established by the non-availability of expressions for the Dunham coefficients higher than Y_{40}. Analytical expressions for P_j ($j = 0$ through 4) are given in Table 4.5 at the end of this Chapter and Table 4.3 provides the numerical expressions for P_j as functions of M_j obtained by substituting the values of a_i given by Ogilvie for hydrogen fluoride. As a test of these expressions, the dipole moment function of Zemke *et al.* was fit to a power series, and the resultant values of M_j substituted into the expressions in Table 4.3 to obtain values of P_j. These were then used to calculate values of μ_v ($v = 0$ through 3) which agreed to within 10^{-3} Debye of the corresponding values calculated by Zemke *et al.*, indicating that both the values of a_j and expressions for P_j are satisfactory for the present purpose. In Table 4.4 a comparison is made between the P_j values based on Ogilvie's M_j and the expressions in Table 4.3, and the values obtained directly from Equation 4.10 and experimentally determined dipole moments.

The values of M_j obtained by Ogilvie from a careful analysis of dipole moments and infrared intensities for hydrogen fluoride were then used, in a similar manner, to calculate values of μ_v for $v = -1/2$ and 0 through 3. These results have been inserted into Figure 4.3 as solid stars. It can be seen that the M_j values suggested by Ogilvie provide better agreement with the trend established by the present measurement than that obtained by Muenter. Even so, the agreement seems to be deteriorating with increasing v.

Table 4.3: Numerical Expressions for P_j as a Function of M_j

P_0	$M_0 + 4.405 \times 10^{-5} M_1 + 4.687 \times 10^{-5} M_2 + 1.685 \times 10^{-5} M_3 + 1.602 \times 10^{-6} M_4$
P_1	$3.423 \times 10^{-2} M_1 + 5.068 \times 10^{-3} M_2 + 2.985 \times 10^{-6} M_3 + 9.442 \times 10^{-7} M_4 + 1.158 \times 10^{-7} M_5 + 4.507 \times 10^{-9} M_6$
P_2	$4.689 \times 10^{-4} M_1 + 7.074 \times 10^{-4} M_2 + 1.446 \times 10^{-4} M_3 + 6.519 \times 10^{-6} M_4 + 2.793 \times 10^{-8} M_5 + 3.537 \times 10^{-9} M_6$
P_3	$9.440 \times 10^{-6} M_1 + 1.880 \times 10^{-5} M_2 + 1.220 \times 10^{-5} M_3 + 2.449 \times 10^{-6} M_4 + 1.706 \times 10^{-7} M_5 + 3.606 \times 10^{-9} M_6$
P_4	$-5.000 \times 10^{-6} M_1 + 2.034 \times 10^{-7} M_2 + 4.383 \times 10^{-7} M_3 + 1.790 \times 10^{-7} M_4 + 3.230 \times 10^{-8} M_5 + 2.622 \times 10^{-9} M_6$

Table 4.4: Comparison of the Literature and Present Values for P_j

P_j	Ogilvie *et al.* [70]	This Work
P_0	1.8027	1.8022
P_1	0.04774	0.04931
P_2	-1.209×10^{-4}	-0.001091
P_3	-8.958×10^{-5}	
P_4	-1.677×10^{-6}	

Table 4.5: Analytical Expressions for P_j

$$\begin{aligned} P_0 &= M_0 + \left[\left(-\frac{21\,a_1{}^3}{8} + \frac{23\,a_1\,a_2}{4} - \frac{15\,a_3}{4}\right) M_1 \right. \\ &+ \left.\left(\frac{7\,a_1{}^2}{4} - \frac{3\,a_2}{2}\right) M_2 - \frac{7}{4} a_1\,M_3 + \frac{3}{2} M_4\right] \frac{B_e{}^2}{\omega_e{}^2} \end{aligned} \tag{4.12}$$

$$\begin{aligned} P_1 &= \left(-3\,a_1\,M_1 + 2\,M_2\right) \frac{B_e}{\omega_e} + \left[\left(-\frac{31185\,a_1{}^5}{256} + \frac{14259\,a_1{}^3 a_2}{32} - \frac{5145\,a_1{}^2 a_3}{16}\right.\right. \\ &+ \left.\frac{715\,a_2\,a_3}{4} + \frac{795\,a_1\,a_4}{4} - \frac{4677\,a_1\,a_2{}^2}{16} - \frac{175\,a_5}{2}\right) M_1 \\ &+ \left(\frac{10395\,a_1{}^4}{128} + \frac{335\,a_2{}^2}{8} + \frac{475\,a_1\,a_3}{4} - \frac{75\,a_4}{2} - \frac{3213\,a_1{}^2 a_2}{16}\right) M_2 \\ &+ \left(-\frac{95\,a_3}{2} + \frac{459\,a_1\,a_2}{4} - \frac{1155\,a_1{}^3}{16}\right) M_3 + \left(-\frac{67\,a_2}{2} + \frac{459\,a_1{}^2}{8}\right) M_4 \\ &- \left.\frac{95}{2} a_1\,M_5 + 25\,M_6\right] \frac{B_e{}^3}{\omega_e{}^3} \end{aligned} \tag{4.13}$$

$$
\begin{aligned}
P_2 &= \Bigg[\left(39\, a_1\, a_2 - 15\, a_3 - \frac{45\, a_1^{\,3}}{2}\right) M_1 + \left(15\, a_1^{\,2} - 6\, a_2\right) M_2 - 15\, a_1\, M_3 \\
&+ 6\, M_4\Bigg] \frac{B_e^{\,2}}{\omega_e^{\,2}} + \Bigg[\Bigg(\frac{1393515\, a_2\, a_1^{\,5}}{64} - \frac{1890135\, a_2^{\,2} a_1^{\,3}}{64} + \frac{948525\, a_1^{\,2} a_3\, a_2}{32} \\
&+ \frac{174015\, a_4\, a_1^{\,3}}{16} + \frac{72255\, a_2^{\,3} a_1}{8} - 11760\, a_4\, a_1\, a_2 - 5805\, a_1\, a_3^{\,2} - \frac{4390155\, a_1^{\,7}}{1024} \\
&- \frac{84285\, a_2^{\,2} a_3}{16} + \frac{11655\, a_5\, a_2}{4} + \frac{10935\, a_4\, a_3}{4} + 3465\, a_1\, a_6 - \frac{108885\, a_5\, a_1^{\,2}}{16} \\
&- \frac{4063725\, a_1^{\,4} a_3}{256} - \frac{2205\, a_7}{2}\Bigg) M_1 + \Bigg(\frac{1463385\, a_1^{\,6}}{512} - \frac{719955\, a_1^{\,4} a_2}{64} - \frac{1707\, a_2^{\,3}}{2} \\
&- 7335\, a_1\, a_2\, a_3 - \frac{8535\, a_1^{\,2} a_4}{2} + \frac{2655\, a_2\, a_4}{2} + \frac{3255\, a_3^{\,2}}{4} + \frac{119325\, a_1^{\,3} a_3}{16} \\
&+ \frac{4095\, a_1\, a_5}{2} + \frac{310065\, a_1^{\,2} a_2^{\,2}}{32} - 490\, a_6\Bigg) M_2 + \Bigg(-\frac{1365\, a_5}{2} + \frac{8535\, a_1\, a_4}{4} \\
&+ \frac{7335\, a_2\, a_3}{4} - \frac{71595\, a_1^{\,2} a_3}{16} - \frac{62013\, a_1\, a_2^{\,2}}{16} + \frac{239985\, a_1^{\,3} a_2}{32} - \frac{627165\, a_1^{\,5}}{256}\Bigg) M_3 \\
&+ \left(-\frac{885\, a_4}{2} + \frac{5121\, a_2^{\,2}}{8} + \frac{7335\, a_1\, a_3}{4} - \frac{62013\, a_1^{\,2} a_2}{16} + \frac{239985\, a_1^{\,4}}{128}\right) M_4 \\
&+ \left(-\frac{1085\, a_3}{2} + \frac{7335\, a_1\, a_2}{4} - \frac{23865\, a_1^{\,3}}{16}\right) M_5 \\
&+ \left(-\frac{885\, a_2}{2} + \frac{8535\, a_1^{\,2}}{8}\right) M_6\Bigg] \frac{B_e^{\,4}}{\omega_e^{\,4}} \qquad (4.14)
\end{aligned}
$$

$$
\begin{aligned}
P_3 &= \Bigg[\left(-\frac{19035\, a_1^{\,5}}{64} + \frac{7545\, a_1^{\,3} a_2}{8} - \frac{2055\, a_1\, a_2^{\,2}}{4} - \frac{2175\, a_1^{\,2} a_3}{4} + 225\, a_2\, a_3 - 70\, a_5 \right. \\
&+ \left. 255\, a_1\, a_4\right) M_1 + \left(\frac{6345\, a_1^{\,4}}{32} - \frac{1575\, a_1^{\,2} a_2}{4} + \frac{85\, a_2^{\,2}}{2} + 175\, a_1\, a_3 - 30\, a_4\right) M_2 \\
&+ \left(-\frac{705\, a_1^{\,3}}{4} + 225\, a_1\, a_2 - 70\, a_3\right) M_3 + \left(\frac{225\, a_1^{\,2}}{2} - 34\, a_2\right) M_4 \\
&- 70\, a_1\, M_5 + 20\, M_6\Bigg] \frac{B_e^{\,3}}{\omega_e^{\,3}} \qquad (4.15)
\end{aligned}
$$

$$
\begin{aligned}
P_4 \;=\; & \left[\left(-\frac{2430855\, a_1{}^7}{512}+\frac{697095\, a_2\, a_1{}^5}{32}-\frac{839475\, a_2{}^2 a_1{}^3}{32}-315\, a_7+\frac{27195\, a_2{}^3 a_1}{4}\right.\right.\\
+\; & \frac{357825\, a_1{}^2 a_3\, a_2}{16}+\frac{61875\, a_4\, a_1{}^3}{8}-\frac{24945\, a_2{}^2 a_3}{8}-7080\, a_4\, a_1\, a_2-\frac{7455\, a_1\, a_3{}^2}{2}\\
-\; & \left.\frac{30345\, a_5\, a_1{}^2}{8}+\frac{2415\, a_5\, a_2}{2}+\frac{2715\, a_4\, a_3}{2}+1470\, a_1\, a_6-\frac{1753425\, a_1{}^4 a_3}{128}\right) M_1\\
+\; & \left(\frac{810285\, a_1{}^6}{256}-\frac{348975\, a_1{}^4 a_2}{32}+\frac{124725\, a_1{}^2 a_2{}^2}{16}+\frac{48825\, a_1{}^3 a_3}{8}-375\, a_2{}^3\right.\\
-\; & \left.4830\, a_1\, a_2\, a_3-2715\, a_1{}^2 a_4+495\, a_2\, a_4+\frac{945\, a_3{}^2}{2}+945\, a_1\, a_5-140\, a_6\right) M_2\\
+\; & \left(-\frac{347265\, a_1{}^5}{128}+\frac{116325\, a_1{}^3 a_2}{16}-\frac{24945\, a_1\, a_2{}^2}{8}-\frac{29295\, a_1{}^2 a_3}{8}+\frac{2415\, a_2\, a_3}{2}\right.\\
+\; & \left.\frac{2715\, a_1\, a_4}{2}-315\, a_5\right) M_3+\left(\frac{116325\, a_1{}^4}{64}-\frac{24945\, a_1{}^2 a_2}{8}+\frac{1125\, a_2{}^2}{4}\right.\\
+\; & \left.\frac{2415\, a_1\, a_3}{2}-165\, a_4\right) M_4+\left(-\frac{9765\, a_1{}^3}{8}+\frac{2415\, a_1\, a_2}{2}-315\, a_3\right) M_5\\
+\; & \left.\left(\frac{2715\, a_1{}^2}{4}-165\, a_2\right) M_6\right]\frac{B_e{}^4}{\omega_e{}^4}
\end{aligned}
\tag{4.16}
$$

Chapter 5

Acetylene $\nu_1 + 3\nu_3$

5.1 Introduction

The ro-vibrational spectrum of the ground electronic state of the acetylene molecule has been studied extensively over the past 70 or so years. The molecule's simple linear geometry has lured many a spectroscopist, resulting in a plethora of literature detailing its spectrum and the difficulties that have arisen during the analyses. In fact, Herman *et al.* listed no fewer than 127 measured vibrational bands between 600–12000 cm^{-1} alone during their attempt to perform a detailed analysis of acetylene's vibrational structure [2]. The object of this recent analysis was to find a model that could adequately describe the irregular vibrational energy pattern at higher energies. The reason for the irregularities was attributed to the incredible congestion at higher levels of vibrational excitation. The energy regime accessible by the Ti:Sapphire laser alone encompasses 25 vibrational bands, of which only ten have been assigned to any particular vibrational transition [9, 47, 77, 78]. Extensive calculations, such as those by Herman *et al.*, have been more successful in assigning vibrational state labels by dividing up the 127 input energies into "clusters" of vibrational states [2] thought to have been coupled by Fermi [28], Darling–Dennison [79] and Coriolis [80, 81] resonances. The criteria for the inclusion of a vibrational state within a particular vibrational "cluster" were based upon a set of pseudoquantum numbers developed by Kellman [82, 83]. Acetylene has three such pseudoquantum numbers. The first, $n_s = (V_1 + V_2 + V_3)$, is the total stretching quantum number, which is followed by a total vibrational angular momentum quantum number, $n_\ell = (\ell_4 + \ell_5)$. The third quantum number, $n_r = (5V_1 + 3V_2 + 5V_3 + V_4 + V_5)$, fixes the energy of the vibrational cluster and, hence, imparts a "resonance condition" [84]. The "cluster" number $\{n_s, n_r, n_\ell\}$ combined with the gerade/ungerade symmetry label uniquely defines a set of vibrational states that are coupled via anharmonic resonances [2]. This thesis will examine the effects various coupling mechanisms have on the electrical properties of acetylene.

The application of external electric fields can also open up new mechanisms for state to state coupling, particularly for molecules as symmetric as acetylene. This chapter deals with the analysis of a Stark field induced interaction between two highly excited vibrational overtone states of acetylene. In the case of acetylene, a direct transition from the ground state to the interacting state must be forbidden. Hence, the Stark field will allow the measurement of a state that cannot be measured directly by infrared spectroscopy. Not only will the measurement of the polarisability tensor of the optically excited state be possible, but also the measurement of the transition dipole moment connecting the two interacting states and their relative band origins. Reilly has carried out such experiments on methane, measuring vibrationally induced dipole moments [26, 48]. Pate has described similar experiments on 2-propyn-1-ol, and discussed the complexities to be expected from extremely high state densities [85].

The following results are a direct test of the local mode calculations of Child and Halonen [11].

5.2 Experimental Details

The molecular beam was prepared by expanding a mixture of 10% acetylene in helium at a stagnation pressure of 0.5 atmosphere (Figure 2.4). The ro-vibrational transitions of the $\nu_1 + 3\nu_3$ band (12675.63 cm^{-1}) were located using the photoacoustic cell and tables of previously measured transition frequencies [86].

Because acetylene has no electric dipole moment, extremely high electric fields ($>$ 300 kV/cm) are necessary to induce Stark splittings, even with the high resolution (approximately 5 MHz) of the molecular beam spectrometer. The Stark electrode gap was determined by calibration against the hydrogen fluoride $v = 0$ electric dipole moment [68] and found to be 0.6853±0.0007 mm.

The Stark shift of the transition energies was sufficient to allow the measurement of the unperturbed and the Stark split rotational spectrum during the same laser scan. This was accomplished by turning the Stark field off once the laser had scanned through the Stark field perturbed spectrum, thereby recording the field free transition within the same scan (Figure 5.1). The Stark induced shift as well as the splittings were recorded using this technique. All Stark shifts and splittings were found to be quadratic in electric field within the precision of the experiment for the $\nu_1 + 3\nu_3$ combination band.

Measurements were made on the R(0–5), R(7), P(1), and P(2) ro-vibrational transitions of the $\nu_1 + 3\nu_3$ band. A typical Stark spectrum of the $\nu_1 + 3\nu_3$ R(1) transition is depicted in Figure 5.1 with the transitions labelled according to Figure 5.2. The laser electric field polarisation was rotated 90° with respect to the Stark Field in order to observe only the $\Delta M = \pm 1$ transitions.

The relative intensities of infrared (500–5000 cm^{-1}) vibrational bands of acetylene were measured using a BOMEM DA3.002 Fourier transform infrared spectrometer. The rotational lines were broadened to 0.13 cm^{-1} (FWHM) with approximately 705 Torr of helium buffer gas and measured with a resolution of 0.05 cm^{-1}. The absolute band intensities were measured to be 701 cm^{-2} atm^{-1} (ν_5) and 78.3 cm^{-2} atm^{-1} ($\nu_4 + \nu_5$) based upon the previously measured value of 223.22 cm^{-2} atm^{-1} for the ν_3, $\nu_2 + \nu_4 + \nu_5$ Fermi diad [87].

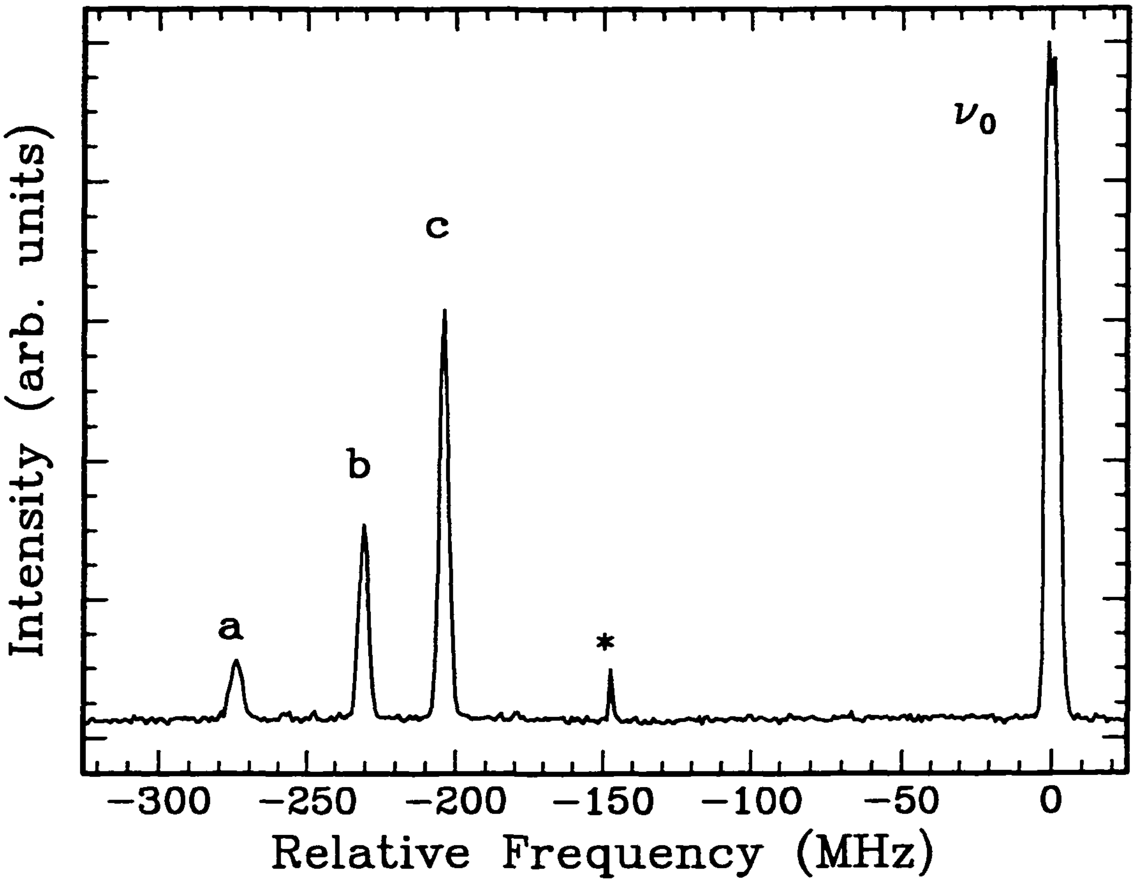

Figure 5.1: The Stark field perturbed spectrum of the $\nu_1+3\nu_3$ R(1) transition with an applied field of 265.5 kV/cm. The transitions a, b, and c are labelled according to Figure 5.2. The "spike" in the spectrum, indicated with the ⋆, was generated when the applied field was turned off. The field-free transition is labelled as ν_0.

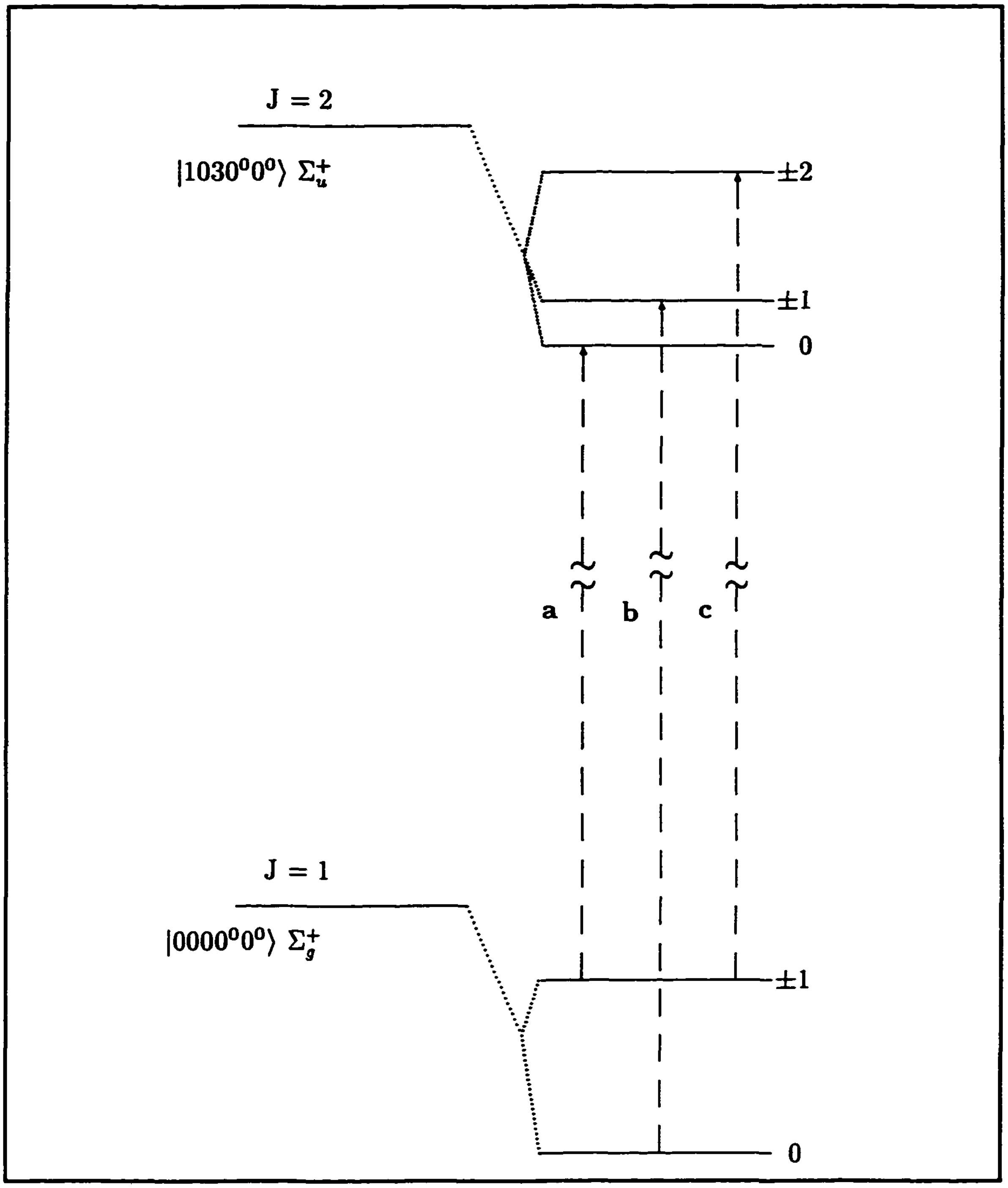

Figure 5.2: Allowed transitions in the presence of a Stark field for the $\nu_1 + 3\nu_3$ R(1) rotational-vibrational transition following $\Delta M = \pm 1$ selection rules. 04^- is the local mode notation for the $|1030^00^0\rangle$ vibrational state.

5.3 Results

For a linear molecule having a zero permanent electric dipole moment, in a uniform electric field (F), the electrical energies of the J, M levels can be described by [19]

$$W_{vJM}(F) = -\frac{1}{2}\alpha_v F^2 - \frac{J(J+1)-3M^2}{3(2J-1)(2J+3)}\Delta\alpha_v F^2 \qquad (5.1)$$

where α_v is the polarisability and $\Delta\alpha_v$ is the anisotropy of the polarisability in quantum state v. Higher order terms in F need not be considered, because the Stark field perturbed spectra showed a linear dependence on F^2. A linear least squares fit to the R(1) Stark shifts and splittings recorded at various electric field strengths resulted in a correlation coefficient, R, of 0.9996 (Figure 5.3).

The equation for the Stark transition is :

$$\begin{aligned} W_{vJ'M'}(F) - W_{0J''M''}(F) &= -\frac{1}{2}(\alpha_v - \alpha_0)F^2 - \left[\frac{J'(J'+1)-3M'^2}{3(2J'-1)(2J'+3)}\Delta\alpha_v \right. \\ &- \left. \frac{J''(J''+1)-3M''^2}{3(2J''-1)(2J''+3)}\Delta\alpha_0\right] F^2 \end{aligned} \qquad (5.2)$$

In order to determine a value for $(\alpha_v - \alpha_0)$ and $\Delta\alpha_v$, measured rotational line shifts and splittings were fit to Equation 5.2. The ground state (static) anisotropy ($\Delta\alpha_0$) was calculated from 17 measurements of the Stark split P(1) transition, which does not depend upon the excited state polarisability anisotropy. The ground state $\Delta\alpha$ was found to be 1.071±0.014 $\mathring{A}^3$. Table 5.1 lists the results for the excited ro-vibrational

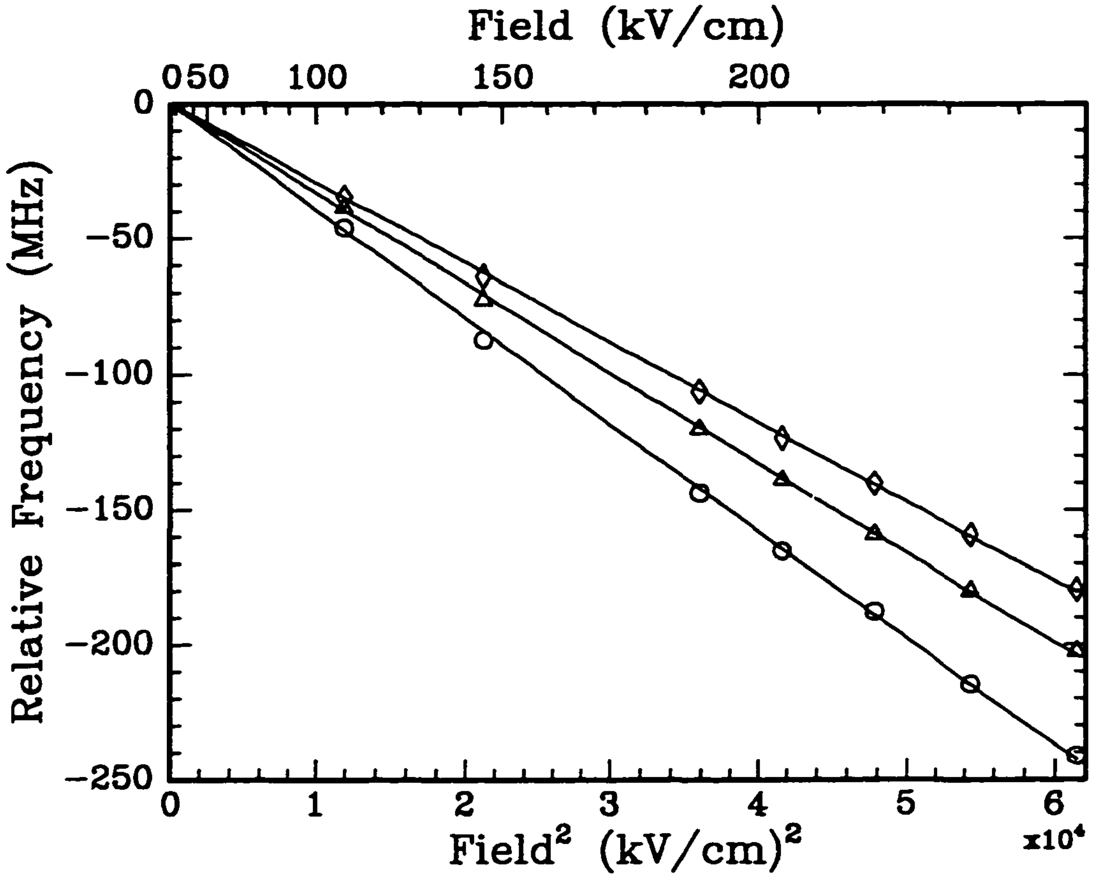

Figure 5.3: The result of the linear least-squares fit to the Stark field induced shifts and splittings of the R(1) ro-vibrational transition of $\nu_1 + 3\nu_3$. The zero frequency position marks the zero electric field position of the R(1) transition. The individual M transitions are identified as follows :

$$\begin{array}{lcl} \diamond\ M & = & 2 \leftarrow 1 \\ \triangle\ M & = & 1 \leftarrow 0 \\ \circ\ M & = & 0 \leftarrow \text{-}1 \end{array}$$

states, each an average of 5 or more measurements. Above J = 4, the individual *M* components of the Stark field perturbed spectrum could no longer be resolved and only spectral profiles could be fit.

Table 5.1: Experimental Results for the $|1030^00^0\rangle$ State of Acetylene

J	$(\alpha_v - \alpha_0)$	Å^3	$\Delta\alpha_v$	Å^3
0	-11.66	±0.03	Not	Available
1	22.49	±0.05	10.13	±0.04
2	3.92	±0.07	3.11	±0.06
3	1.881	±0.009	2.232	±0.024
4	1.260	±0.012	2.076	±0.012
5	1.209	±0.012	2.977	±0.013
6	0.499	±0.007	0.79	±0.010
8	0.488	±0.010	1.15	±0.03

5.4 Discussion

The results presented in Table 5.1 show a remarkable dependence on the rotational quantum number of the excited state. The normal mode description of the $|1030^00^0\rangle$ state places one quantum of excitation in the symmetric C-H stretch and 3 quanta in the asymmetric C-H stretch ($\nu_1 + 3\nu_3$). Local mode descriptions of the state place all four quanta in one or other of the C-H bonds, and then form symmetric and antisymmetric linear combinations of such excitations [11]. The antisymmetric combination, designated 04^-, corresponds to $|1030^00^0\rangle$ (*ungerade* symmetry) while the symmetric combination, designated 04^+, corresponds to $|0040^00^0\rangle$(*gerade* symmetry).

In what follows the dramatic J-dependence of the polarisability (see Table 5.1) is attributed to the Stark induced mixing of the 04^+ and 04^- states.

The 04^+ state may not be accessed by a direct transition from the ground state: however the 04^- to 04^+ transition is allowed and will provide a vibrational contribution to the static polarisability of the 04^- state. When J = M the applied field can only couple to the state of opposite parity with rotational quantum numbers J+1,M ($\Delta M = 0$) allowing an easier visualisation of the effects of the coupling (See Figure 5.4). With B ≈ 1.15177 cm^{-1} [47] and the difference in band origins, Θ, as 3.9 cm^{-1} [11], (04^-,J = 0) is 1.6 cm^{-1} higher in energy than (04^+,J = 1) and so is shifted higher in energy by the field corresponding to a negative polarisability. All other (04^-,J) levels are lower in energy than (04^+,J+1) and so have positive polarisabilities.

The Stark effect for two closely spaced energy levels has been described by Townes and Schawlow [30]. Briefly, for two states, ψ_1^0 and ψ_2^0, interacting in the presence of an electric field the new wavefunctions can be written as

$$\psi_\pm = a\psi_1^0 \pm b\psi_2^0 , \tag{5.3}$$

and the new energies (W), given by the secular equation

$$\begin{vmatrix} W_1^0 - W & W_{12} \\ W_{12} & W_2^0 - W \end{vmatrix} = 0 , \tag{5.4}$$

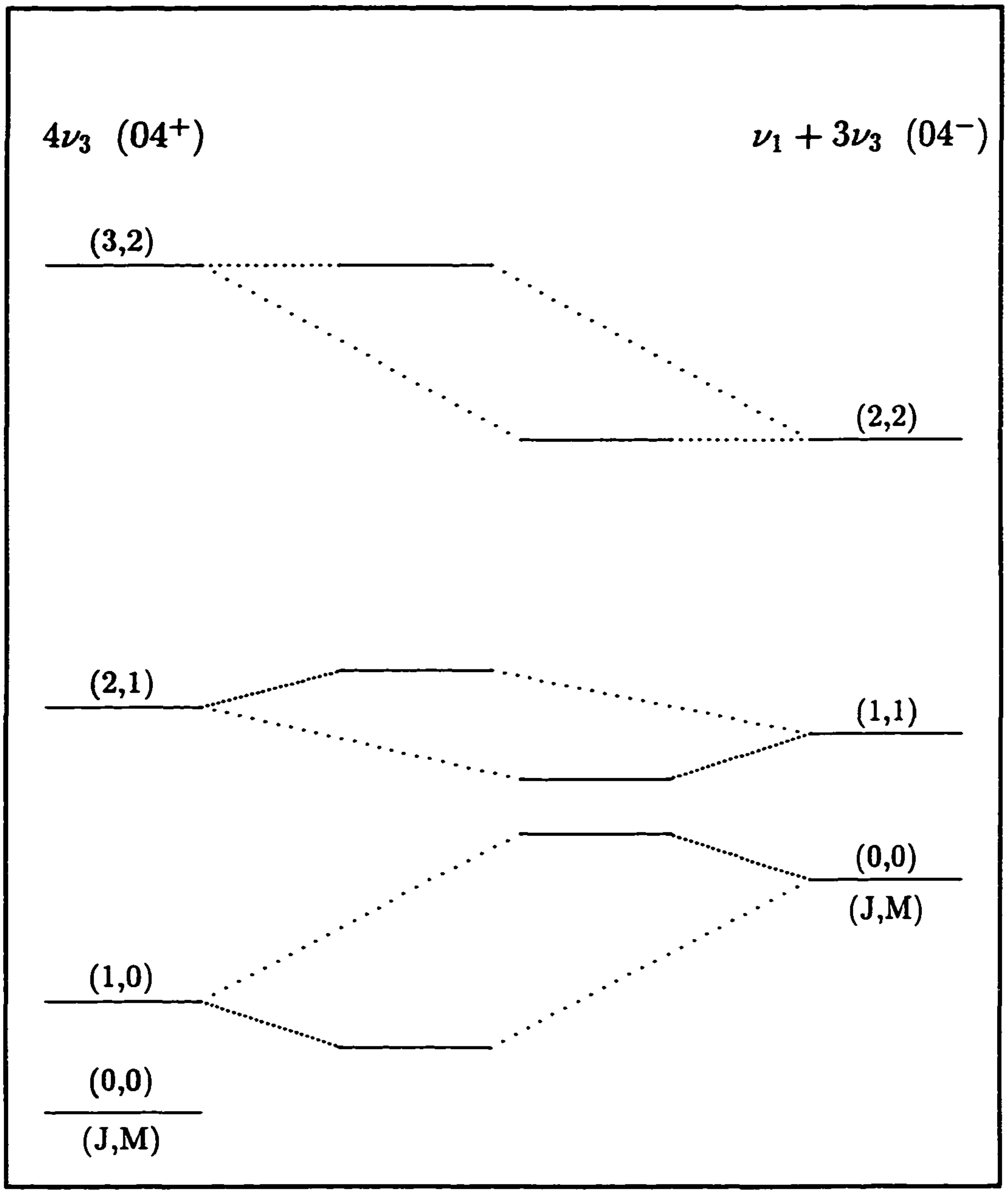

Figure 5.4: A simplified coupling scheme for the J = M energy levels of the 04^- and 04^+ vibrational states. The rotational constants were assumed to be equal and the difference in band origins was taken to be 3.9 cm^{-1} (see Reference [11]). The coupling strength was exaggerated somewhat to make the effect more noticeable

where $W_{12} = F^2\mu_{12}^2$, are

$$W = \frac{(W_1^0 + W_2^0)}{2} \pm \left[\left(\frac{W_1^0 - W_2^0}{2}\right)^2 + F^2\mu_{12}^2\right]^{1/2} . \tag{5.5}$$

If the interaction energy, $F\mu_{12}$, is less than $(W_1^0 - W_2^0/2)$, Equation 5.5 can be expanded to give

$$W_1 = W_1^0 + \frac{F^2\mu_{12}^2}{W_1^0 - W_2^0} + \cdots \quad \text{and} \quad W_2 = W_2^0 - \frac{F^2\mu_{12}^2}{W_1^0 - W_2^0} + \cdots \tag{5.6}$$

The first term in each expansion is the unperturbed energy of the state and the second term is the corrective shift that accounts for the coupling of the states. Following infrared selection rules, the J state of 04^- can only couple with the $J+1$ and $J-1$ states of 04^+. The correction to the energy of the $(04^-, J)$ state is the sum of the corrective shifts from the coupling to the $(04^+, J+1)$ and $(04^+, J-1)$ states and can be expressed as :

$$\varepsilon_J^{04^-} = W_{(04^+,J+1) \leftarrow (04^-,J)} + W_{(04^+,J-1) \leftarrow (04^-,J)} . \tag{5.7}$$

Substituting the appropriate corrective shifts from Equation 5.6 results in

$$\varepsilon_J^{04^-} = F^2 \left[\frac{\mu_{J+1\leftarrow J}^2}{W_J^{04^-} - W_{J+1}^{04^+}} + \frac{\mu_{J-1\leftarrow J}^2}{W_J^{04^-} - W_{J-1}^{04^+}}\right] . \tag{5.8}$$

$W_J^{04^-}$ and $W_{J\pm1}^{04^+}$ are the energies of the unperturbed states and $\mu_{J'\leftarrow J''}$ is the J dependent transition dipole moment connecting the two states. The latter is given by [30]

$$|\mu_{J+1\leftarrow J}|^2 = \mu^2\frac{(J+1)^2 - M^2}{(2J+1)(2J+3)} \text{ and } |\mu_{J-1\leftarrow J}|^2 = \mu^2\frac{J^2 - M^2}{(2J+1)(2J-1)}. \tag{5.9}$$

The energy, $\varepsilon_J^{04^-}$, can also be supplied by Equation 5.1. Combining Equations 5.1, 5.8 and 5.9 produces Equation 5.10:

$$\begin{aligned} \frac{1}{2}\alpha_v &+ \frac{J(J+1) - 3M^2}{3(2J-1)(2J+3)}\Delta\alpha_v \\ &= -\mu^2\left[\frac{(J+1)^2 - M^2}{(\Theta - 2B(J+1))(2J+1)(2J+3)} + \frac{J^2 - M^2}{(\Theta + 2BJ)(2J-1)(2J+1)}\right]. \end{aligned} \tag{5.10}$$

In order to fit the measured data to Equation 5.10, a value for the ground state polarisability must be assumed. Meath and Kumar have calculated a value of 3.40 Å^3 for the electronic contribution to the static polarisability based upon dipole oscillator strength distributions and available experimental dipole oscillator strength and molar refractivity data [88], the results of which are in complete agreement with experimental data [89–91]. To make use of this value in the present calculations it must be corrected for the vibrational contribution to the polarisability. For a linear molecule in internal state $v = 0$, the parallel and perpendicular vibrational contributions to the ground state polarisability tensor can be written as [38]

$$\alpha_{0\parallel}^{\mathrm{vib}} = \frac{2}{hc}\sum_{v\neq 0}\omega_{v0}^{-1} \mid \langle v|\mu_z|0\rangle \mid^2$$

$$\alpha^{\mathrm{vib}}_{0\perp} = \frac{2}{hc}\sum_{v\neq 0}\omega_{v0}^{-1} \mid \langle v|\mu_x|0\rangle \mid^2 \tag{5.11}$$

where ω_{v0} is the frequency (in cm^{-1}) for the transition $v \leftarrow 0$ and μ_z/μ_x are the parallel/perpendicular components of the electric dipole operator relative to the molecular symmetry axis. The matrix element $\langle v|\mu_i|0\rangle$ ($i = x$ or z) can be evaluated from measured band strengths by the relationship ([92]) :

$$\mathrm{S}_0^v = \frac{8\pi^3}{3hc}\frac{e^{\frac{-E_0}{kT}}(1 - e^{\frac{-\omega_{v0}}{kT}})}{\mathrm{Q}_{\mathrm{vib}}} g_v\omega_{v0} \mid \langle v|\mu_i|0\rangle \mid^2 \tag{5.12}$$

where $\mathrm{Q}_{\mathrm{vib}}$ is the vibrational partition function, g_v is the degeneracy of state v, E_0 is the ground state energy (cm^{-1}) and S_0^v has units of cm·molecule^{-1}. Combining equations (5.11) and (5.12) yields

$$\alpha^{\mathrm{vib}}_{0(\|\mathrm{or}\perp)} = \frac{3}{4\pi^3}\sum_{v\neq 0}\frac{\mathrm{Q}_{\mathrm{vib}}\ \mathrm{S}_0^v}{e^{\frac{-E_0}{kT}}(1 - e^{\frac{-\omega_{v0}}{kT}})\omega_{v0}^2\, g_v} \tag{5.13}$$

and the component of α_0^{vib} is determined by the symmetry of the infrared absorption band. Using the currently measured band strengths this analysis produces values of 0.56 $\mathring{A}^3$ and -0.72 $\mathring{A}^3$ for α_0^{vib} and $\Delta\alpha_0^{\mathrm{vib}}$, respectively. Previous analyses only included the ν_3 transition when calculating $\alpha_{0\|}^{\mathrm{vib}}$ [93]: the present measurements show that the contribution from $\nu_4 + \nu_5$ is approximately 2.2 times larger than that from ν_3. Usually fundamental vibrational transitions provide the dominant contribution to α_v. However, as may be seen in the results section, ν_3 is not a strong transition ;

furthermore, it is three times higher in energy than $\nu_4 + \nu_5$. Therefore, in this particular case a combination band and a fundamental make a comparable contribution. Despite the inclusion of $\nu_4 + \nu_5$, the major contribution to the revised estimates of α_0^{vib} and $\Delta\alpha_0^{\mathrm{vib}}$ is the improved value for the strength of the ν_5 transition. The ground state static polarisability can now be set at 3.96 $\AA^3$ and a fit to Equation 5.10 gives $\alpha_{04^-} = 4.62\pm0.09$ $\AA^3$, $\mu = 0.0696\pm0.0012$ Debye and $\Theta = 4.133\pm0.016$ cm^{-1}. The latter value is in good agreement with the local mode analysis of the acetylene vibrational modes, which predicts a band origin difference of 3.9 cm^{-1} [11]. Figure 5.5 depicts a fit of Equation 5.10 to the data for the special case $J = M$.

The present measurement of the ground state static polarisability anisotropy of acetylene ($\Delta\alpha_0 = 1.071$ $\AA^3$) differs from measurements based upon Rayleigh scattering (1.74 $\AA^3$ [40] and 1.653 $\AA^3$ [41]) and those based, in part, upon the Kerr effect (1.32 ± 0.29 $\AA^3$) [93]. Although the Kerr effect measures the static polarisability, due to experimental limitations, the measurements of acetylene were not comprehensive and the value determined for $\Delta\alpha_0$ is not necessarily reliable. The Rayleigh scattering measurements made in the visible region of the spectrum were extrapolated to produce the "zero frequency" anisotropy of the polarisability. Adjusting for the vibrational contribution calculated earlier brings the Rayleigh scattering values to 1.02 $\AA^3$ [40] and 0.933 $\AA^3$ [41], of which the former is in good agreement with the present measurements.

It is of interest to note that, although the vibrational transition dipole moment

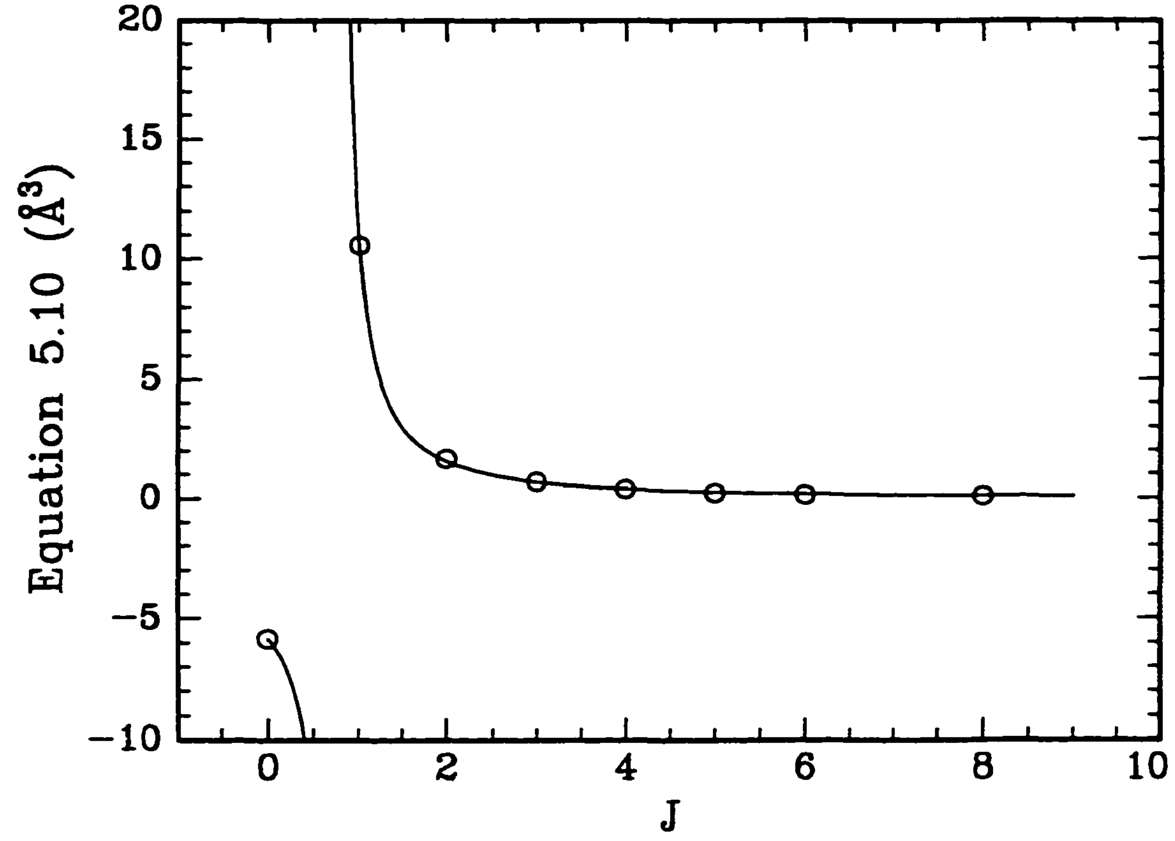

Figure 5.5: The result of the non-linear least-squares fit of Equation 5.10 to the experimental data for the J = M levels only. The o represent the left-hand-side of Equation 5.10 calculated from the experimental values obtained for $\alpha_{v\,J}$ and $\Delta\alpha_{v\,J}$. The smooth curve describes the fit of the right-hand-side of Equation 5.10 to the experimental data.

connecting 04^+ and 04^- is along the symmetry axis ($\Sigma - \Sigma$ transition), both components of the polarisability tensor are enhanced by the coupling. Figure 5.6 depicts the parallel ($\alpha_{\parallel}$) and perpendicular ($\alpha_{\perp}$) components of the polarisability tensor as a function of J. The parallel component (stars) is slightly more enhanced than the perpendicular component (solid circles). The reason for the increase in both components is unclear. Also, it is interesting to see that at $J = 5$ the parallel component appears to have received an additional increase over the perpendicular component. This unexpected increase in $\Delta\alpha$ manifested itself as an increase in the splitting of the Stark field perturbed spectrum of R(4). It is speculated that another, weaker, interaction with a different state (not 04^+) may be responsible for this.

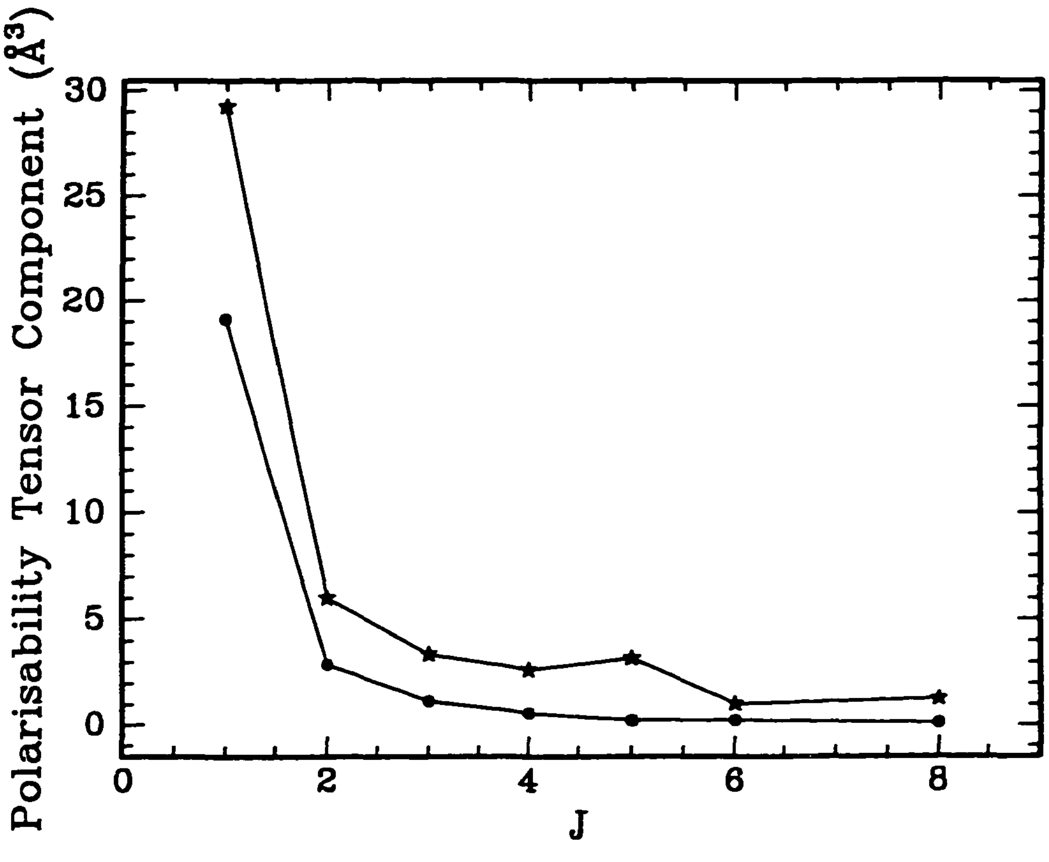

Figure 5.6: The components of the polarisability tensor are plotted here as a function of J. The solid circles depict the perpendicular components ($\alpha_\perp$) and the stars are the parallel components ($\alpha_\parallel$). Notice that both components of the polarisability tensor are enhanced despite the fact that the transition dipole moment connecting the two vibrational states lies along the molecular symmetry axis. The $J = 0$ data point could not be calculated since a measured value of the polarisability anisotropy is not available for $J = 0$.

Chapter 6

Acetylene $\nu_2 + 3\nu_3$

6.1 Introduction

Some of the earliest literature on the $\nu_2 + 3\nu_3$ band of acetylene described "disturbances" in the spectra and "extra lines" [94]. More recent studies have shown there to be 14 vibrational bands within the 11500–11900 cm^{-1} range, all of which have exhibited extensive perturbations [78]. These bands were analysed by assuming they interacted via Fermi, Coriolis and ℓ-type resonances [80]. As a result, six of the 14 were identified. Milce and Orr have conducted infrared–ultraviolet (IR-UV) double resonance experiments that indicated the $|0130^00^0\rangle$ state ($\nu_2+3\nu_3$ band) was strongly coupled with a, tentatively labelled, $|0130^00^0\rangle_{\text{II}}$ state ($[\nu_2+3\nu_3]_{\text{II}}$ band) [95, 96]. They noted that the J = 5 level of $|0130^00^0\rangle$ was unusually "UV-bright". This was unexpected, since the first electronic state ($\tilde{A}$) of acetylene has a *trans*-bent geometry [27], favouring transitions from the ground electronic state that have the *trans*-bending vibration (ν_4) excited. In order to observe the UV spectra originating from the $|0130^00^0\rangle$ state, some mixing with a state containing several quanta of the *trans*-bending vibration must be occurring [95]. Crim *et al.* have reported similar observations for 2, 3 and 4 quanta ν_{CH} (C–H) stretching vibrations in a series of experiments on acetylene [97–100].

Field *et al.* have conducted stimulated emission pumping experiments that probe the vibrational overtone region of acetylene from 5000–18000 cm^{-1} [84, 101]. Their results indicate a much more restrictive view of intramolecular vibrational redistribution in highly excited acetylene than was previously thought [102]. The almost complete absence of C-H stretching excitation in the $\tilde{A} \rightarrow \tilde{X}$ seemed to indicate a restrictive coupling of the initial C≡C stretch/*trans*-bending excitation to the other vibrational degrees of freedom. The ensuing analysis determined that a Darling-Dennison resonance was required to transfer energy to the *cis*-bending vibration (ν_5) before the energy can be transferred to the other vibrational modes. However, this latter energy flow seemed to be further restricted in that a C≡C stretching excitation was also required, resulting in a far more organised picture of energy flow than was originally expected.

The acetylene C≡C (ν_2) stretching vibration is not included in local mode calculations and therefore some type of hybrid notation needs to be used to describe the $|0130^00^0\rangle$ state (*ungerade* symmetry) using local mode terminology. The C–H stretching portion of the $|0130^00^0\rangle$ state is written as 03^- in local mode notation and its corresponding *gerade* state is 03^+ (normal mode $|1120^00^0\rangle$) [11]. A hybrid local mode notation of $1|03^-$ will therefore be used to describe the $|0130^00^0\rangle$ state. The 03^- state was calculated to be 17.1 cm^{-1} higher in energy than the 03^+ state [11] and it is assumed that this will also be true for the $1|03^-$ and $1|03^+$ states.

What follows will not only test the local mode calculations of Child and Halonen [11], but, hopefully, also be a probe of the mysterious, strongly perturbing, $|0130^00^0\rangle_{\text{II}}$ state.

6.2 Experimental Details

Generally, the experimental conditions were identical to those for the measurement of the $\nu_1 + 3\nu_3$ band of acetylene. The main difference here lay in the fact that the ro-vibrational transitions of the $\nu_2 + 3\nu_3$ band (11600.07 cm^{-1}) were approximately five times weaker than those of the $\nu_1 + 3\nu_3$ band, requiring the use of the BUC. Measurements were made on the R(0) to R(7) ro-vibrational transitions, by using the laser power build-up cavity (BUC) and tables of previously measured transition frequencies [94, 103].

The BUC Stark cell could not be as well insulated as the regular Stark cell due to the close proximity of all the components within the aluminum BUC housing. Typically fields of no more than 183 kV/cm were generated with the BUC Stark electrodes. The BUC Stark gap was measured to be 0.8187 mm by calibration against the hydrogen fluoride $v = 0$ electric dipole moment [68].

In the case of $\nu_2+3\nu_3$, the Stark shift of the transitions was not usually sufficient to allow the measurement of the unperturbed and the Stark split ro-vibrational spectrum during the same laser scan. The spectra were often measured twice. One spectrum was usually taken while turning the electric field off during the scan to locate the zero electric field position, at the expense of part of the Stark split spectrum. The scan would then be repeated with the electric field left on. During the analysis the two spectra were overlayed to locate the zero electric field position in the complete Stark field perturbed spectrum.

6.3 Results

The analysis of the spectra for the Stark split ro-vibrational transitions of the $\nu_2+3\nu_3$ band was not as straight forward as that for the $\nu_1 + 3\nu_3$ band. Figure 6.1 depicts the Stark field perturbed spectra of the R(0) to R(7) ro-vibrational transitions at an electric field of 171.0 kV/cm. The Stark split spectrum of the R(0) transition consists of two peaks instead of just the one expected for $\Delta M = \pm 1$ selection rules. The laser electric field polarisation was rotated slightly away from 90° with respect to the Stark field to allow the observation of two Stark transitions ($M = 0 \leftarrow 0$ and $1 \leftarrow 0$) and, hence, the measurement of the excited state polarisability anisotropy.

As can be seen in Figure 6.1 not only did the polarisability change sign at R(5), but the coefficient for the splitting of the transition for R(4) seems to be an order of magnitude greater than the rest. In fact, at this particular field, the spectra of R(3), R(4), and R(5) cannot be fit to the Stark equation for a non-polar molecule (Equation 5.2). As a result, the Stark electric field dependence of each of the rovibrational transitions was examined in detail. Only spectra from R(3), R(4) and R(5) could not be fit to the second order Stark equation at all fields. The polarisability data extracted from the R(0), R(1), R(2), R(6) and R(7) Stark field perturbed spectra are given in Table 6.1.

In order to provide a better picture of what the expected pattern for a Stark split spectrum is, the peak positions of the Stark split spectra of R(2) (Figure 6.2A) and R(3) (Figure 6.2B) are plotted as a function of electric field. The R(2) Stark field perturbed spectrum follows the F^2 dependence predicted by Equation 5.2. The R(3) spectrum not only has peaks that tune more rapidly than F^2, some of these peaks seem to originate from outside the R(3) Stark split manifold. However, at lower electric fields, the Stark split spectra for R(3) (72.0 kV/cm) and R(5) (107.9 kV/cm) followed the second order Stark effect and were fit to Equation 5.2. The polarisability data for R(3) and R(5) were obtained at these lower fields and are also listed in Table 6.1. Hence, peaks that tune according to the second order Stark equation will be called *normal* and peaks that tune much more rapidly will be called *rogue*.

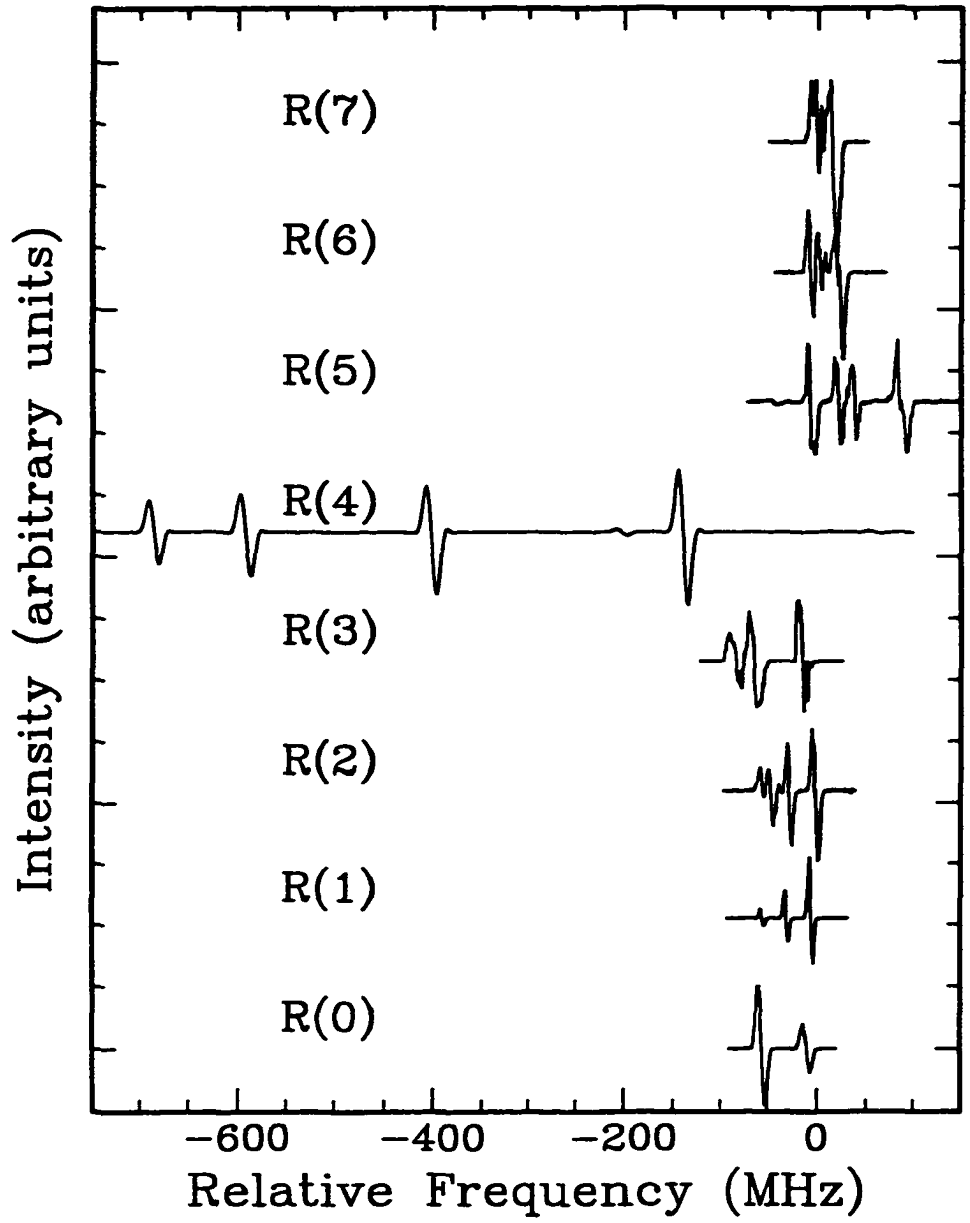

Figure 6.1: The Stark split spectra of the R(0–7) rovibrational transitions of the $\nu_2 + 3\nu_3$ band at an electric field of 171.0 kV/cm. Each spectrum was adjusted so the zero electric field transition would appear at zero frequency. All spectra follow $\Delta M = \pm 1$ selection rules except for R(0), in which case the $\Delta M = 0$ transition was also measured. The intensities were normalised to the largest peak in each spectrum for comparison purposes.

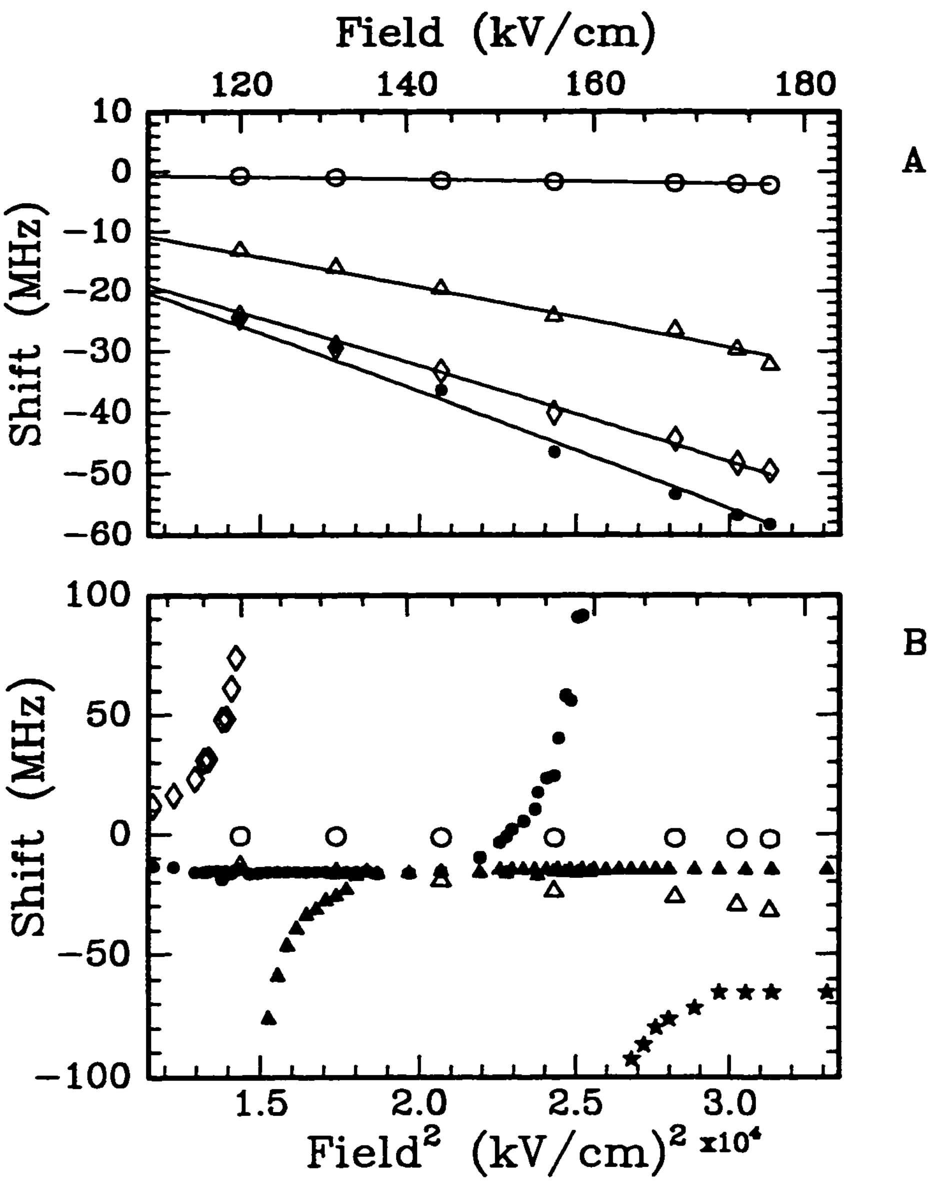

Figure 6.2: The R(2) (A) and the R(3) (B) Stark split spectra are depicted here. Spectrum A was fit to Equation 5.2 and the transitions were identified as $M = 3 \leftarrow 2 \equiv \bigcirc$, $M = 2 \leftarrow 1 \equiv \triangle$, $M = 1 \leftarrow 0 \equiv \diamond$, and $M = 0 \leftarrow -1$ and $M = -1 \leftarrow -2$ are $\bullet$. At these fields the R(3) spectrum (B) could not be fit to the second order Stark equation and the transitions were not readily identified.

Table 6.1: Polarisability data determined by fitting the spectra to the second order Stark equation (Equation 5.2). The results for $J = 8$ have no units of error associated with them, but the values for the difference in polarisabilities and the anisotropy were obtained from an averaged spectrum (N/A ≡ Not Available).

J	$(\alpha_v - \alpha_0)$	$\mathring{A}^3$	$\Delta\alpha_v$	$\mathring{A}^3$
0	1.04	±0.07	N/A	
1	1.00	±0.09	4.63	±0.06
2	1.177	±0.008	5.065	±0.029
3	1.27	±0.06	6.283	±0.024
4	1.9	±0.1	11.0	±0.5
5	N/A		N/A	
6	-1.99	±0.06	-7.08	±0.14
7	-0.49	±0.05	-1.76	±0.11
8	-0.320	N/A	-1.05	N/A

6.3.1 The R(3) Ro-vibrational Transition

The spectrum of R(3) (11609.014 cm^{-1}) was among the first examined and it was noticed that as the field was increased, a new peak, not belonging to the expected pattern, emerged at a lower frequency relative to the zero electric field position of the R(3) transition (Figures 6.3 to 6.7). This new, *rogue*, peak rapidly moved closer to the field free position as the field was increased, while at the same time a *normal* peak within the R(3) Stark split manifold moved to higher frequency. As the *rogue* peak came closer it gained intensity and it slowed its tuning rate, while at the same time the *normal* peak lost intensity and increased its tuning rate. Hence, the normal peak accumulated enough *rogue* character to now be called *rogue* and vice versa. The signals for the *rogue* and *normal* peaks were as needed amplified by increasing the sensitivity of the lock-in amplifier. This can be seen by a sudden increase in baseline noise or by a small spike in the spectrum. Upon increasing the electric field further, a second *rogue* peak emerged and another *normal* peak disappeared to the blue side of the spectrum. Table 6.2 lists the positions of the "paired" *normal* and *rogue* peaks and a visual illustration of these data is given in Figure 6.8 on page 108.

In order to identify the peaks in the *normal* part of the R(3) Stark field perturbed spectrum, the relative intensities of the individual peaks was compared. According to [30]

$$I_{M' \leftarrow M''} = (J' + M' - 1)(J' + M')(\Delta J = \pm 1) \tag{6.1}$$

the intensity ratios for the peaks should be 28:21:15:10:6:3:1 for the seven (2J+1) peaks of the ΔM= ±1 Stark field perturbed spectrum. However, not all the peaks were resolved, therefore the identities were confirmed by comparison with a calculated spectrum. At lower fields, where there was no perturbation due to the presence of *rogue* peaks, the experimental spectrum compared well with the calculated one and the transitions were easily labelled. Hence, the two most intense peaks (calculated intensity ratio 28:21 = 1.33, measured intensity ratio = 1.34) represent the $M = 4 \leftarrow 3$ and $M = 3 \leftarrow 2$ transitions, respectively. The correlation seen in Figure 6.8 suggests that both the *rogue* and *normal* peaks belong to the same M_J type of transition and, therefore, the *rogue* peak has been given the same M_J transition label.

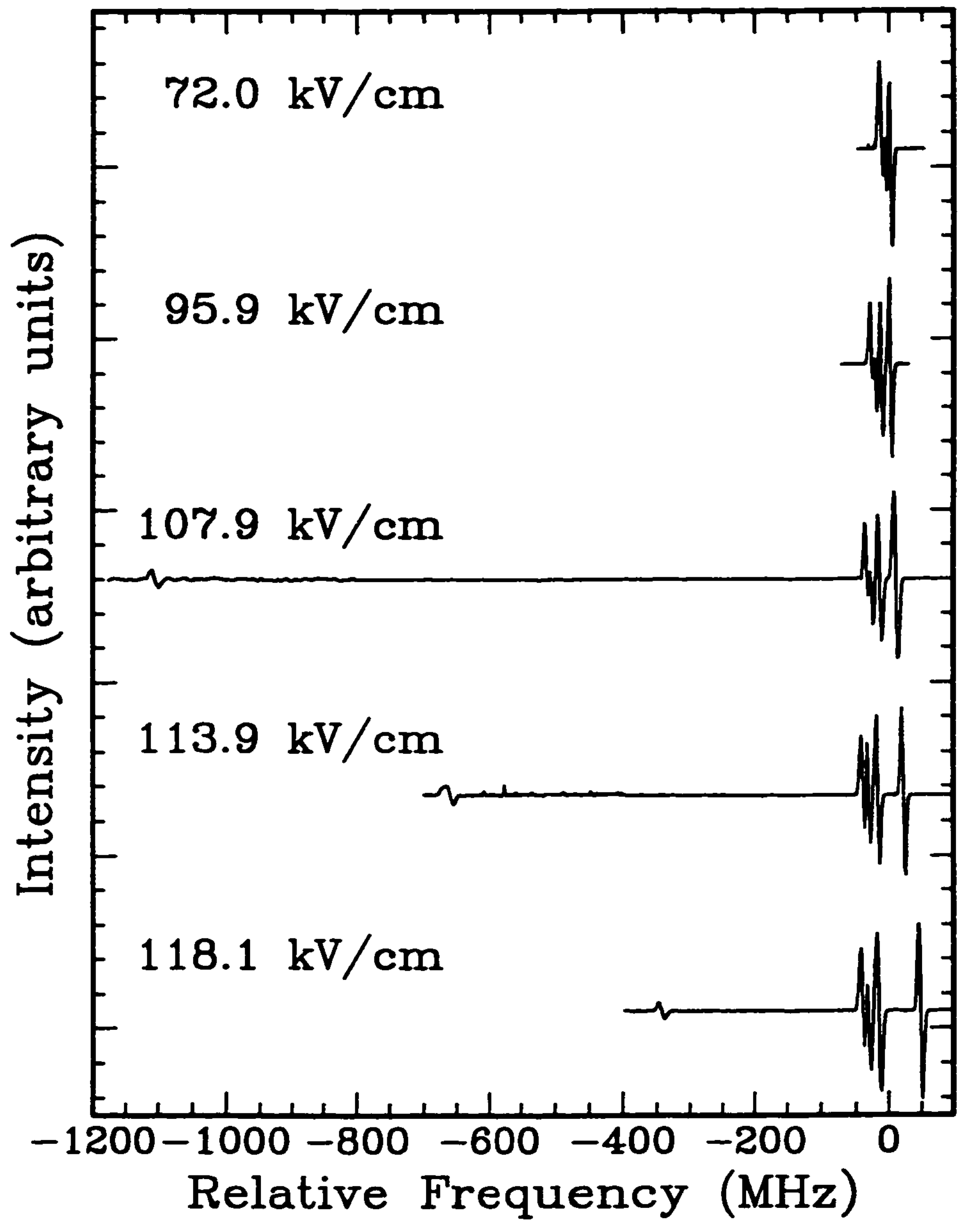

Figure 6.3: Electric Field dependence of the Stark split spectrum of $\nu_2 + 3\nu_3$ R(3). The zero in the spectra is the field free position of R(3). At 107.9 kV/cm a new, *rogue*, peak emerged. In order to make this peak more visible, the intensity in that portion of the spectrum was amplified by a factor of two to five, depending on the existing signal-to-noise ratio. Only 25 of the 60 spectra measured are depicted in this series ending with Figure 6.7.

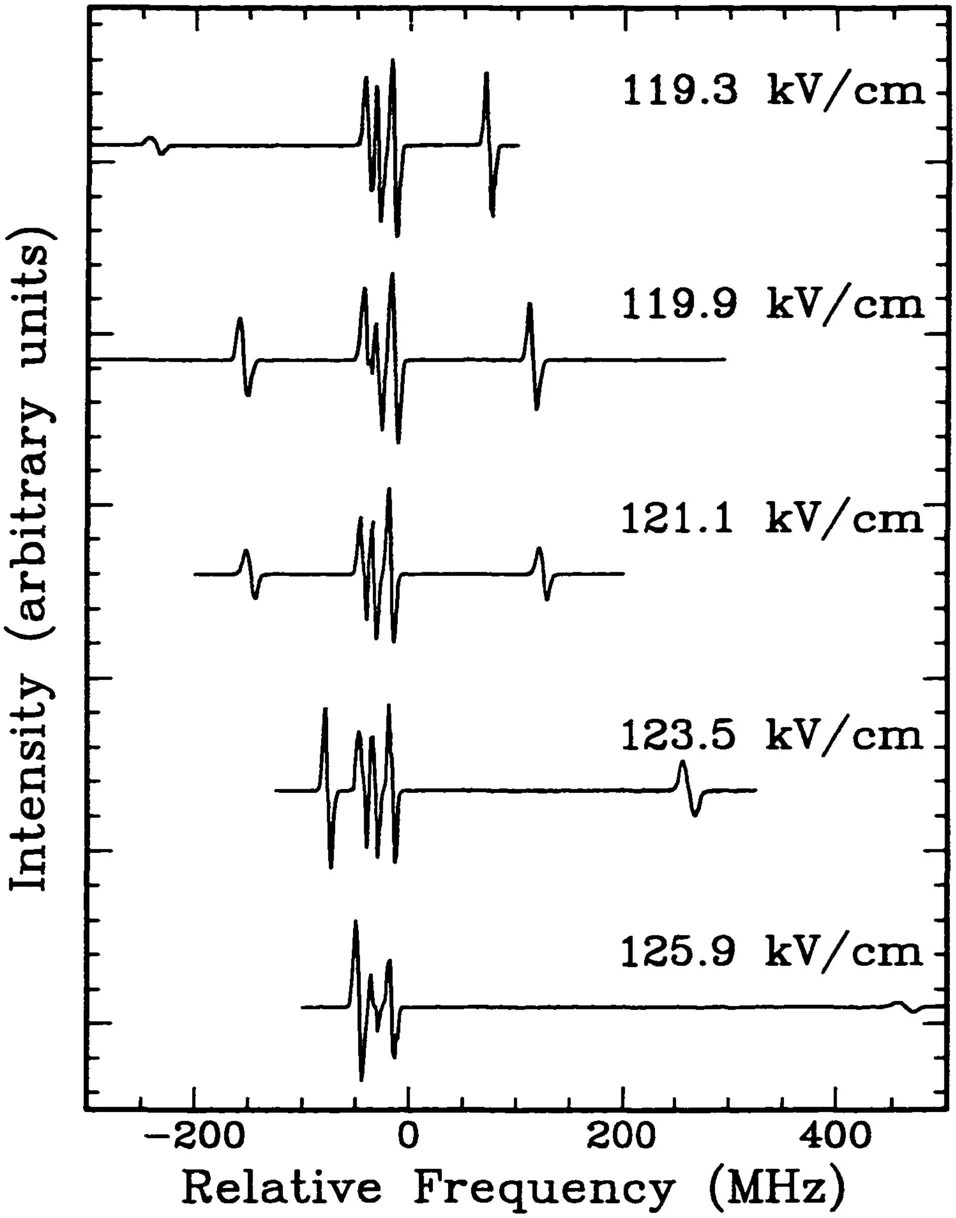

Figure 6.4: Electric Field dependence of Stark split spectrum of $\nu_2 + 3\nu_3$ R(3). The zero in the spectra is the field free position of R(3). At about 121.1 kV/cm the *rogue* and *normal* peaks appear to be equal in intensity.

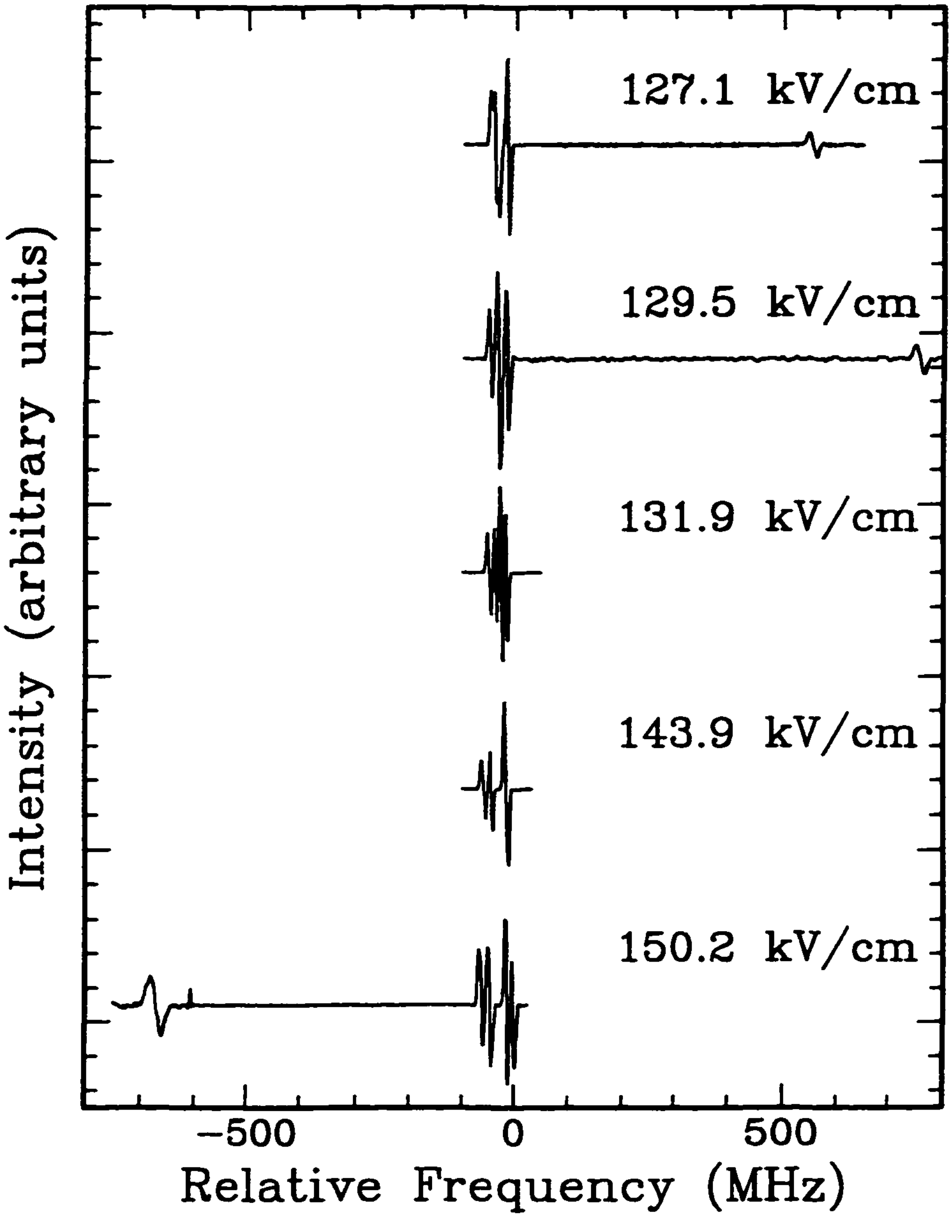

Figure 6.5: Electric Field dependence of Stark split spectrum of $\nu_2 + 3\nu_3$ R(3). The zero in the spectra is the field free position of R(3). The second *rogue* peak first appears at 150.2 kV/cm.

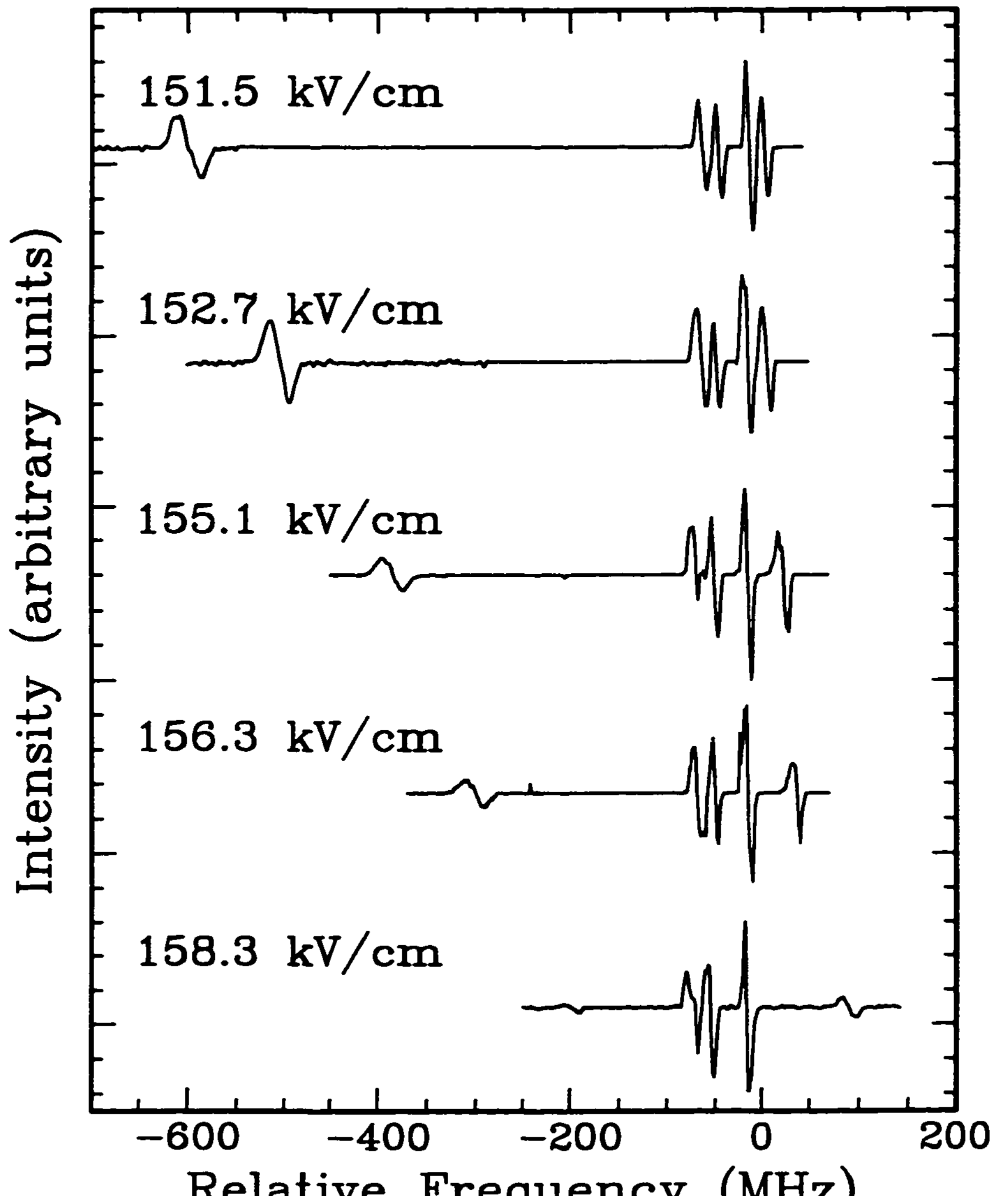

Figure 6.6: Electric Field dependence of Stark split spectrum of $\nu_2 + 3\nu_3$ R(3). The zero in the spectra is the field free position of R(3).

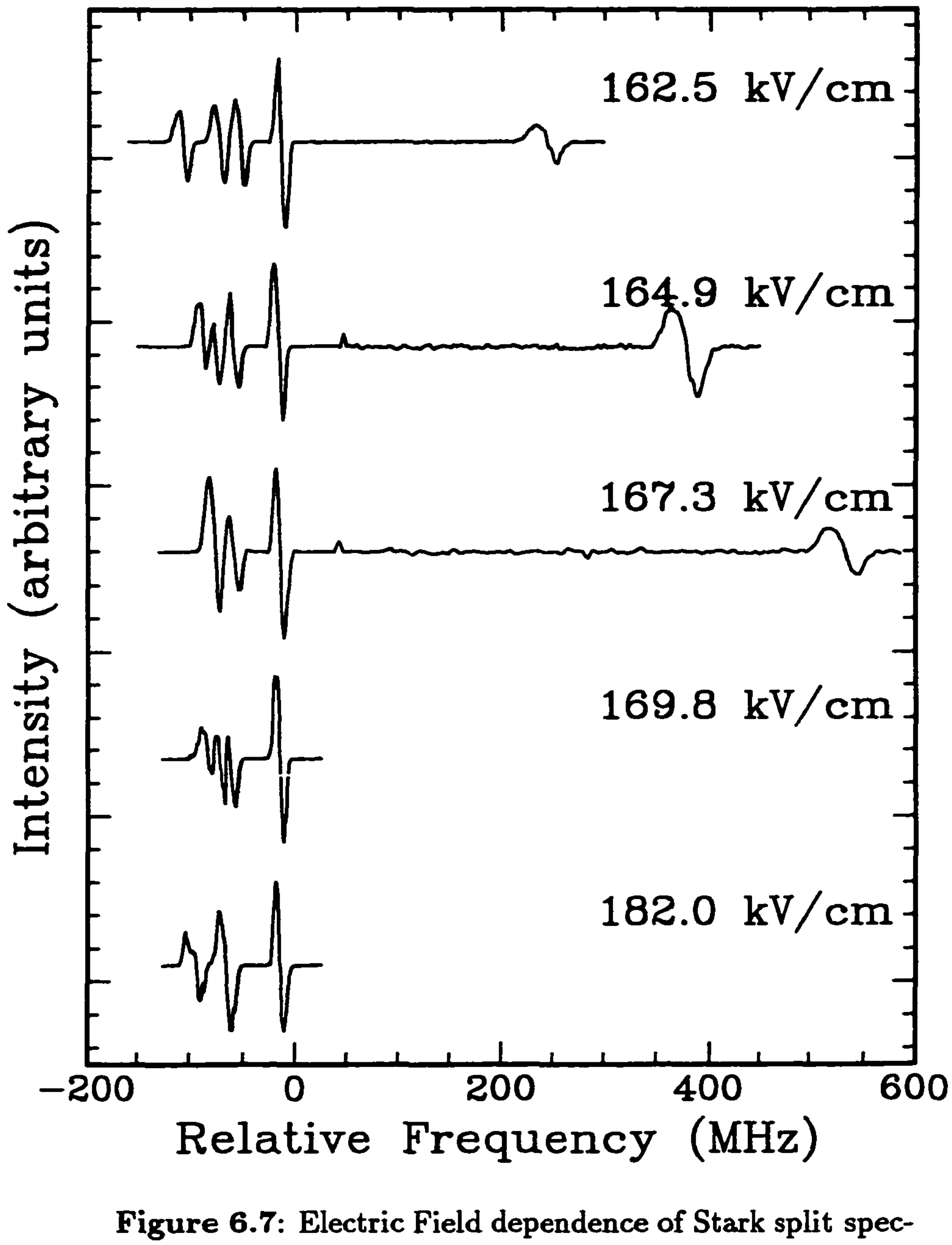

Figure 6.7: Electric Field dependence of Stark split spectrum of $\nu_2 + 3\nu_3$ R(3). The zero in the spectra is the field free position of R(3).

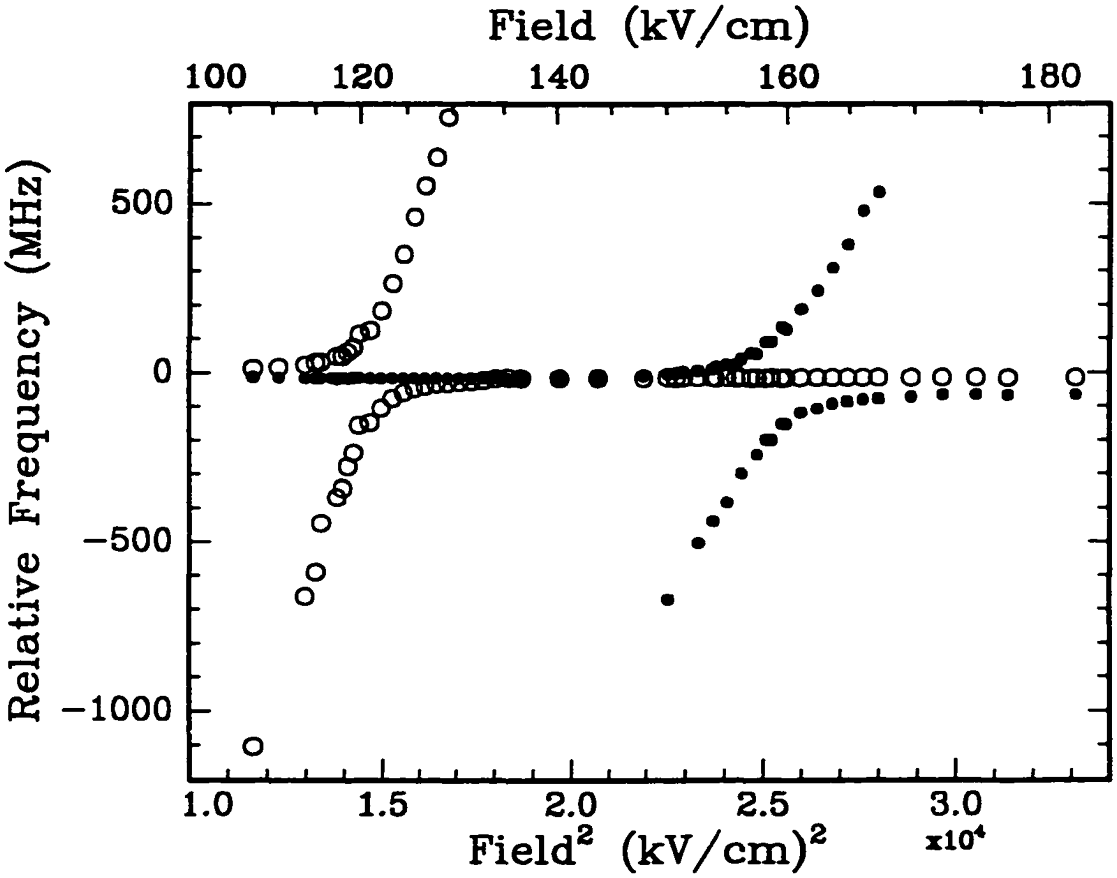

Figure 6.8: Electric Field dependence of the *normal* and *rogue* peaks in the $\nu_2+3\nu_3$ R(3) Stark field perturbed spectrum. Zero frequency is the field free position of R(3). The open circles represent the first *normal-rogue* pair and the solid circles the second pair. The peak positions plotted here are listed in Table 6.2.

Table 6.2: Field Dependent *rogue* and *normal* Line Positions for R(3)

Electric Field (kV/cm)	$M = 4 \leftarrow 3$		$M = 3 \leftarrow 2$	Electric Field (kV/cm)	$M = 4 \leftarrow 3$	$M = 3 \leftarrow 2$	
	normal (MHz)	*rogue* (MHz)	*normal* (MHz)		*rogue* (MHz)	*normal* (MHz)	*rogue* (MHz)
107.9	11.8	-1104.7	-13.3	150.2	-15.0	-3.5	-670.9
110.9	16.3		-13.8	150.9	-16.6	-1.1	
113.9	23.1	-661.6	-16.0	151.5	-15.0	2.0	
115.1	30.9	-590.4	-16.0	152.7	-15.1	5.3	-503.5
115.7	31.3	-445.2	-15.5	153.9	-15.1	10.3	-439.3
117.5	47.9	-369.6	-18.7	154.2	-17.4	17.4	
118.1	48.5	-342.6	-15.5	155.1	-15.0	23.3	-383.9
118.7	60.9	-278.7	-16.3	155.9	-16.0	24.4	
119.3	73.7	-237.8	-15.0	156.3	-14.8	40.0	-300.0
119.9	114.6	-155.2	-14.5	157.1	-16.1	57.8	
121.1	124.8	-147.5	-16.6	157.6	-15.0	55.8	-243.2
122.3	182.4	-105.1	-16.3	158.3	-16.4	90.5	-198.6
123.5	263.5	-76.3	-16.0	158.8	-15.0	91.3	-199.7
124.7	350.0	-58.9	-16.0	159.6	-16.2	135.0	-151.5
125.9	461.9	-46.7	-16.0	160.0	-15.0	127.6	-152.3
127.1	553.5	-39.6	-16.0	161.2	-15.4	187.8	-118.4
128.3	638.3	-33.6	-16.0	162.5	-15.0	242.4	-107.0
129.5	758.5	-31.7	-16.0	163.7	-15.0	309.4	-92.9
130.7		-27.9	-16.0	164.9	-15.0	378.3	-87.0
131.9		-26.0	-16.0	166.1	-15.0	480.1	-80.0
133.1		-23.3	-16.0	167.3	-15.0	533.5	-76.5
134.3		-17.5	-16.0	169.8	-15.0		-72.0
135.5		-15.7	-15.7	172.2	-15.0		-65.6
136.7		-16.6	-16.6	174.7	-15.0		-65.6
140.3		-16.4	-16.4	177.1	-15.0		-65.6
143.9		-16.0	-16.0	182.0	-15.0		-65.6
148.1		-16.4	-9.9				

6.3.2 The R(4) Ro-vibrational Transition

The Stark field perturbed spectra of R(4) (11611.138 cm^{-1}) were perhaps the most interesting. In the absence of an electric field there were two peaks in the spectrum (top of Figure 6.9). The more intense of the two peaks was the field free $\nu_2 + 3\nu_3$ R(4) transition at 11611.138 cm^{-1}; the ± 0.01 cm^{-1} accuracy of the wavemeter was sufficient to ascertain this. The second, *rogue*, peak was found -469 MHz (-0.0156 cm^{-1}) relative to the *normal* peak and was 2.89 times less intense. As the Stark field was increased, the *rogue* peak split much more rapidly than the *normal* peak and when the maximum attainable field was reached, only three of the *rogue* peaks were still observable (See Figures 6.9 to 6.11). The field dependent positions of each peak are listed in Tables 6.3 and 6.4. The peak numbers in the columns bear no relation to one another and are provided for reference purposes only.

Figure 6.12 illustrates the considerable difference in tuning rates of the *normal* and *rogue* peaks. In comparison to the other Stark split ro-vibrational transitions of $\nu_2 + 3\nu_3$, the *normal* R(4) peaks have anomalously large tuning rates; yet the tuning rates of the *rogue* peaks are larger still. Another interesting point that can be seen in Figure 6.12 is the fact that some of the peaks within the *normal* Stark split manifold cross as the Stark field is increased. Specifically, the peaks marked with the ○ and ● cross at approximately 85 kV/cm and the ⋆ peak crosses both the △ (80 kV/cm) and the ◇ (115 kV/cm) peaks. This type of behaviour cannot be reproduced with the second order Stark effect. Neither the *rogue* nor the *normal* Stark split R(4) spectrum could be fit to the second order Stark equation (Equation 5.2) at any of the applied electric fields.

The spectrum of each type of transition (*rogue* and *normal*) split into a total of six peaks each, even though each has nine ($2J + 1$) allowed transitions. A computed Stark split spectrum for a typical R(4) transition reveals that the three weakest of the Stark transitions are overlapped with three other, more intense, peaks (Figure 6.13). Due to the finite line width of the molecular beam laser system (5-6 MHz), only six peaks are observed.

6.3.3 The R(5) Ro-vibrational Transition

The R(5) (11613.223 cm^{-1}) series of spectra (Figures 6.14 to 6.17) showed results similar to those of the R(3) series. However, for R(5), there were four *rogue* peaks that emerged on the blue side of the spectrum and, accordingly, four *normal* peaks shifted out to the red side of the spectrum. Figure 6.18 depicts the positions of the *normal* and *rogue* peaks as a function of the square of the electric field, and, once again, the correlation between them. In the case of R(5) the rapidly tuning peaks seem to belong to lower intensity components of the Stark split manifold, rather than the higher intensity ones as was the case for R(3). Just as with R(3), a calculated spectrum was used to identify the M transitions at fields low enough to avoid the complication introduced by the *rogue* peaks. The spectrum at 183.2 kV/cm (page 123) shows the third most intense peak retreating from another incoming *rogue*

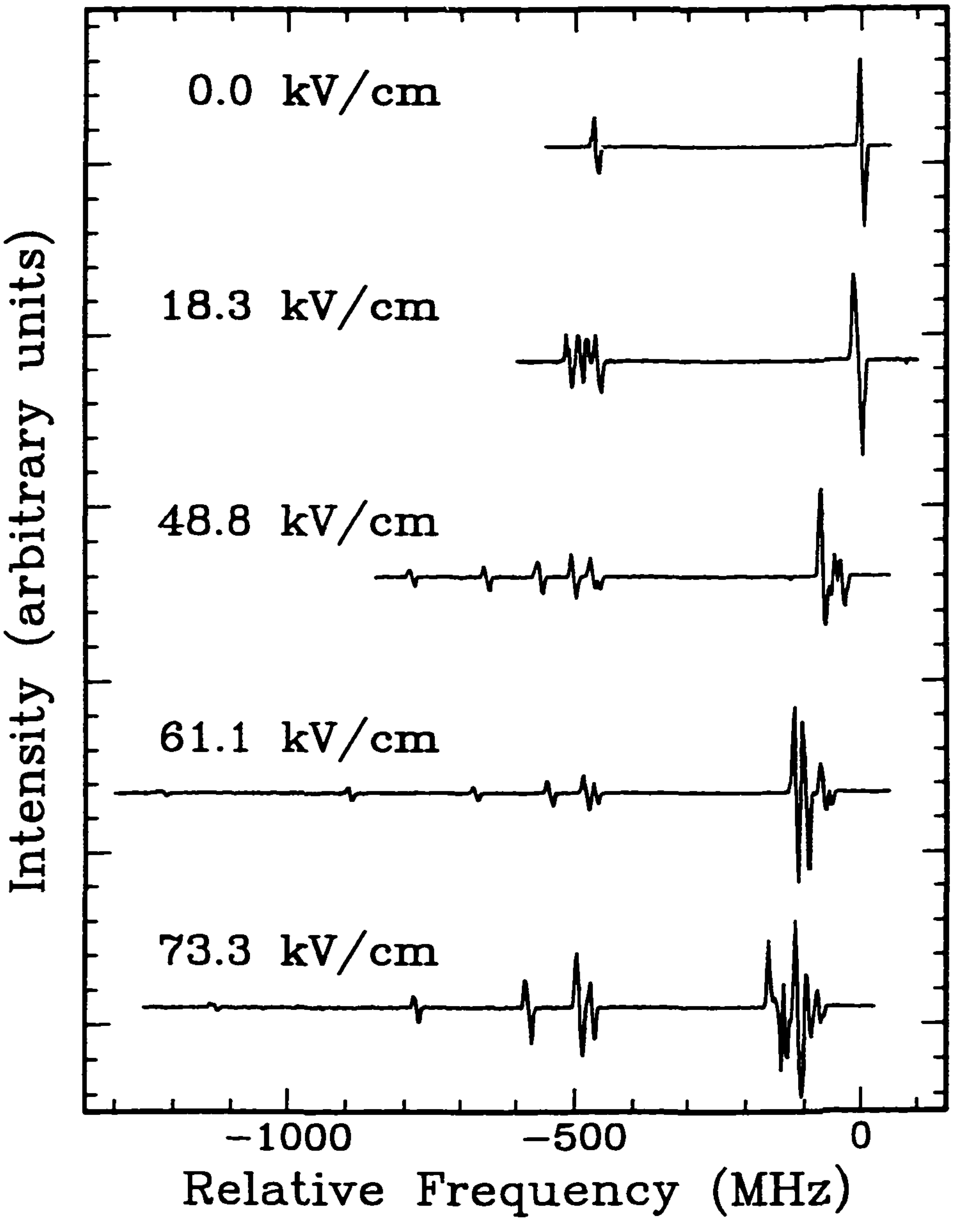

Figure 6.9: Electric Field dependence of Stark split spectrum of $\nu_2 + 3\nu_3$ R(4). The zero in the spectra is the field free position of R(4). 15 out the the 30 spectra collected are shown here and in Figures 6.10 and 6.11.

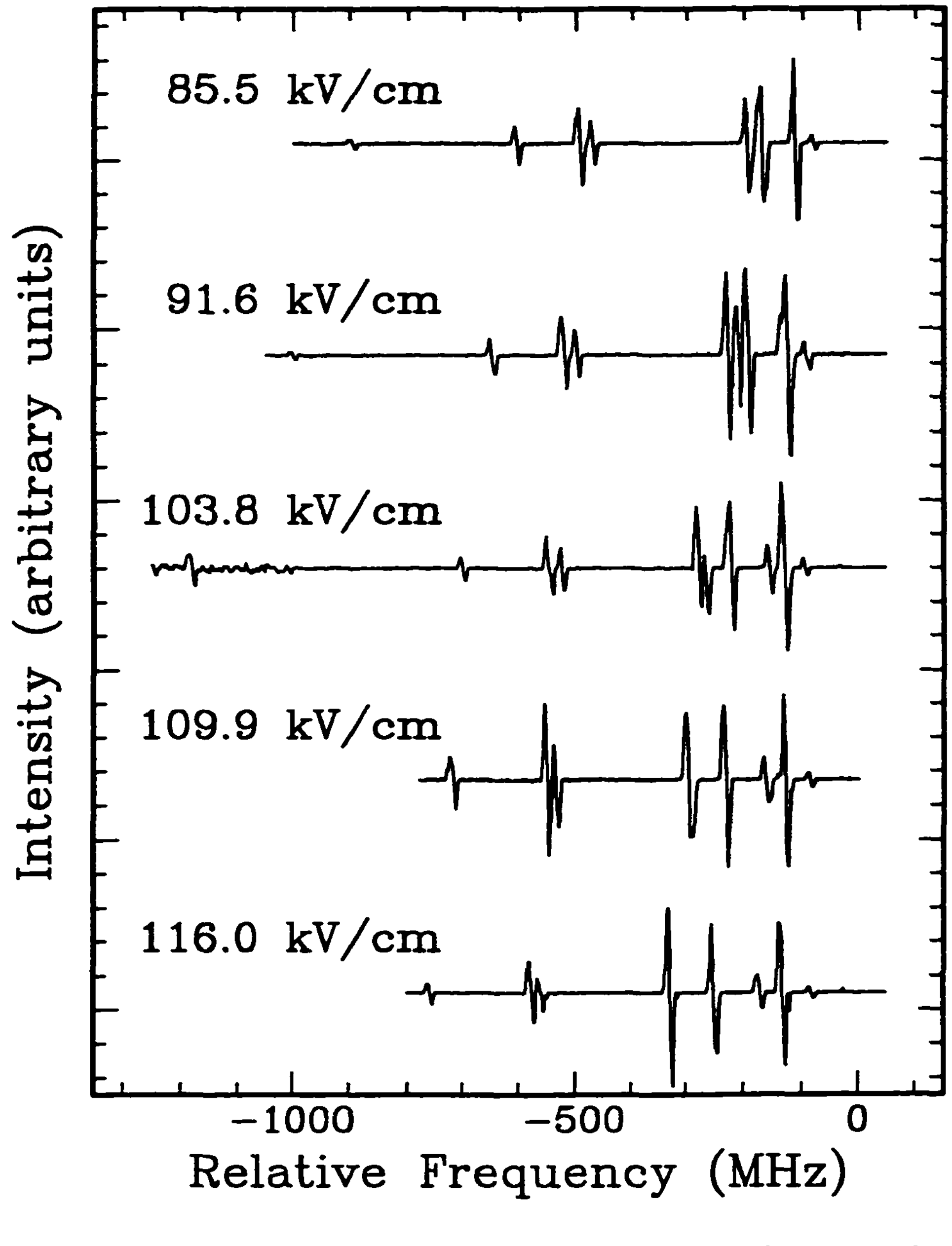

Figure 6.10: Electric Field dependence of Stark split spectrum of $\nu_2 + 3\nu_3$ R(4). The zero in the spectra is the field free position of R(4).

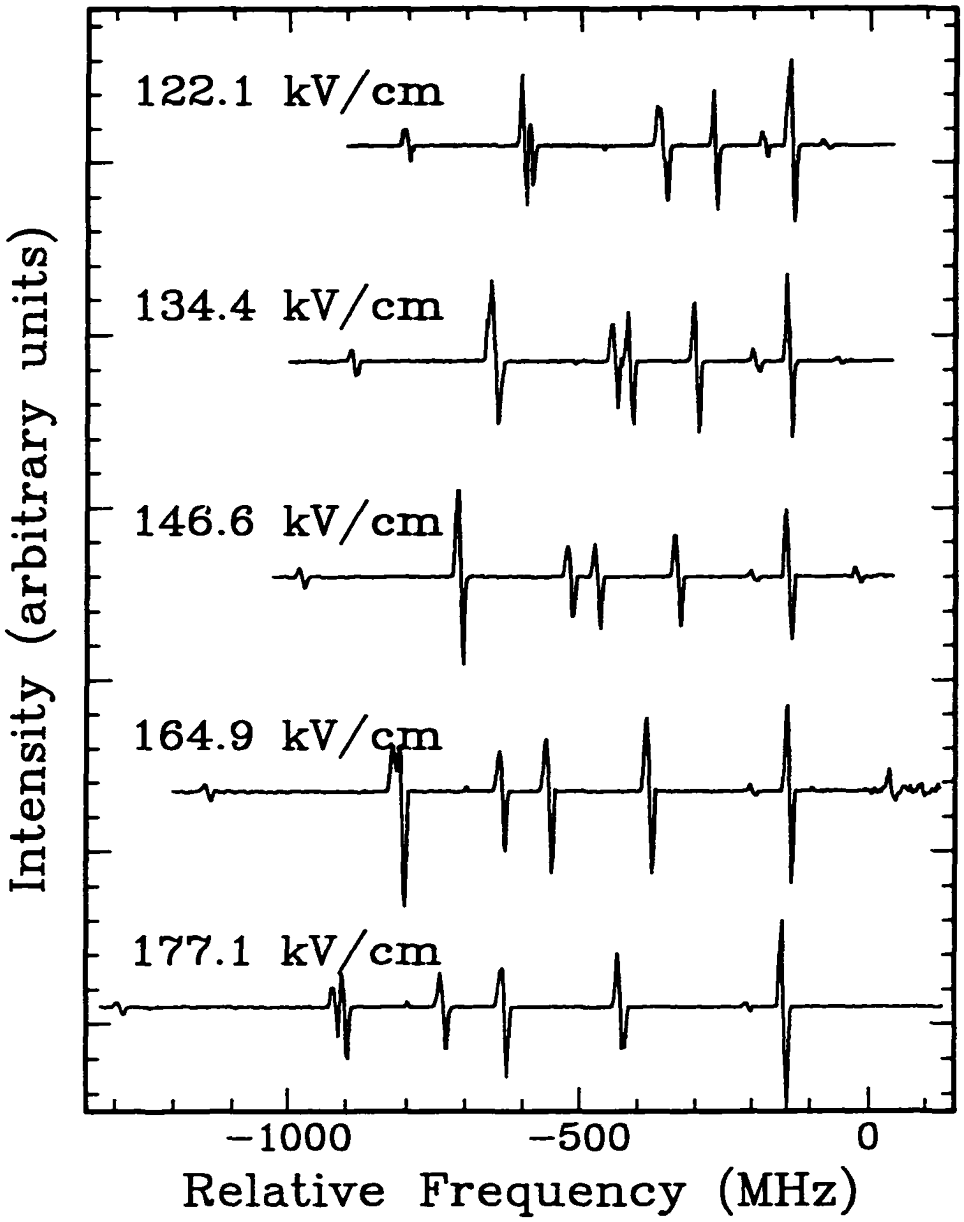

Figure 6.11: Electric Field dependence of Stark split spectrum of $\nu_2 + 3\nu_3$ R(4). The zero in the spectra is the field free position of R(4).

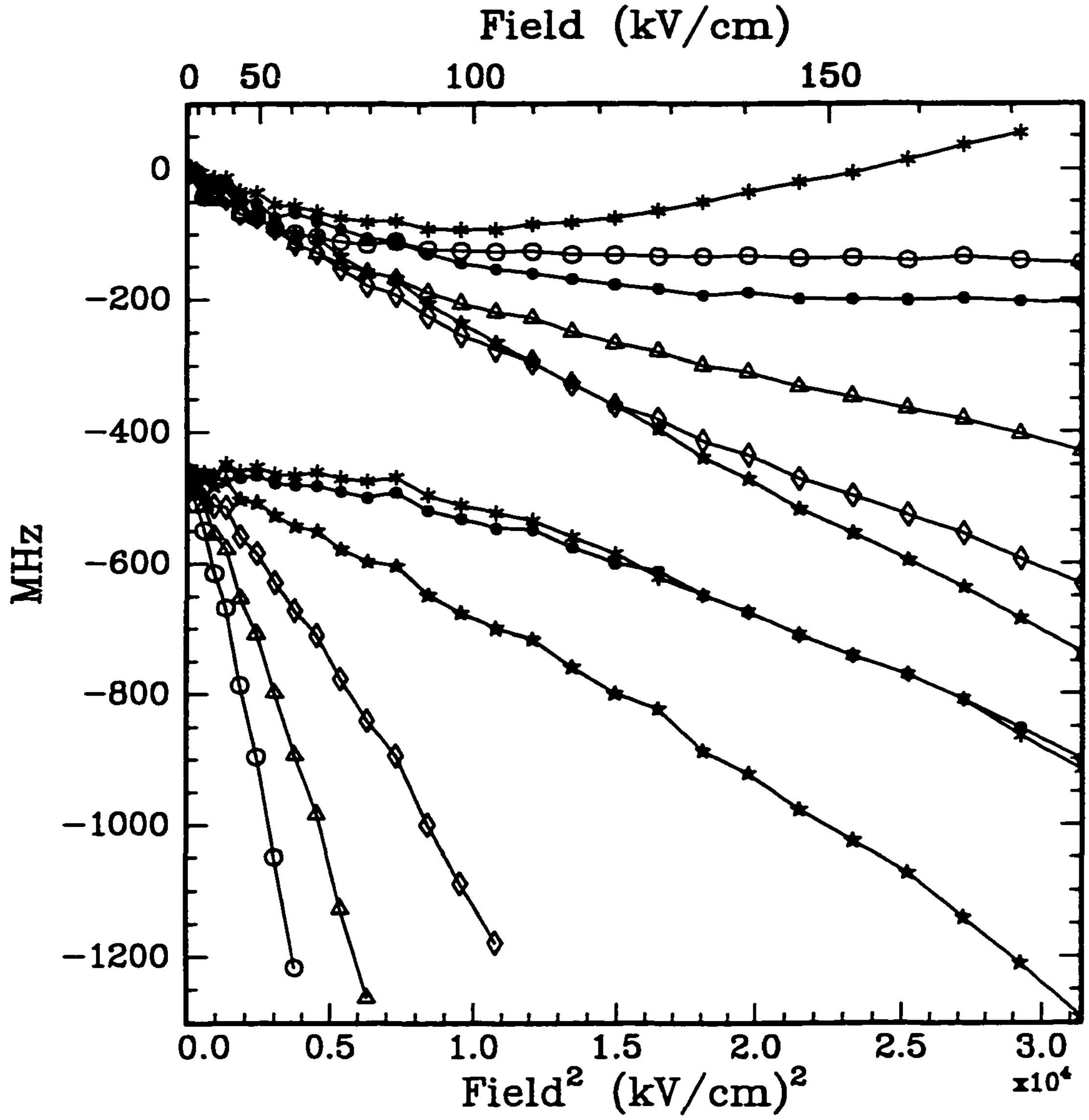

Figure 6.12: All of the R(4) data from Tables 6.3 and 6.4 is depicted here. The upper set of six lines is the data from the *normal* transitions and the lower set comes from the *rogue* transitions. The solid lines are are provided only as a visual aid. Note how rapidly the lower set of lines tune relative to the upper set.

Table 6.3: Field Dependent *normal* Line Positions for R(4)

Electric Field (kV/cm)	Peak ○ (MHz)	Peak △ (MHz)	Peak ◇ (MHz)	Peak ★ (MHz)	Peak ● (MHz)	Peak ∗ (MHz)
0.0	0.0	0.0	0.0	0.0	0.0	0.0
6.1	-0.4	-0.4	-0.4	-0.4	-0.4	-0.4
12.2	-2.8	-2.8	-2.8	-2.8	-2.8	-2.8
18.3	-5.9	-5.9	-5.9	-5.9	-5.9	-5.9
24.4	-42.4	-42.4	-33.5	-28.9	-25.8	-12.0
30.5	-42.5	-42.5	-35.3	-26.6	-20.8	-13.0
36.6	-44.5	-44.5	-44.5	-28.8	-19.1	-13.4
42.8	-67.9	-67.9	-67.9	-55.7	-43.6	-33.8
48.9	-73.7	-73.7	-73.7	-73.7	-52.5	-36.2
55.0	-90.4	-90.4	-90.4	-90.4	-74.2	-54.5
61.1	-98.7	-115.2	-115.2	-98.7	-66.9	-56.9
67.2	-104.5	-129.1	-129.1	-104.5	-80.2	-65.7
73.3	-111.5	-146.1	-153.9	-134.3	-92.0	-75.0
79.4	-116.1	-158.7	-179.2	-158.7	-106.0	-81.1
85.5	-111.4	-168.5	-194.0	-168.5	-111.4	-79.3
91.6	-123.6	-190.4	-226.0	-207.1	-130.0	-92.3
97.7	-125.9	-206.8	-255.0	-236.8	-144.8	-93.2
103.8	-127.7	-220.1	-276.1	-266.1	-154.1	-93.4
109.9	-127.0	-229.1	-295.4	-295.4	-161.1	-85.1
116.0	-132.0	-250.2	-327.9	-327.9	-169.8	-82.1
122.1	-132.3	-267.4	-359.9	-359.9	-178.0	-75.5
128.2	-134.5	-279.7	-380.8	-395.7	-184.8	-64.2
134.4	-134.8	-300.3	-413.7	-438.5	-194.6	-50.8
140.5	-133.1	-309.8	-434.8	-471.1	-189.9	-34.9
146.6	-137.2	-331.7	-470.8	-516.8	-199.8	-20.1
152.7	-136.5	-346.5	-496.7	-553.3	-200.4	-6.1
158.8	-140.5	-364.7	-525.6	-595.1	-201.8	14.1
164.9	-134.2	-380.0	-553.9	-636.5	-198.9	37.0
171.0	-140.2	-402.8	-592.6	-684.8	-203.3	55.1
177.1	-144.9	-428.8	-632.1	-736.4	-205.4	

Table 6.4: Field Dependent *rogue* Line Positions for R(4)

Electric Field (kV/cm)	Peak ● (MHz)	Peak ∗ (MHz)	Peak ⋆ (MHz)	Peak ◇ (MHz)	Peak △ (MHz)	Peak ○ (MHz)
0.0	-469.4	-469.4	-469.4	-469.4	-469.4	-469.4
6.1	-466.1	-466.1	-466.1	-466.1	-466.1	-466.1
12.2	-465.7	-465.7	-465.7	-465.7	-483.7	-483.7
18.3	-462.2	-462.2	-462.2	-475.2	-490.4	-508.7
24.4	-461.7	-461.7	-470.9	-487.0	-511.7	-549.1
30.5	-465.5	-465.5	-481.3	-511.6	-554.7	-614.4
36.6	-451.9	-448.3	-474.3	-513.5	-577.4	-668.1
42.8	-468.9	-460.1	-502.2	-558.1	-653.2	-786.3
48.9	-465.2	-453.4	-506.9	-583.9	-707.8	-895.7
55.0	-477.6	-464.0	-526.5	-629.1	-797.9	-1048.9
61.1	-480.6	-465.8	-542.9	-672.3	-893.2	-1216.4
67.2	-481.9	-461.1	-550.8	-710.6	-983.8	
73.3	-490.2	-470.6	-578.2	-777.2	-1126.7	
79.4	-499.6	-474.8	-597.0	-840.4	-1262.1	
85.5	-491.8	-469.0	-603.8	-894.3		
91.6	-519.3	-496.0	-648.9	-999.5		
97.7	-531.5	-511.3	-676.3	-1089.4		
103.8	-546.5	-523.0	-700.2	-1178.8		
109.9	-548.4	-534.5	-716.7			
116.0	-575.6	-559.7	-759.3			
122.1	-600.1	-585.5	-799.8			
128.2	-612.0	-621.9	-823.3			
134.4	-648.9	-648.9	-887.5			
140.5	-674.8	-674.8	-921.8			
146.6	-709.6	-709.6	-977.0			
152.7	-741.8	-741.8	-1024.4			
158.8	-771.1	-771.1	-1073.9			
164.9	-809.0	-809.0	-1141.1			
171.0	-852.4	-864.0	-1210.4			
177.1	-900.7	-916.3	-1291.0			

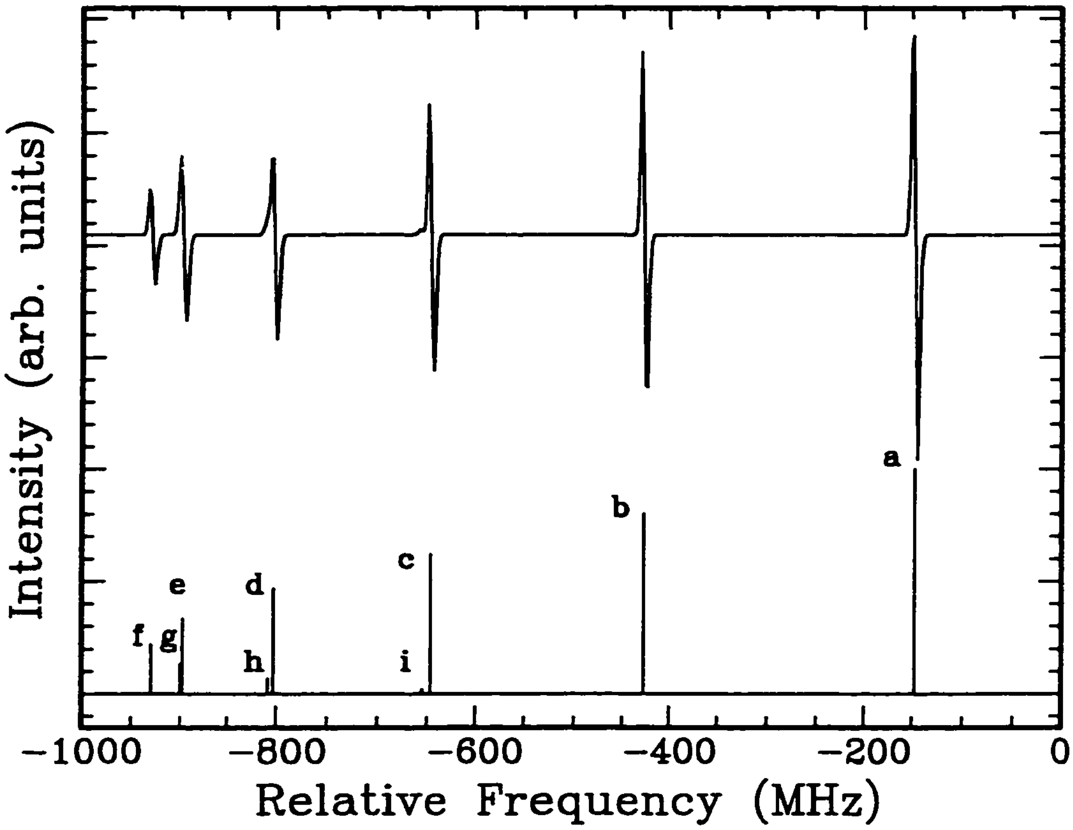

Figure 6.13: The top of the diagram depicts the first derivative of the computed Stark split spectrum of an R(4) type of transition at 177.1 kV/cm with a line width of 6 MHz. Beneath it is a "stick" spectrum showing the precise positions of the nine peaks. The M transitions, along with their calculated intensities (in parentheses), are as follows :

a $M = 5 \leftarrow 4$ (45)
b $M = 4 \leftarrow 3$ (36)
c $M = 3 \leftarrow 2$ (28)
d $M = 2 \leftarrow 1$ (21)
e $M = 1 \leftarrow 0$ (15)
f $M = 0 \leftarrow -1$ (10)
g $M = -1 \leftarrow -2$ (6)
h $M = -2 \leftarrow -3$ (3)
i $M = -3 \leftarrow -4$ (1)

peak approximately 500 MHz to the blue of the R(5) field free position. Since the three most intense peaks were well resolved at lower fields, it was possible to assign the $M = 4 \leftarrow 3$ to this third most intense transition. Hence, in order of decreasing intensity, the four rapidly tuning transitions can be assigned to the $M = 3 \leftarrow 2$, $2 \leftarrow 1$, $1 \leftarrow 0$ and $0 \leftarrow -1$ transitions.

6.4 Discussion

According to the infrared selection rules, transitions originating in the ground vibrational state of acetylene (Σ_g^+) must terminate in a vibrational state of *ungerade* symmetry [3]. The second, *rogue* peak seen in the spectrum of R(4) at zero electric field must therefore also belong to a vibrational state of *ungerade* symmetry. The coupling described previously between the 04^+ and 04^- states of acetylene was of course between *gerade* and *ungerade* vibrational states. The 04^+ state provides a contribution to the polarisability of the 04^- state according to the sum-over-states methodology described in Chapter 1. Similarly, the $1|03^+$ ($|1120^00^0\rangle$) state will also provide a contribution to the polarisability of the $1|03^-$ ($|0130^00^0\rangle$) state. However, the *rogue* vibrational state is not included in the sum-over-states for the polarisability of the $1|03^-$ state and anomalies seen in the Stark split spectra of R(3) and R(5) must be due to coupling via Fermi, Darling-Dennison or Coriolis resonances. The question arises: "Can the identity of the *rogue* state as well as the coupling mechanism(s) be determined from the data at hand?"

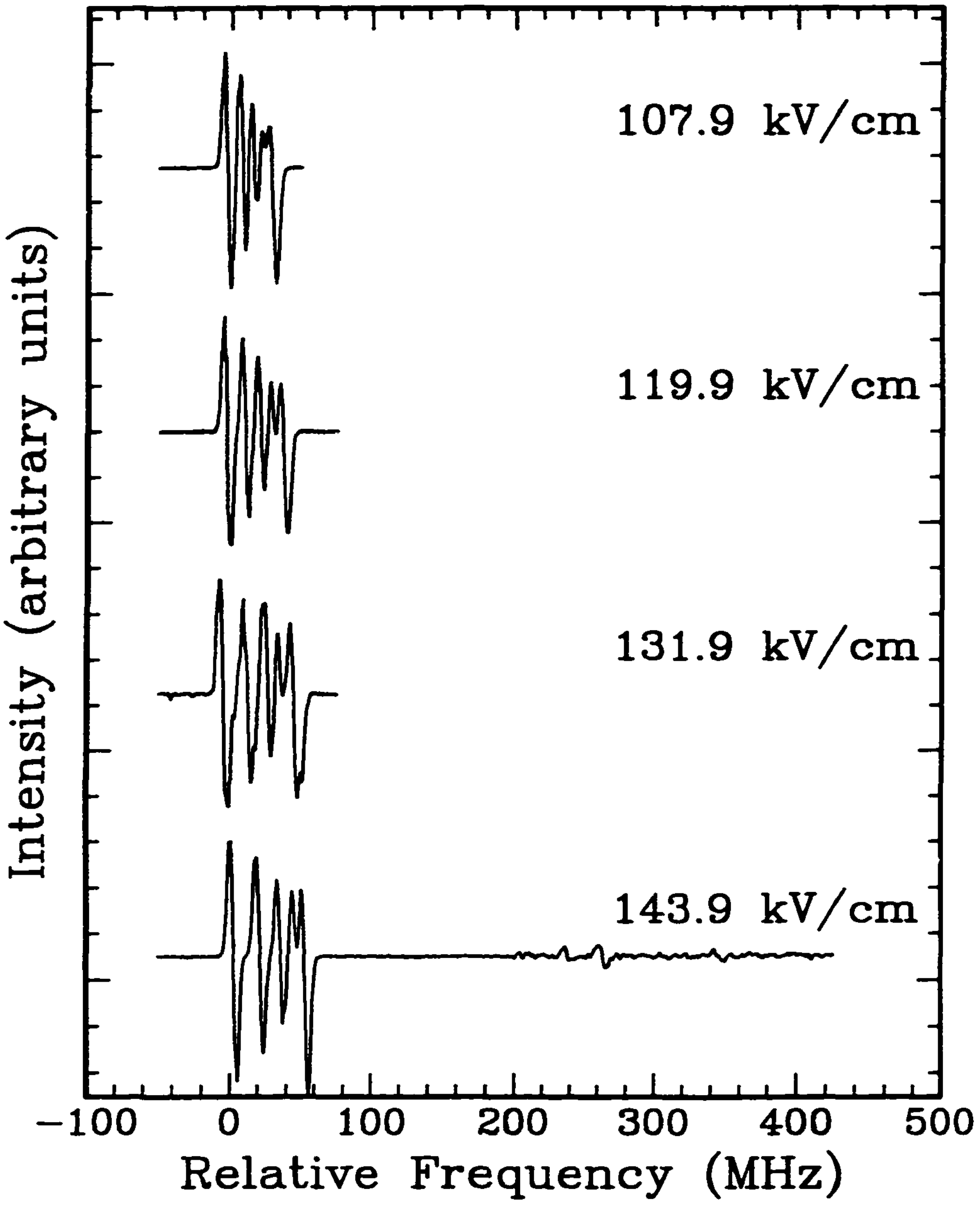

Figure 6.14: Electric Field dependence of Stark split spectrum of $\nu_2 + 3\nu_3$ R(5). The zero in the spectra is the field free position of R(5). 16 of the 34 spectra collected are depicted here and in Figures 6.15 to 6.17.

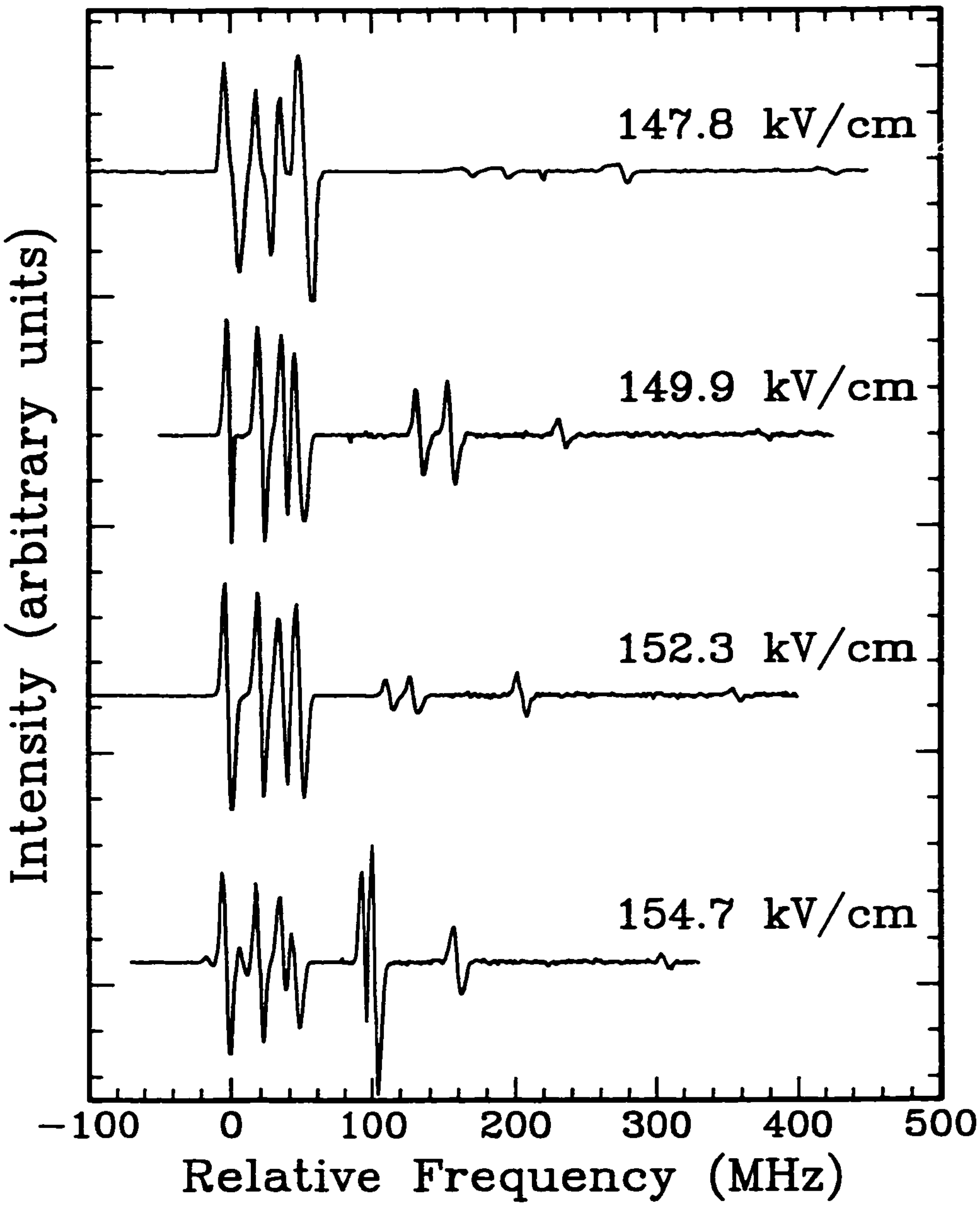

Figure 6.15: Electric Field dependence of Stark split spectrum of $\nu_2 + 3\nu_3$ R(5). The zero in the spectra is the field free position of R(5).

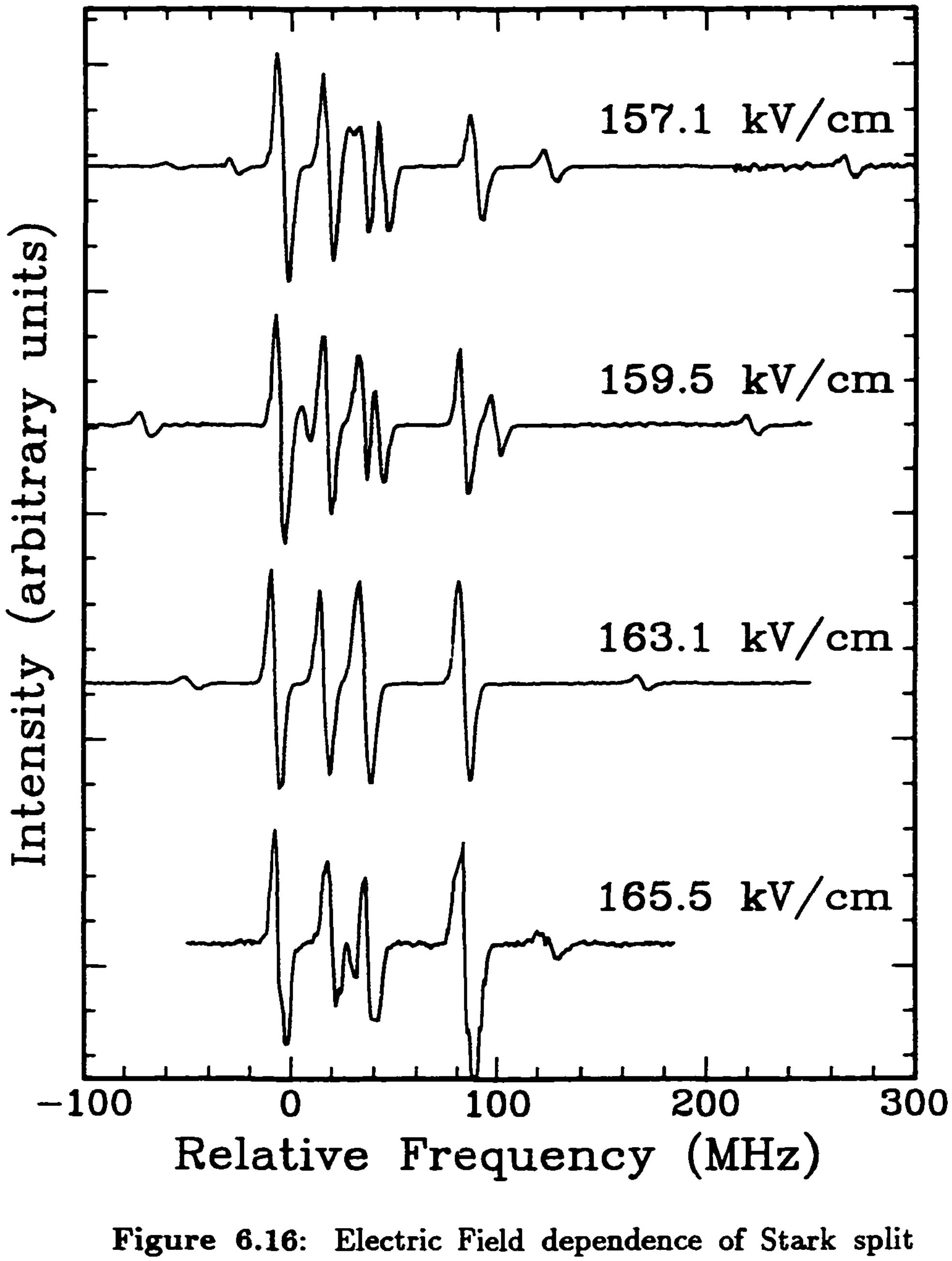

Figure 6.16: Electric Field dependence of Stark split spectrum of $\nu_2 + 3\nu_3$ R(5). The zero in the spectra is the field free position of R(5).

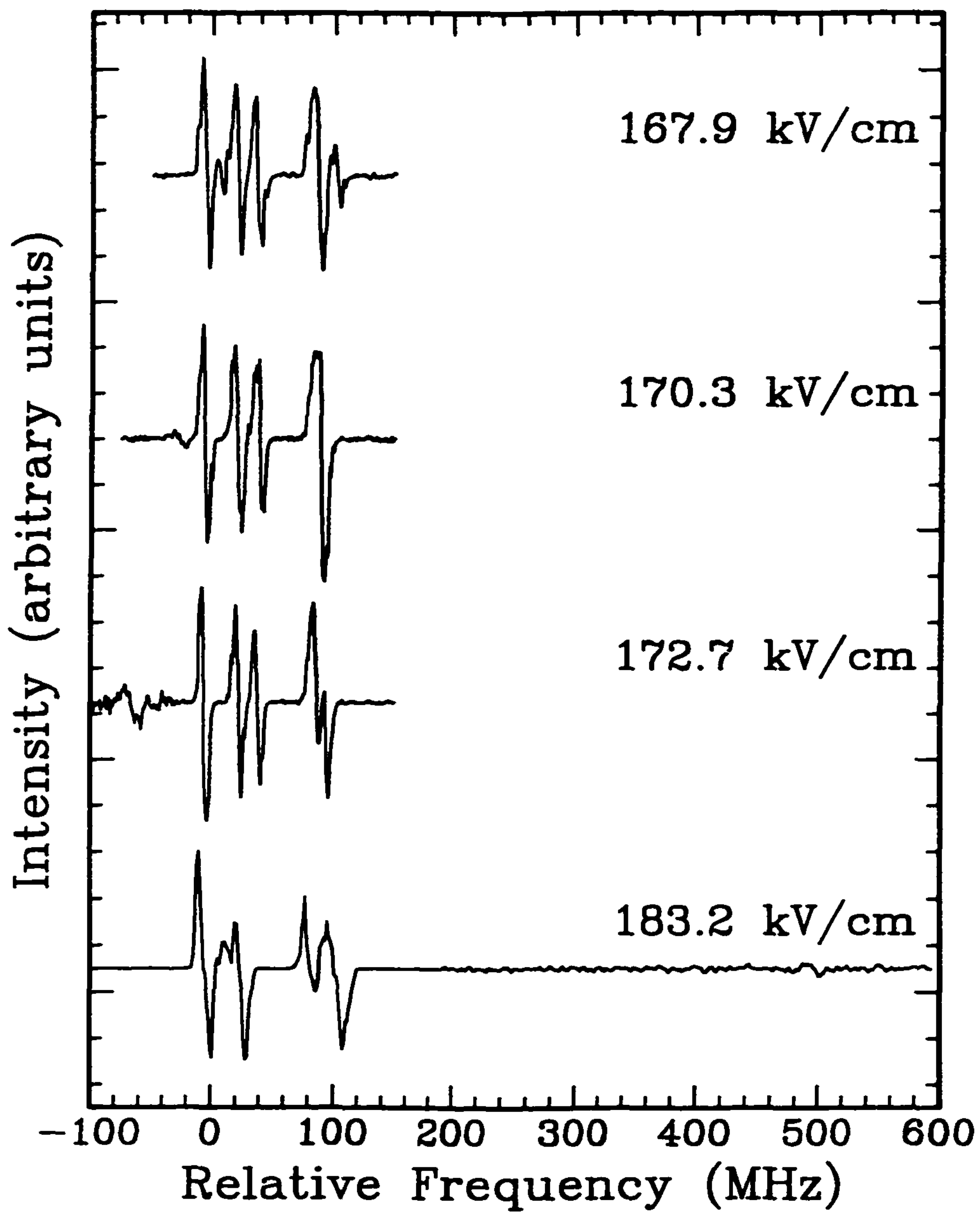

Figure 6.17: Electric Field dependence of Stark split spectrum of $\nu_2 + 3\nu_3$ R(5). The zero in the spectra is the field free position of R(5). A fifth *rogue* peak appears at approximately +500 MHz in the bottom spectrum.

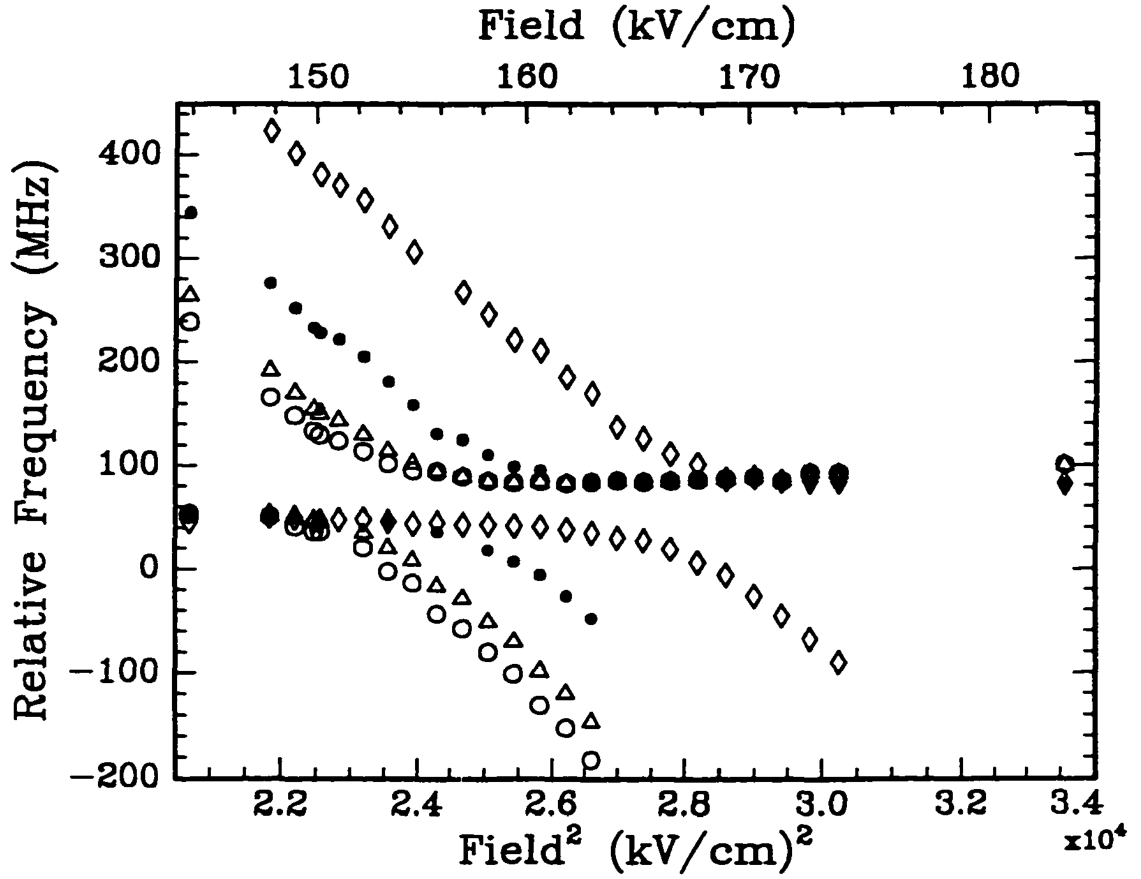

Figure 6.18: Electric Field dependence of the *normal* and *rogue* peaks in the $\nu_2+3\nu_3$ R(5) Stark field perturbed spectrum. Zero frequency is the field free position of R(5). The data plotted here is listed in Table 6.5.

Table 6.5: Field Dependent *rogue* and *normal* Line Positions for R(5)

Electric Field (kV/cm)	$M = 0 \leftarrow -1$		$M = 0 \leftarrow -1$		$M = 2 \leftarrow 1$		$M = 3 \leftarrow 2$	
	normal (MHz)	*rogue* (MHz)	*normal* (MHz)	*rogue* (MHz)	*normal* (MHz)	*rogue* (MHz)	*normal* (MHz)	*rogue* (MHz)
143.9	53.0	238.7	53.0	263.9	53.0	344.2	45.9	
147.8	50.9	165.9	50.9	192.0	50.9	275.9	50.9	423.2
149.0	40.8	148.4	49.4	170.1	49.4	252.0	49.4	401.7
149.9	36.2	133.4	45.8	154.7		233.0	45.9	
150.2	36.2	129.3	45.8	150.5	45.8	228.2	45.8	380.9
151.1		123.7		143.7		221.8	47.7	370.7
152.3	20.4	113.6	35.1	129.7		205.1	47.8	356.3
153.5	-2.4	101.7	20.4	114.1	45.9	181.1	45.9	330.8
154.7	-13.7	94.7	8.2	102.2		158.9	43.6	306.1
155.9	-43.4	94.4	-16.4	94.4	36.3	131.0	45.2	
157.1	-57.6	89.1	-28.7	89.1		125.0	43.1	267.5
158.3	-80.1	84.9	-51.1	84.9	18.3	110.4	43.0	246.3
159.5	-101.0	83.4	-70.2	83.4	7.2	98.7	41.6	221.3
160.7	-131.0	84.3	-98.4	84.3	-6.0	94.9	40.8	210.7
161.9	-152.4	82.5	-119.8	82.5	-26.6		38.0	185.5
163.1	-182.4	83.8	-146.4	83.8	-47.9	83.8	35.0	169.9
164.3		85.2		85.2		85.2		137.5
165.5		83.9		83.9		83.9	27.5	126.1
166.7		84.8		84.8		84.8	19.2	111.0
167.9		86.5		86.5		86.5	6.7	101.5
169.1		87.1		87.1		87.1	-6.0	87.1
170.3		88.8		88.8		88.8	-26.5	88.8
171.5		85.0		85.0		85.0	-45.2	85.0
172.7		93.4		93.4		85.0	-67.1	85.0
173.9		92.9		92.9		84.4	-89.8	84.4
183.2		100.4		100.4		81.9		81.9

In what follows it will be assumed that the *rogue* peaks seen in the Stark split spectra of R(3) and R(5) belong to the same vibrational band as the *rogue* peak in the zero Stark field R(4) spectrum.

Figure 6.19 depicts a plot of the *rogue* and *normal* peak positions as a function of the square of the electric field for the R(3) transition. What is seen could be characterised as a typical example of the non-crossing rule that is often associated with potential curves of electronic states [104]. The essence of this rule lies in the non-crossing of two states of the same symmetry species. In this particular case, the correlation between the *rogue* and *normal* peaks of R(3) before and after the non-crossing region identifies the excited M_J *rogue* states. In the vicinity of the non-crossing region the labels *normal* and *rogue* have little meaning. Figure 6.4 illustrates this point well; the *rogue* and *normal* peaks at 119.9 kV/cm and 121.1 kV/cm are approximately equal in intensity, suggesting each peak is approximately 50% *rogue* and 50% *normal*. Plotting the ratio of the *rogue* to the *normal* peak areas as a function of the difference between the peak positions is another indication of the *rogue/normal* character mixing. Figure 6.20 shows how the *rogue* peak borrows intensity as it passes through the *normal* R(3) region of the Stark split spectrum. At large frequency separations the *rogue* peaks have very little intensity (if any at all) and as the *rogue* peaks approach the minimum frequency separation (approximately 270 MHz) they reach a maximum intensity of 50% of their corresponding *normal* peaks. These *normal/rogue* correlations form the basis for establishing the M_J identity of the *rogue* peaks.

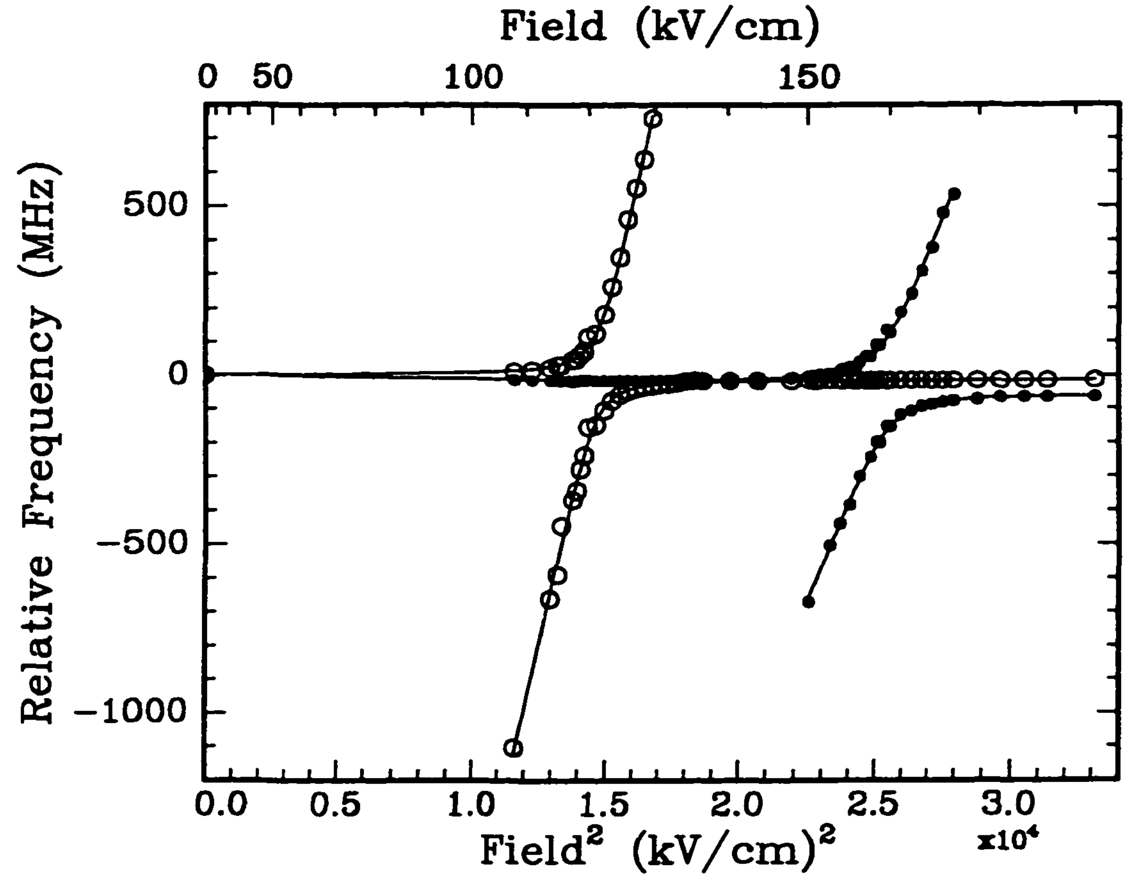

Figure 6.19: Illustrated is the R(3) data for both *rogue-normal* pairs of transitions. The $M = 4 \leftarrow 3$ data are represented by the ○ and the $M = 3 \leftarrow 2$ data are depicted with ●. The solid lines are the result of a fit to Equation 6.2 for each pair with C fixed at 135 MHz.

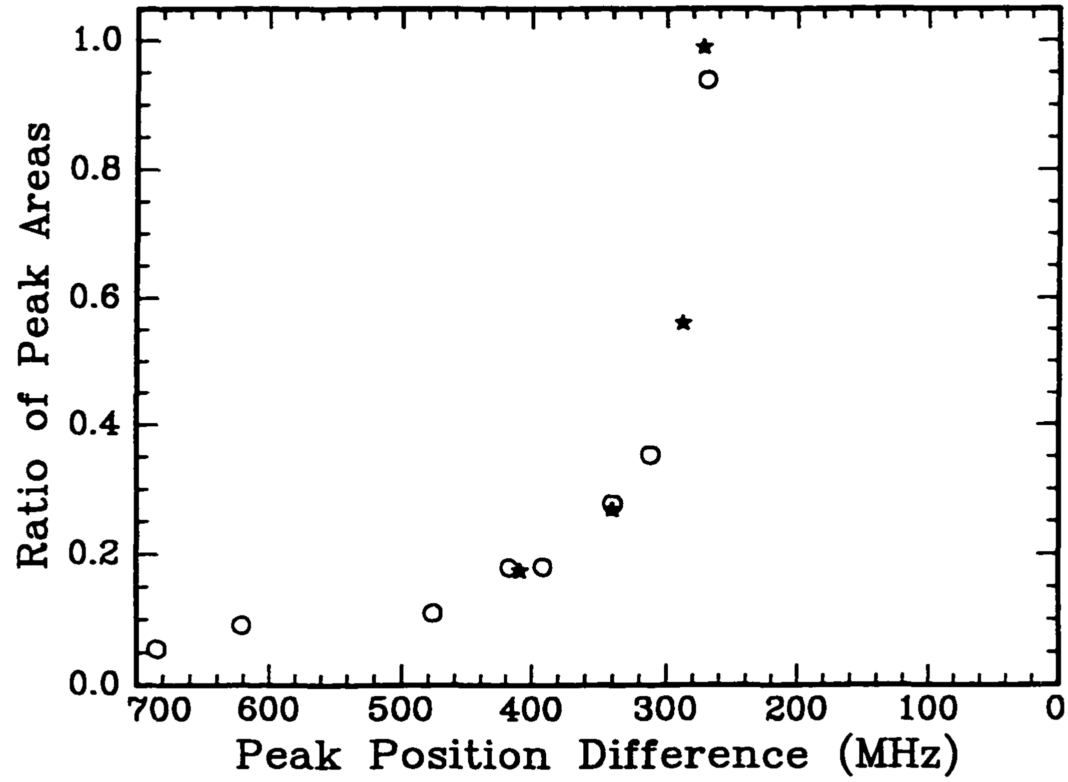

Figure 6.20: The ratio of the *rogue* to *normal* peak areas for the first *rogue/normal* pair of peaks ($M = 4 \leftarrow 3$ transition) is plotted against the difference in peak positions. The circles depict the *rogue* peaks on the red side of the R(3) zero field position and the stars represent the *rogue* peaks on the high frequency side. The minimum difference corresponds to an electric field of 121.1 kV/cm. This is a typical example of intensity borrowing.

A modification of the equation used earlier for the Stark effect for two nearby states (Equation 5.5) that incorporates the field dependence of the *rogue* and *normal* peaks can be used to describe the observations:

$$\begin{aligned} W_{h/l} &= \left(\frac{W_N + W_R}{2}\right) \pm \left[\left(\frac{W_N - W_R}{2}\right)^2 + C^2\right]^{1/2} \\ W_N &= W_N^{\circ} + t_N F^2 \\ W_R &= W_R^{\circ} + t_R F^2 \,. \end{aligned} \qquad (6.2)$$

The energies of the *normal* and *rogue* J states in the absence of coupling and the Stark field are given by W_N° and W_R°, respectively. W_N and W_R are the Stark field perturbed energies of the M_J states with tuning rates t_N and t_R (MHz/kV^2). C is a coupling constant with the same units as $W_{h/l}$ (MHz). In the case of R(3), W_h and W_l represent the *normal* and *rogue* states, since the *normal* transitions are at higher energy in the absence of the Stark field.

The Stark field tuning rates for the *normal* peaks can be calculated from Equation 5.2 and the polarisability data given in Table 6.1. The tuning rate for $M = 4 \leftarrow 3$ is 4.293×10^{-4} MHz/kV^2 and for $M = 3 \leftarrow 2$ it is -0.001048×10^{-3} MHz/kV^2. Plotting the difference of the line positions of the *normal-rogue* peak pairs provides a simple means of establishing the value of the coupling constant, C (Figure 6.21).

Taking the difference between W_h and W_l (Equation 6.2) produces

$$W_h - W_l = \Delta W = 2\left[\left(\frac{W_N - W_R}{2}\right)^2 + C^2\right]^{1/2}. \tag{6.3}$$

The value of F^2 at the minimum was found by taking the first derivative of ΔW with respect to F^2 and setting it to zero. Some algebraic manipulation produces $F^2_{\text{min}} = (W_R^0 - W_N^0)/(t_N - t_R)$, which can be substituted back into Equation 6.3 resulting in

$$C = {}^1\!/\!_2\, \Delta W_{\text{min}}\,. \tag{6.4}$$

From the plot of the data in Figure 6.21, the best value of the coupling constant to fit both curves is 135 MHz.

At low electric fields the Stark split R(3) spectrum was fit to the second order Stark equation (Equation 5.2). This leads one to believe that at these fields, the *rogue–normal* interaction is non-existent (or negligible) and, therefore, at zero electric field it is assumed that $W_N = W_N^0 = 0$. Using a value of 135 MHz for the coupling constant and calculated *normal* tuning rates, the data in Figure 6.19 can be fit to Equation 6.2, producing an average W_R^0 of -5350±110 MHz. Also from the fit, the tuning rates for the *rogue* $M = 4 \leftarrow 3$ and $M = 3 \leftarrow 2$ transitions were determined to be 0.3634±0.0008 MHz/kV^2 and 0.2092±0.0004 MHz/kV^2, respectively (errors are given as 2σ). Since the tuning rates of specific *rogue* M transitions are known, the second order Stark equation was used to calculate the polarisability and anisotropy

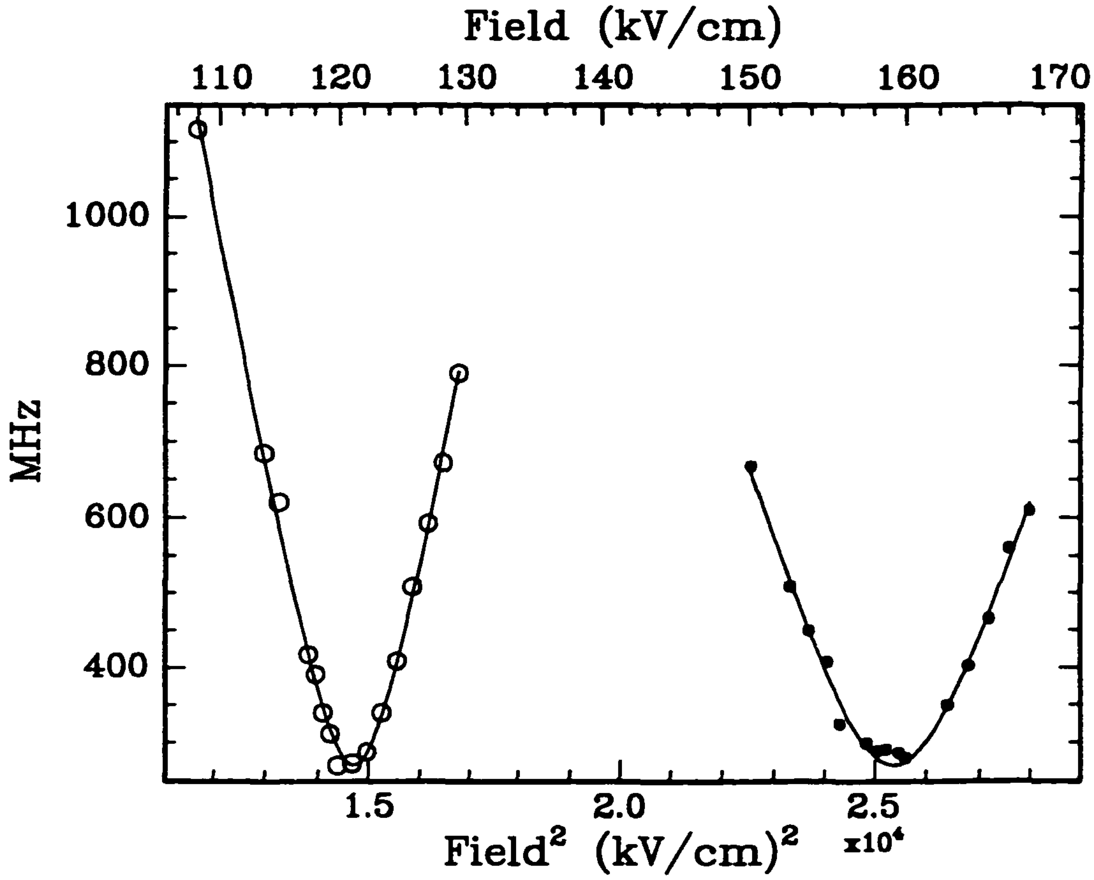

Figure 6.21: Difference in line positions of the *normal* and *rogue* peaks. The $M = 4 \leftarrow 3$ data are represented by the ○ and the $M = 3 \leftarrow 2$ data are depicted with ●. The solid lines are the result of a fit to the difference in the $W_{h/l}$ energies (see Equation 6.3). The best fit for both was obtained with a coupling constant, C, of 135 MHz.

of the polarisability. For $J' = 4$ of the *rogue* state, $\alpha = -184$ $\AA^3$ and $\Delta\alpha = 1013$ $\AA^3$. However, using these results to calculate the polarisability tensor components produces a large, negative value for $\alpha_\perp$ (-522 $\AA^3$). This seems to indicate that the second order Stark equation (derived assuming a parallel vibrational transition) is not appropriate for these particular ro-vibrational transitions. It should be noted that the tuning rates for these rogue transitions scale as M^2, which is what one would expect for a perpendicular type vibrational transition .

The data for the R(5) *rogue–normal* interaction can be analysed in the same fashion as the R(3) data. Figure 6.22 depicts the avoided crossing curves for the various M transitions. In this case, the coupling constant and W_R^0 were determined from fits to four sets of data and could therefore be statistically averaged. The values are C = 45.8± 1.6 MHz and W_R^0 = 1600± 40 MHz. Fitting the line positions of the *rogue* and *normal* peaks using these values for the coupling constant and W_R^0 gives tuning rates for the *rogue* $M = 0 \leftarrow -1$, $M = 1 \leftarrow 0$, $M = 2 \leftarrow 1$ and $M = 3 \leftarrow 2$ transitions as -0.06668±0.00024 MHz/kV^2, -0.06536±0.00026 MHz/kV^2, -0.06136±0.0003 MHz/kV^2 and -0.05504±0.00028 MHz/kV^2, respectively. As was done for R(3), the second order Stark equation can be used to calculate α and $\Delta\alpha$ from the four tuning rates. Any pair of M transitions could be used to solve the Stark equation, therefore six sets of polarisability data were computed and averaged. As a further validation of the *rogue* peak identities, the M transition assignments were varied while calculating α and $\Delta\alpha$. Only when the above stated assignments were used, did the calculations produce consistent results. For $J' = 6$ of the *rogue* state, $\alpha = 61.71 \pm 0.29\text{Å}^3$ and $\Delta\alpha = 128.4 \pm 2.1\text{Å}^3$.

Given the polarisability data for the *rogue* R(5) transition it would seem to be possible to predict the appearance of the fifth peak seen at 183.2 kV/cm (Figure 6.17). A second order Stark calculation places the fifth peak ($M = 4 \leftarrow 3$) at the zero field position of the *normal* R(5) transition for an applied electric field of 183.2 kV/cm. However, the experiment shows it to be still 500 MHz to the blue. A possible explanation for this discrepancy comes from Figure 6.22. The incoming *rogue* peaks slow down as they approach the *normal* R(5) spectrum and acquire more *normal* character. However, the tuning rates calculated for the *rogue* transitions are only valid when the *normal-rogue* interaction is negligible. Since the *rogue* peaks acquire intensity by borrowing it from the *normal* peaks, as soon as a *rogue* peak is visible in the spectrum the *normal-rogue* interaction cannot be considered negligible.

The analysis of the R(4) data is not as "simple" as that of R(3) and R(5). A *rogue* peak is present in the absence of the electric field (see top of Figure 6.9, page 112) and, hence, it must be assumed that the two states are already strongly coupled. Following the outline provided by Equation 5.3 for the mixing of two zero order wave functions, the wave function coefficients, a and b, are (page 38, reference [30])

$$a = \frac{\sqrt{2}}{2}\left(\frac{\sqrt{(W_N^0 - W_R^0)^2 + 4C^2} + (W_N^0 - W_R^0)}{\sqrt{(W_N^0 - W_R^0)^2 + 4C^2}}\right)^{1/2}$$

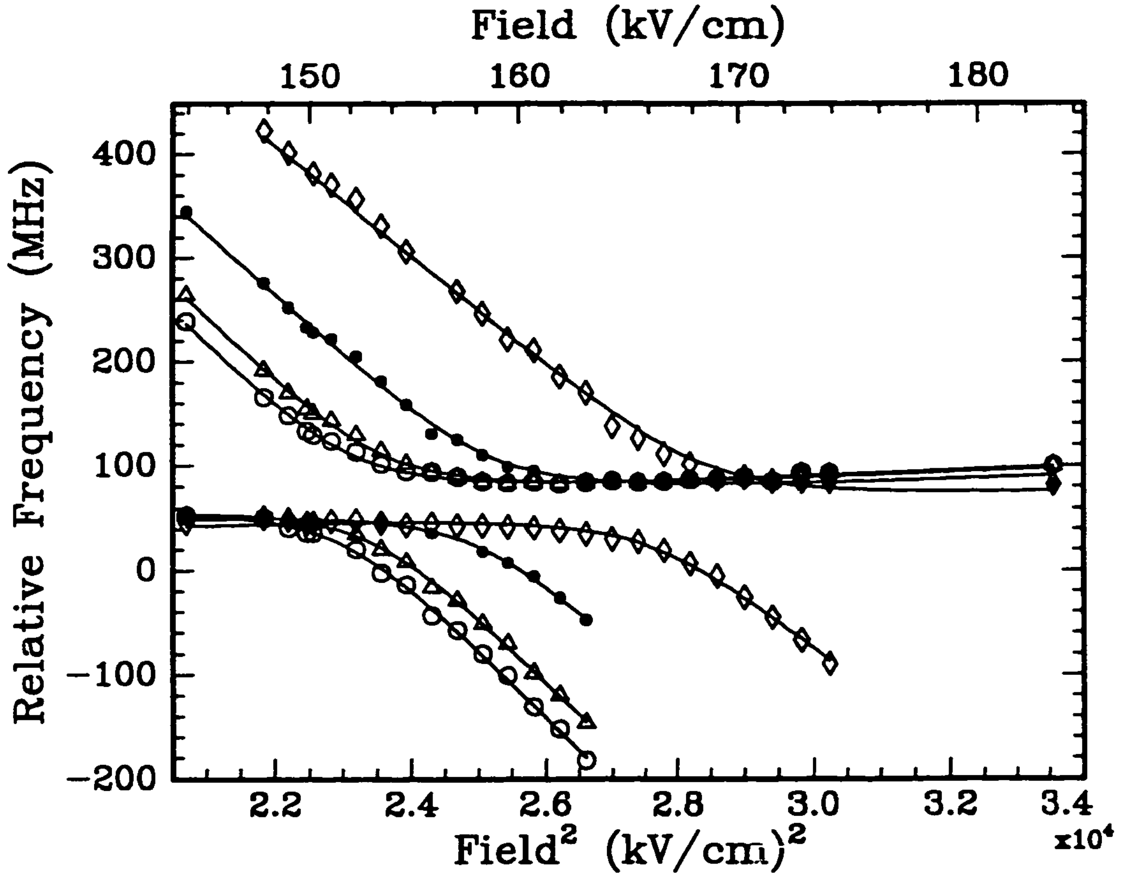

Figure 6.22: The data for the R(5) *rogue-normal* pairs of interacting transitions is depicted here. The ○, △, ● and ◇ represent the $M = 0 \leftarrow -1$, $M = 1 \leftarrow 0$, $M = 2 \leftarrow 1$ and $M = 3 \leftarrow 2$ transitions respectively. The solid line is the result of a fit to Equation 6.2 for each *rogue-normal* data pair.

$$b = \frac{\sqrt{2}}{2}\left(\frac{\sqrt{(W_N^0 - W_R^0)^2 + 4C^2} - (W_N^0 - W_R^0)}{\sqrt{(W_N^0 - W_R^0)^2 + 4C^2}}\right)^{1/2} \qquad (6.5)$$

such that $a^2 + b^2 = 1$.

Solving these equations together with the data from the zero electric field spectrum ($a^2/b^2 = 2.89$, ratio of the *normal* to *rogue* peak areas), gives $a = 0.862$ and $b = 0.507$, a coupling constant of 205 MHz and a $W_N^0 - W_R^0$ of 228 MHz ($W_N^0 \neq W_N$ at zero electric field). Since at all of the applied Stark fields there are always *rogue* peaks present, it is not possible to use the second order Stark equation to obtain reliable polarisability data for the *normal* R(4) spectrum. However, upon examining the R(4) spectra at high electric fields (Figure 6.11, page 114), one can see that the tuning rates of the two most intense peaks (depicted by ○ and △ in Figure 6.23) have slowed considerably compared to the other peaks. Also, the intensity pattern among the first three most intense *normal* peaks is very similar to that of the first three peaks in the calculated spectrum (45:36:28, see top of Figure 6.13, page 118). This may indicate that the *rogue* peaks with which they were coupled have shifted far enough away in frequency that their influence on the *normal* peaks is negligible. The two *rogue* peaks that disappeared from the spectrum at the lower electric fields are the best candidates for this pairing. The three most intense *normal* peaks can then be assigned to the $M = 5 \leftarrow 4$, $M = 4 \leftarrow 3$ and $M = 3 \leftarrow 2$ transitions.

Assuming that the interaction between the *normal* and *rogue* states for the two

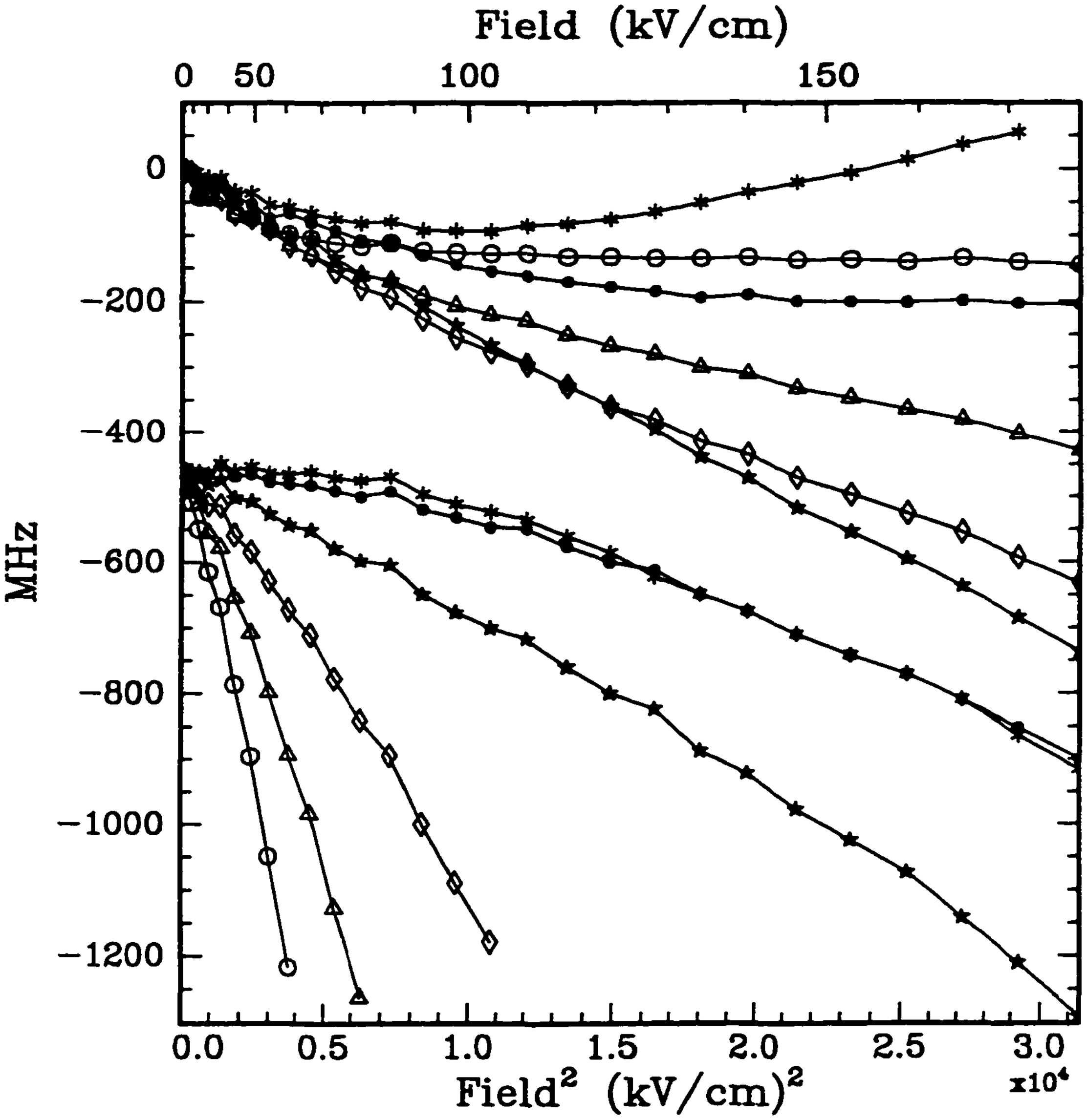

Figure 6.23: All of the R(4) data from Tables 6.3 and 6.4 is depicted here. The upper set of six lines is the data from the *normal* transitions and the lower set comes from the *rogue* transitions. The symbols used reflect the "best guess" of possible *normal-rogue* pairs. The M transition labels are not provided here, since none of the spectra seem to follow the second order Stark effect. Possible M assignments and reasons for pairing are discussed in the text (see page 135). The solid lines are not fits to any equations and are provided only as a visual guide.

most intense *normal* peaks is negligible at the higher applied fields ($\geq$171.0 kV/cm), one can use the second order Stark equation (Equation 5.2) to calculate the positions of these two peaks at 171.0 kV/cm. The spectrum at 177.1 kV/cm was not chosen for this calculation, since the second most intense peak lost some intensity when the BUC temporarily fell off resonance during the scan. The results of this partial "fit" to the spectrum at 171.0 kV/cm are $\alpha = 23.53$ $\AA^3$ and $\Delta\alpha = 71.3$ $\AA^3$. A comparison of the calculated and measured spectrum at 171.0 kV/cm is illustrated in Figure 6.24. Not only do the intensities of the first few peaks match the calculated spectrum well, but the line positions for the first two peaks do also. It is interesting to note that the two most intense *rogue* peaks (-852 MHz and -844 MHz) appear close to the calculated position of the two weakest *normal* peaks (-873 MHz and -843 MHz). Their intensities are greater than the calculated ones, because during the measurement, they were magnified by a factor of two over the *normal* peaks by adjusting the gain on the lock-in amplifier. The peak position agreement is even better for the Stark split spectrum at 177.1 kV/cm. It is possible that these two *rogue* peaks are coupled with the weakly visible *normal* peaks seen at -134 MHz and 37 MHz (Figure 6.11, 164.9 kV/cm). Both of these two weak *normal* peaks continually lost intensity as the electric field was increased, while their (possible) *rogue* counterparts have not. Hence, one conclusion that can be drawn is that the two low intensity peaks of the R(4) *normal* spectrum are mostly *rogue* in character at high electric fields, while the other two more intense *rogue* peaks are mostly *normal* in character.

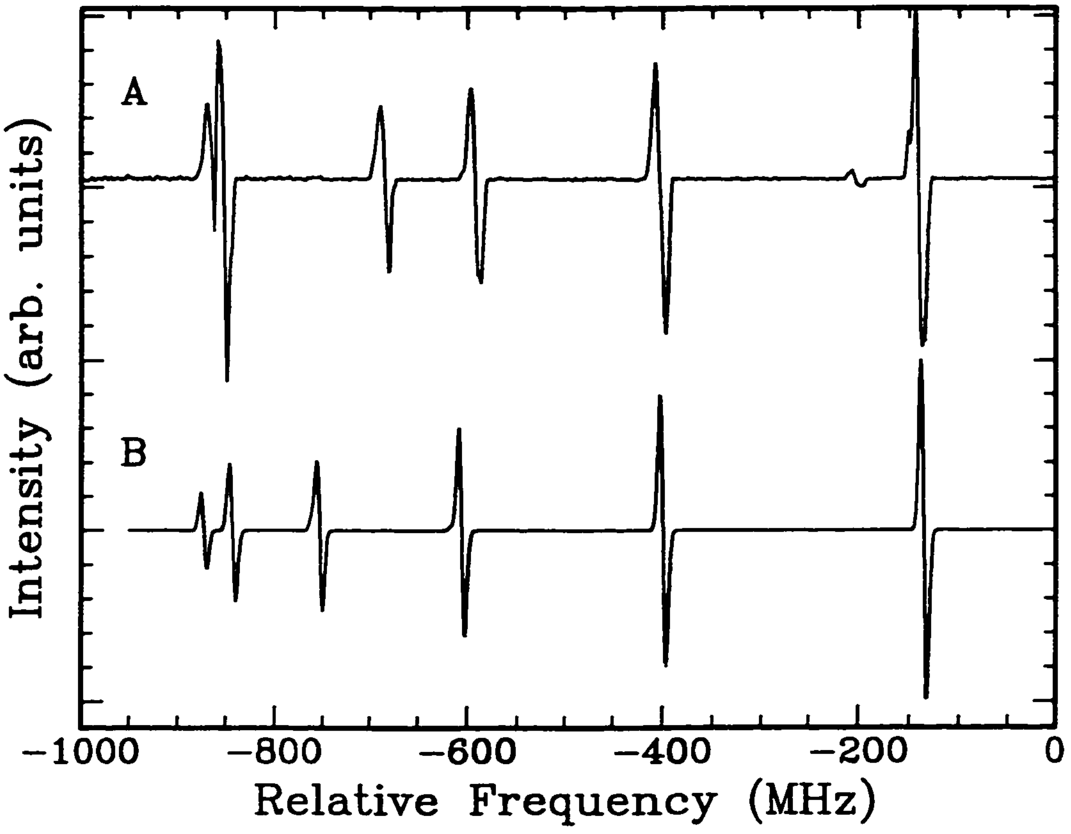

Figure 6.24: Comparison of the measured (**A**) and calculated (**B**) R(4) Stark field perturbed spectrum at 171.0 kV/cm. The line width used in the calculation was 7 MHz. The "best fit" was produced with $\alpha = 23.53Å^3$ and $\Delta\alpha = 71.3Å^3$.

The intensity borrowing exhibited by the *rogue* peaks can also be demonstrated with the state coupling model. In particular, the ratio of the *rogue* and *normal* peak intensities plotted earlier for the R(3) $M = 4 \leftarrow 3$ transition can be calculated with this model. Using the equations for the wave function coefficients, a and b (Equation 6.5) and the previously determined values for the various constants, the intensity ratio a^2/b^2 can be calculated as a function of electric field (F). This can then be converted to a function of the difference in *rogue* and *normal* peak positions by using Equation 6.3. Despite the difficulty in obtaining reliable peak intensities (via peak areas), the data fits the model very well (Figure 6.25).

Earlier the assumption was made that the three *rogue* ro-vibrational transitions observed belonged to same vibrational band. This was not an unreasonable assumption. Had there been more than one *rogue* band involved, more *rogue* ro-vibrational transitions should have been detected. The rotational constant of highly excited vibrational states of acetylene in this region of the spectrum ranges from 1.153 cm^{-1} to about 1.164 cm^{-1} [78]. Using these as the values as the upper and lower limits of the rotational constants in this spectral region, it is not possible for two or more *rogue* bands to be present without there being any observation of other ro-vibrational transitions belonging to these bands.

Using the data from Table 6.6 together with the known positions of the *normal* ro-vibrational transitions, one can calculate an approximate value of the *rogue* band's rotational constant, $B_R = 1.165\ \text{cm}^{-1}$. Since the rotational constant is proportional

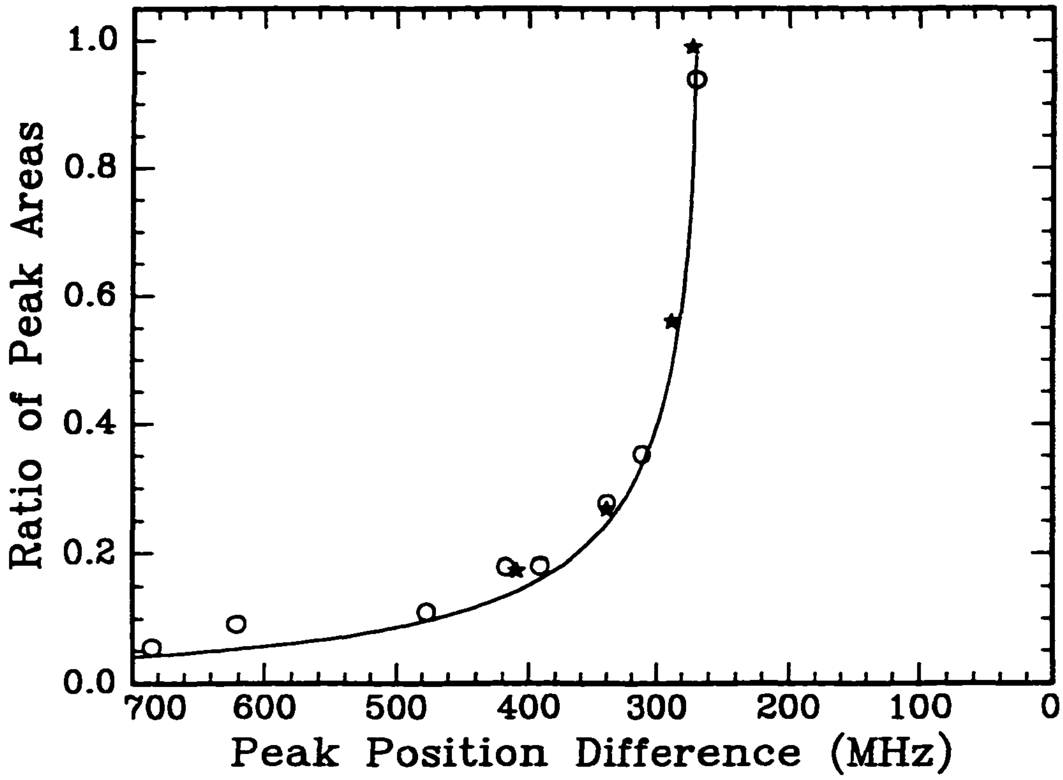

Figure 6.25: The ratio of the *rogue* to *normal* peak areas for the first *rogue/normal* pair of peaks ($M = 4 \leftarrow 3$ transition) is plotted against the difference in peak positions. The circles depict the *rogue* peaks on the red side of the R(3) zero field position and the stars represent the *rogue* peaks on the high frequency side. The solid line is a plot of a^2/b^2 using Equations 6.3 and 6.5 with $C = 135$ MHz, $W_N^0 = 0$, $W_R^0 = -5350$, $t_R = 0.3634$ MHz/kV^2 and $t_N = 4.293 \times 10^{-4}$ MHz/kV^2.

Table 6.6: Data extracted from the *rogue* transitions. † see page 132.

J_{upper}	(α_{vJ}) (Å^3)	$\Delta\alpha_{vJ}$ (Å^3)	Coupling Constant (MHz)	$W_R^0 - W_N^0$ (MHz)
4†	-184	1013	135	-5350± 110
5	Not	Available	205	228
6	61.71±0.29	128.4±2.1	45.8±1.6	1600±40

to the inverse of the moment of inertia for the molecule ($B = \hbar/[4\pi cI]$), it can be concluded that the molecule is more compact in the *rogue* state than in the normal state. Adding a significant number of quanta to the bending vibrations of acetylene could alter the geometry sufficiently to cause such a change in the rotational constant. In fact, since the asymmetric stretch, ν_3 (3287 cm^{-1}), is approximately 5 times higher in frequency than the average bending vibration (ν_4 = 612 cm^{-1} and ν_5 = 729 cm^{-1}) [3], substituting only two quanta of asymmetric stretch vibration would require about 10 quanta of bending vibration in return. This is the basis of Kellman's resonance pseudoquantum number n_r (see Chapter 5 page 77 and also references [82, 83]). Not only would this distort the molecule, it would render the band nearly undetectable by direct infrared transition, since the intensity of an overtone band often drops by approximately an order of magnitude with each additional quantum of vibrational excitation [92]. The fact that the *rogue* peaks lacked the intensity to be easily observed at large frequency separations from the *normal* peak positions seems to support this hypothesis.

Finally, the same analysis used to describe the *ungerade-gerade* state coupling of the 04^- and 04^+ states was applied to polarisability data of the $1|03^-$ state in Table 6.1. The rotational constant for both states ($1|03^-$ and $1|03^+$) was assumed to be 1.15291 cm^{-1} [78]. The results of fitting the polarisability data of $1|03^-$ to Equation 5.10 (page 88) are $\alpha_{1|03^-} = 3.5\pm0.3$ $\AA^3$, $\Delta\alpha_{1|03^-} = 5.6\pm1.8$ $\AA^3$, $\mu = 0.0551\pm0.018$ Debye and $\Theta = -11.88\pm0.22$ cm^{-1} (See Figure 6.26). The errors (given as 2σ) are about an order of magnitude larger than those produced by the fit to the data from the $\nu_1 + 3\nu_3$ band, and the difference in band origins does not compare well with the results from Child and Halonen (17.1 cm^{-1}) [11]. The solid line depicting the fit to the data in Figure 6.26 was not calculated between $J = 0$ and $J = 1$, since Equation 5.10 contains a singularity at $J = 0.5$. The fit to Equation 5.10 does correctly predict the value for $J = 0$ when calculated at that data point. The data point for R(4) (J = 5) was not included in the fit, but superimposed afterwards for comparison. Although the J = 5 data point is not the result of a fit of the entire Stark field split spectrum (at 171.0 kV/cm), it compares well with the results of the *ungerade-gerade* state coupling calculations. This may also be an indication that the R(4) Stark field perturbed spectrum is slowly becoming more *normal* at the higher electric fields.

A plot of the components of the $1|03^{-1}$ polarisability tensor shows that, in contrast to 04^-, only the parallel component (stars) is significantly enhanced (Figure 6.27). This is expected, since the transition dipole connecting $1|03^-$ and $1|03^+$ is along the molecular symmetry axis.

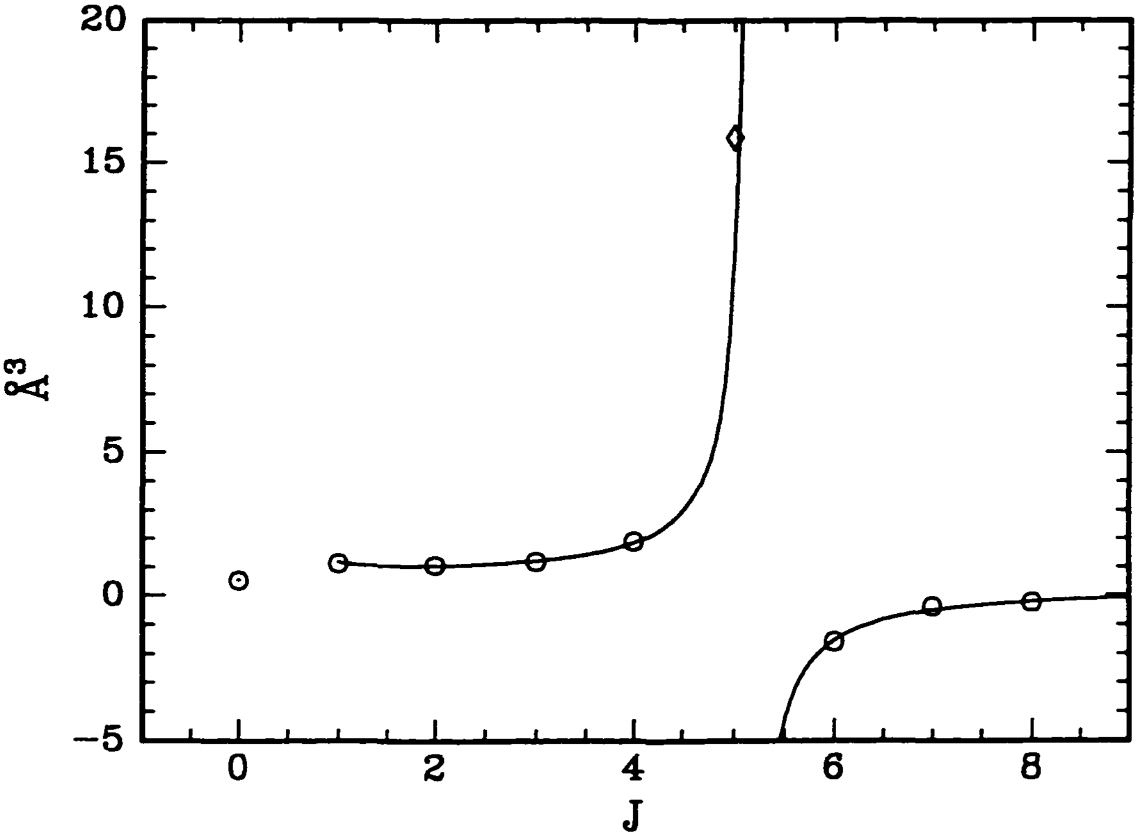

Figure 6.26: The result of the non-linear least-squares fit of Equation 5.10 to the experimental data for the M = 0 levels only. The o represent the left-hand-side of Equation 5.10 calculated from the experimental values obtained for α_{vJ} and $\Delta\alpha_{vJ}$. The data for J = 5 (estimated from the high electric field Stark perturbed spectrum) was not included in the fit and was superimposed afterwards. It is represented by the ◇.

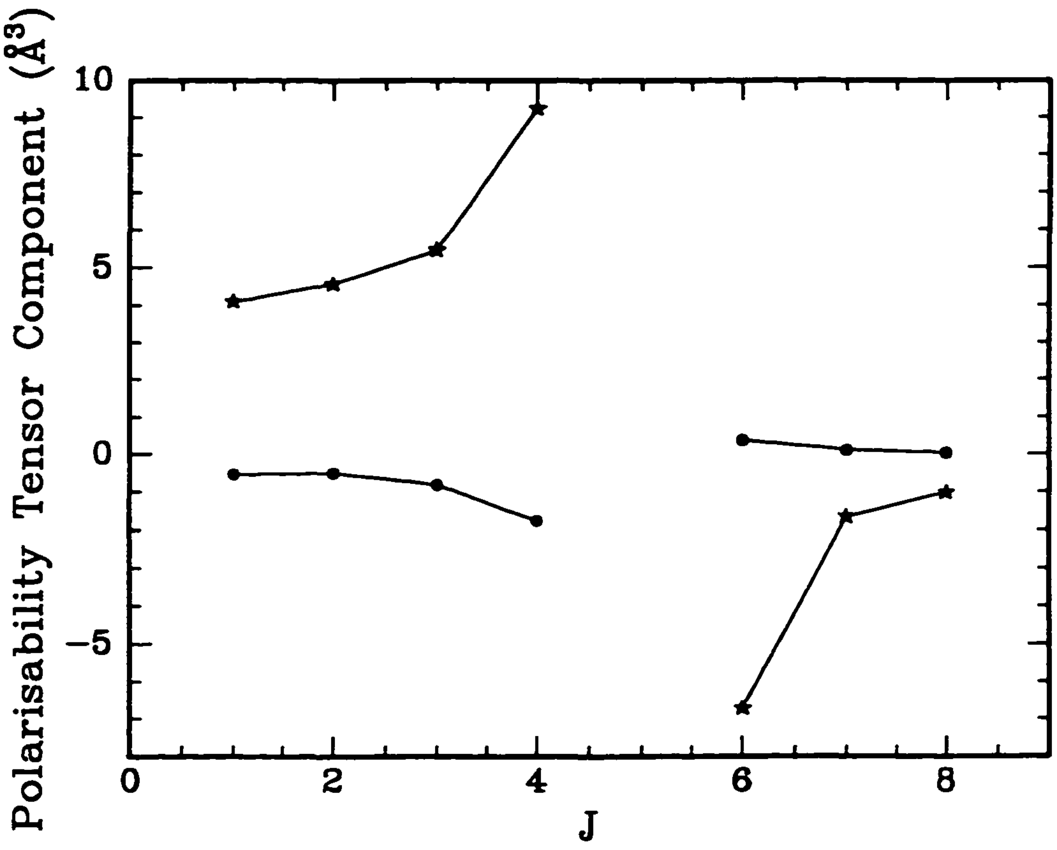

Figure 6.27: The components of the polarisability tensor are plotted here as a function of J. The solid circles depict the perpendicular components ($\alpha_\perp$) and the stars are the parallel components ($\alpha_\parallel$). In contrast to the results of 04^-, only the parallel component of the polarisability exhibits significant enhancement. The $J = 0$ data point could not be calculated since a measured value of the polarisability anisotropy is not available for $J = 0$.

Chapter 7

Summary and Conclusions

This thesis reports results on a variety of experiments, ranging from the design of a new instrument, to the complex coupling of highly excited vibrational states of acetylene. This chapter will attempt to summarise and reflect upon these results.

The work designing and evaluating the laser power build-up cavity was not intended to be one of the main experiments, but it turned out to be far more time-consuming than all of the other experiments combined. The initial goal was to design a very high gain optical device using a pair of 99.998% reflectivity mirrors held apart by two separate mirror mounts contained within a massive assembly. The heavy assembly was designed to be free of external vibration, yet the resultant BUC was plagued with instabilities. With the earlier design, it was impossible to obtain a BUC spectrum showing mode structure as clear as that depicted in Figure 3.4 (page 46), instead a "forest" of "fine structure" was seen. This "fine structure" turned out to be a myriad of higher order transverse modes: a direct result of the instability of the BUC. Over time, it was learned it was far more important that the mirrors be held vibration-free with respect to each other, rather than isolating them from the rest of the molecular beam apparatus. Hence, the "sandwiched" arrangement was devised.

It is possible that the current BUC is near the performance limit for such a device. The early design had, ideally, a potential gain of 50000 compared to the mere 2000 of the present system; the latter produces a real gain of less than 1000. In retrospect, the "heating" effect (Section 3.5.1, page 48) for the earlier high gain system would have been phenomenal and it is unlikely the design would have ever succeeded. Recent reports of "cavity ring-down" experiments have opened up new avenues for these seemingly uncontrollable BUCs [105–107]. These experiments require unstable BUCs with a very high mode density, similar to the early designs of the present BUC. The BUC is then illuminated with a pulsed laser and the cavity fluorescence is monitored after each laser pulse. The data collected at each laser frequency are fit to an exponential decay and the spectrum is then re-created by computer. High gain, unstable BUCs seem to yield the best results, but the resolution of such an experiment is typically limited by the resolution of the pulsed laser (approximately 0.05 $\text{cm}^{-1} \simeq$ 1500MHz) and cannot compare with that of the current system (5 MHz).

The experiment with hydrogen fluoride was the first completed and it had two purposes. The first was to measure the electric dipole moment for comparison with the theory derived from the lower vibrational state experimental data. This was then to be followed by measurements of the HF-Ar van der Waals dimer dipole moment, once a suitable multipass device had been designed. Due to the time spent designing the BUC, this second goal was made obsolete by Klemperer and Chang [108]. However, experimental determination of the dipole moments of still higher vibrational states of hydrogen fluoride seems advisable. The $v = 3$ dipole moment measured here (1.9614 Debye) seems to follow the model by Sileo and Cool (using the correct value for μ_e) [64] and it would seem wise to test the theory further. The most obvious experiment is to use a dye laser working on R6G to interrogate $v = 4$. If instead the Ti:Sapphire laser were intra-cavity doubled, it would be possible to reach the $v = 7$ energy level. The current BUC should provide satisfactory signal to noise for the successful implementation of such an experiment and the results would be a far more rigorous test of the current theoretical models.

The analysis of the Stark split vibrational overtone spectra of acetylene has proven to be far more of a challenge than originally expected. The somewhat deceptive simple geometry of the molecule did not appear to forecast the interesting results reported in Chapters 5 and 6. Closer examination of the near infrared region of the acetylene spectrum reveals a great number of vibrational states and interaction among them would seem to be inevitable. Nonetheless, the coupling of *ungerade* and *gerade* vibrational states would not have seemed predictable. The fact that the interaction between the 04^- and 04^+ states was mediated by the Stark electric field allowed for the unique opportunity to "turn off" the coupling by removing the Stark electric field. The $\nu_1 + 3\nu_3$ band itself has been thoroughly analysed in the past [9, 86], yet the band origin of its "twin" *gerade* (dark) band, $4\nu_3$, could only be determined by calculation [11]. The application of the Stark field provided a means to indirectly measure the origin of $4\nu_3$ band, placing it 4.133 cm^{-1} below the $\nu_1 + 3\nu_3$ band origin.

The coupling of *ungerade* states of acetylene has been the subject of much discussion in the literature [2, 95, 101, 109]. The current measurements of the $\nu_2 + 3\nu_3$ band have resulted in the observation of new transitions (*rogue* peaks), which will hopefully aid future analysis of the state-to-state interactions of acetylene. Using the results presented in this thesis for the $|0130^00^0\rangle$ state and results of their own measurements [95] Orr and Milce have carried out a series of calculations *à la* Herman *et al.* [2] that suggest the $|0306^03^1\rangle$ state is responsible for the *rogue* peaks [110]. They have amended the model to include the perturbations introduced by the Stark field, such as the Stark field mediated mixing of the *ungerade* $|0306^03^1\rangle$ and the *gerade* $|0305^{-3}4^4\rangle$ states. They have concluded that the $|0130^00^0\rangle$ and $|0306^03^1\rangle$ states are strongly coupled via Coriolis resonances. The unusual "UV brightness" of the $J = 5$ level of $|0130^00^0\rangle$ that Orr and Milce noted during the course of their investigations [95] is likely due to Coriolis coupling with the $J = 5$ level of $|0306^03^1\rangle$ which contains significant excitation of the *trans*-bending vibration; a requirement for a strong UV transition to the *trans*-bent first electronic ($\tilde{A}$) state of acetylene. The results of their calculations have been very promising and their model predicts the behaviour of the R(3) and R(5) Stark split spectra quite well. However, it has still not provided a satisfactory picture of the ***normal-rogue*** interaction seen in the R(4) Stark split spectra.

If the *rogue* vibrational state is indeed the $|0306^0 3^1\rangle$ state (Π_u symmetry), then the second order Stark equation used here to extract polarisability data from the *rogue* transitions is not correct. This equation was derived for Σ–Σ (parallel) transitions rather than Σ–Π (perpendicular) transitions. Orr and Milce are making further modifications to the state coupling model to include a perpendicular type second order Stark effect.

In light of the strongly perturbed Stark split spectra of the $\nu_2 + 3\nu_3$ band it seems advisable to re-examine the data for the $\nu_1 + 3\nu_3$ band. Specifically, the polarisability data for the $J = 5$ level (Table 5.1, page 84) seems somewhat anomalous. The Stark perturbed spectrum of the $\nu_1 + 3\nu_3$ R(4) transition seemed to oppose the trend of a decreasing $\Delta\alpha$ and split much more than expected. This similarity with the Stark perturbed spectrum of the $\nu_2 + 3\nu_3$ R(4) transition (sudden large splitting) would seem to suggest a similar phenomenon was responsible, albeit to a lesser degree.

The highly vibrationally excited states of small molecules can offer a great deal of information in the never ending quest to fully understand molecular dynamics. Diatomics, with generally simple spectra, provide the first step in testing the limits of our ability to predict molecular characteristics as a function of excitation. As the number of atoms is increased to three or four, the complexity of the vibrational overtone spectra increases dramatically, but the molecules are still small enough to be modelled theoretically. These molecules are the "stepping stones" to the much larger, chemically interesting species that defy a detailed spectral analysis. However, in order to achieve a better understanding of molecular overtones, high resolution and high sensitivity instruments, such as the one described in this thesis, are required. There is still much work to be done.

Bibliography

[1] V.S. Letokhov, **Laser Spectroscopy of Highly Vibrationally Excited Molecules**, (Adam Hilger, New York, 1989).

[2] M.A. Temsamani and M. Herman, *Journal of Chemical Physics*, **102**(16) (1995) 6371–6384.

[3] G. Herzberg, **Infrared and Raman Spectra**, (Van Nostrand Reinhold Company, New York, 1945) pp. 288–291.

[4] G. Stella, J. Gelfand and W.H. Smith, *Chemical Physics Letters*, **39**(1) (1976) 146–149.

[5] K.V.Reddy, D.F. Heller and M.J. Berry, *Journal of Chemical Physics*, **76**(6) (1982) 2814–2837.

[6] J. Röper, A. Neubrand and P. Hess, *Journal of Applied Physics*, **64**(6) (1988) 2838–2846.

[7] B.H. Henry and M.G. Sowa, *Progress in Analytical Spectroscopy*, **12** (1989)

349–368.

[8] Z. Lin, K. Boraas and J.P. Reilly, *Journal Molecular Spectroscopy*, **156** (1992) 147–153.

[9] L. Halonen and X. Zhan, *Journal of Molecular Spectroscopy*, **160** (1993) 464–470.

[10] B.R. Henry, *Accounts of Chemical Research*, **10** (1977) 207–213.

[11] M.S. Child, and L. Halonen, in: **Advances in Chemical Physics**, Volume 57, (I. Prigogine and Stuart A. Rice, editors), (John Wiley and Sons, New York, 1984) pp. 1–58.

[12] R. Mecke and R. Ziegler, *Zeitschrift für Physik*, **101** (1936) 405–417.

[13] D.W. Chandler, W.E. Farneth and R.N. Zare, *Journal of Chemical Physics*, **77**(9) (1982) 4447–4458.

[14] I.M. Mills at "International Conference on Near Infrared Spectroscopy", *Making Light Work : Advances in Near Infrared Spectroscopy* Title :**Understanding spectra of highly excited vibrational states**, (Weinheim, Germany, VCH publisher, 1992) pp. 67–80.

[15] R.G. Bray and M.J. Berry, *Journal of Chemical Physics*, **71**(12) (1979) 4909–4922.

[16] M.L. Sage and J. Jortner, *Chemical Physics Letters*, **79**(1) (1981) 9–14.

[17] M.G. Sowa, B.R. Henry and Y. Mizugai, *Journal of Physical Chemistry*, **95** (1991) 7659–7664.

[18] M.D. Kikar, J.E. Baggott and F.F. Crim, *Journal of Chemical Physics*, **90**(11) (1989) 6266–6274.

[19] A.D. Buckingham, **MTP International Review of Science, Physical Chemistry, Series One, Spectroscopy**, Volume 3, (D.A. Ramsay, editor) (Butterworths, London, 1972) pp. 73–117.

[20] J.O. Hirschfelder, ed., **Advances in Chemical Physics: Intermolecular Forces**, Volume 12, (Interscience, New York, 1967).

[21] M. Rigby, E.B. Smith, W.A. Wakeham and G.C. Maitland, **The Forces Between Molecules**, (Oxford Science Publications, New York, 1986).

[22] H-J. Werner and P. Rosmus, *Journal of Chemical Physics*, **73**(5) (1980) 2319–2328.

[23] M.D. Marshall, K.C. Izgi and J.S. Muenter, *Journal of Chemical Physics*, **107**(4) (1997) 1037–1044.

[24] J.A. Dodd, A.M. Smith and W. Klemperer, *Journal of Chemical Physics*, **88** (1988) 15–19.

[25] K. Nakagawa, Y. Moriwaki and T. Shimizu, *Optics Letters*, **14**(10) (1989) 488–490.

[26] K. Boraas, D.F. De Boer, Z. Lin, and J.P. Reilly, *Journal of Chemical Physics*, **99**(2) (1993) 1429–1432.

[27] G. Herzberg, **Molecular Spectra and Molecular Structure III: Electronic Spectra and Electronic Structure of Polyatomic Molecules**, (Van Nostrand Reinhold Company, New York, 1966).

[28] E. Fermi, *Zeitschrift für Physik*, **71** (1931) 250–259.

[29] J.R. Lombardi and K-T. Huang, *Journal of Chemical Physics*, **55** (1971) 4072–4076.

[30] C.H. Townes and A.L. Schawlow, **Microwave Spectroscopy** (McGraw–Hill, New York, 1955), pp. 38, 96, 248–283.

[31] M.P. Bogaard and B.J. Orr, **MTP International Review of Science, Physical Chemistry, Series Two**, Volume 2, (A. D. Buckingham, editor) (Butterworths, London, 1975) pp. 149–194.

[32] M. Brieger, *Chemical Physics*, **89** (1984) 275–295.

[33] D.M. Bishop, *Reviews of Modern Physics*, **62**(2) (1990) 343–374.

[34] P.N. Butcher and D. Cotter, **Cambridge Studies in Modern Optics : 9 "The Elements of Nonlinear Optics**, (Cambridge University Press, Cambridge, 1990).

[35] J.D. Graybeal, **Molecular Spectroscopy**, (McGraw Hill, New York, 1988).

[36] L.H. Scharpen, J.S. Muenter and V.W. Laurie, *Journal of Chemical Physics*, **46**(6) (1967) 2431–2434.

[37] A.R. Edmonds, **Angular Momentum in Quantum Mechanics**, (Princteon University Press, Princeton, 1960).

[38] T.E. Gough, B.J. Orr and G. Scoles, *Journal Molecular Spectroscopy*, **99** (1983) 143–158.

[39] J.O. Hirschfelder, C.F. Curtiss and R.B. Bird, **Molecular Theory of Gases and Liquids**, (John Wiley & Sons, New York, 1967).

[40] G.R. Alms, A.K. Burnham and W.H. Flygare, *Journal of Chemical Physics*, **63**(8) (1975) 3321–3326.

[41] M.P. Bogaard, A.D. Buckingham, R.K. Pierens and A.H. White, *Journal of the Chemical Society: Transactions of the Faraday Society*, **I 74** (1978) 3008–3015.

[42] D.H. Whiffen, *Transactions of the Faraday Society*, **54** (1958) 327–329.

[43] G. Scoles, **Atomic and Molecular Beam Methods**, Volume I, (Oxford University Press, New York, 1988), pp. 254–273.

[44] J-P. Chevillard, J-Y. Mandin, J-M. Flaud and C. Camy-Peyret, *Journal of Molecular Spectroscopy*, **116** (1986) 167–190.

[45] J-P. Chevillard, J-Y. Mandin, J-M. Flaud and C. Camy-Peyret, *Canadian Journal of Physics*, **67** (1989) 1065–1084.

[46] B.C. Smith, and J.S. Winn, *Journal of Chemical Physics*, **89**(8) (1988) 4638–4645.

[47] B.C. Smith, and J.S. Winn, *Journal of Chemical Physics*, **94**(6) (1991) 4120–4130.

[48] K. Boraas, Z. Lin and J.P. Reilly, *Journal of Chemical Physics*, **100** (1994) 7916–7927.

[49] Huan-C. Chang and W. Klemperer, *Journal of Chemical Physics*, **98**(4) (1992) 2497–2506.

[50] S.L. Gilbert and C.E. Wieman, *Physical Reviews A*, **34** (1986) 792–803.

[51] Wan-Ü L. Brillet and A. Gallagher, *Physical Reviews A*, **22** (1980) 1012–1017.

[52] E. Riedle and H.J. Neusser, *Journal of Chemical Physics*, **80**(10) (1984) 4686–4693.

[53] C. Douketis, Dissertation (PhD), University of Indiana, Department of Chemistry (1989).

[54] C.E. Tanner, B.P. Masterson and C.E. Wieman, *Optics Letters*, **13** (1988) 357–359.

[55] A.E. Siegman, **Lasers**, (University Science Books, Mill Valley, California, 1986).

[56] R. Arndt, *Journal of Applied Physics*, **36**(8) (1965) 2522–2524.

[57] J. Reid and D. Labrie, *Applied Physics B*, **26** (1981) 203–210.

[58] J.C. Polanyi, *Journal of Chemical Physics*, **34**(1) (1961) 347–348.

[59] J.C. Polanyi, *Applied Optics, Supplement 2 of Chemical Lasers*, (1965) 109–127.

[60] J.C. Polanyi, *Applied Optics,* **10**(8) (1971) 1717–1724.

[61] J.A. Coxon and P.G. Hajigeorgiou, *Journal of Molecular Spectroscopy,* **142** (1990) 254–278.

[62] W.T. Zemke, W.C. Stwalley, J.A. Coxon and P.G. Hajigeorgiou, *Chemical Physics Letters*, **177**(4,5) (1991) 412–418.

[63] W.T. Zemke, W.C. Stwalley, S.R. Langhoff, G.L. Valderrama and M.J. Berry, *Journal of Chemical Physics*, **95**(11) (1991) 7846–7853.

[64] R.N. Sileo and T.A. Cool, *Journal of Chemical Physics*, **65**(1) (1976) 117–133.

[65] C.W. Bauschlicher Jr., S.R. Langhoff, S.P. Walch, P.R. Taylor, and R.L. Raffe, *Journal Chemical Physics*, **88**(3) (1988) 1743–1751.

[66] F. Sim, D.R. Salahub and S. Chin, *International Journal of Quantum Chemistry*, **43** (1992) 463–479.

[67] J.S. Muenter and W. Klemperer, *Journal of Chemical Physics*, **52**(12) (1970) 6033–6037.

[68] J.M. Bass, R.L. DeLeon and J.S. Muenter, *Journal of Chemical Physics*, **86**(8) (1987) 4305–4312.

[69] A.S. Pine, A. Fried and J.W. Elkins, *Journal of Molecular Spectroscopy*, **109** (1985) 30–45.

[70] J.F. Ogilvie, *Journal of Physics B: Atomic, Molecular and Optical Physics*, **21** (1988) 1663–1671.

[71] E.S. Fishburne and K.N. Rao, *Journal of Molecular Spectroscopy*, **19** (1966) 290–293.

[72] H.G. Hedderich, K. Walker and P.F. Bernath, *Journal of Molecular Spectroscopy*, **149** (1991) 314–316.

[73] J.S. Muenter, *Journal of Chemical Physics*, **56**(11) (1972) 5409–5412.

[74] T.E. Gough, R.E. Miller and G. Scoles, *Faraday Discussions of the Chemical Society*, **71** (1981) 77–85.

[75] R.M. Herman and S. Short, *Journal of Chemical Physics*, **48**(3) (1968) 1266–1272.

[76] J.L. Dunham, *Physical Reviews*, **41** (1932) 721–731.

[77] J. Sakai and M. Katayama, *Journal of Molecular Spectroscopy*, **154** (1992) 277–287.

[78] X. Zhan, O. Vaittinen and L. Halonen, *Journal of Molecular Spectroscopy*, **160** (1993) 172–180.

[79] B.T. Darling and D.M. Dennison, *Physical Review*, **57** (1940) 128–139.

[80] H.C. Allen and Paul.C. Cross, **Molecular Vib–Rotors**, (John Wiley and Sons, New York, 1963), pp. 48–50.

[81] D. Papoušek and M.R. Aliev, **Molecular Vibrational–Rotational Spectra**, (Academia, Prague, 1982).

[82] M.E. Kellman, *Journal of Chemical Physics*, **93**(9) (1990) 6630–6635.

[83] M.E. Kellman and G. Chen, *Journal of Chemical Physics*, **95**(11) (1991) 8671–8672.

[84] D.M. Jonas, S.A.B. Solina, B. Rajaram, R.J. Silbey and R. Field, *Journal of Chemical Physics*, **97**(4) (1992) 2813–2816.

[85] G.T. Fraser and B.H. Pate, *Journal of Chemical Physics*, **100** (1994) 6210–6220.

[86] K. Hedfeld and P. Lueg, *Zeitschrift für Physik*, **77** (1932) 446–458.

[87] J. Vander Auwera, D. Hurtmans, M. Carleer, and M. Herman, *Journal of Molecular Spectroscopy*, **157** (1993) 337–357.

[88] A. Kumar and W.J. Meath, *Molecular Physics*, **75**(2) (1992) 311-324.

[89] H.E. Watson and K.L. Ramaswamy, *Proceedings of the Royal Society of London*, **A 156** (1936) 144–157.

[90] H. Lowery, *Proceedings of the Royal Society of London*, **A 133** (1931) 188–207.

[91] J. Tausz and U.G. Hornung, *Zeitschrift für Technische Physik*, **8** (1927) 338–355.

[92] K.N. Rao, **Molecular Spectroscopy: Modern Research**, Volume 2, (Academic Press, New York, 1976) pp. 165–227.

[93] A.D. Buckingham, M.P. Bogaard, D.A. Dunmur, C.P. Hobbs and B.J. Orr, *Transactions of the Faraday Society*, **66** (1970) 1548–1553.

[94] G.W. Funke, *Zeitschrift für Physik*, **104** (1937) 169–187.

[95] A.P. Milce and B.J. Orr, *Journal of Chemical Physics*, **104**(17) (1996) 6423–6434.

[96] A.P. Milce and B.J. Orr, *Journal of Chemical Physics*, **106**(9) (1997) 3592–3606.

[97] A.L. Utz, J.D. Tobiason, E. Carrasquillo, M.D. Fritz and F.F. Crim, *Journal of Chemical Physics*, **97**(1) (1992) 389–396.

[98] A.L. Utz, J.D. Tobiason and F.F. Crim, *Journal of Chemical Physics*, **97**(10) (1992) 7437–7447.

[99] A.L. Utz, J.D. Tobiason, E. Carrasquillo, L.J. Sanders and F.F. Crim, *Journal of Chemical Physics*, **98**(4) (1993) 2742–2753.

[100] A.L. Utz, J.D. Tobiason, E. Carrasquillo and F.F. Crim, *Chemical Physics*, **190** (1995) 311–325.

[101] D.M. Jonas, S.A.B. Solina, B. Rajaram, R.J. Silbey, R. Field, K. Yamanouchi and S. Tsuchiya, *Journal of Chemical Physics*, **99**(10) (1993) 7350–7370.

[102] J.P. Pique, Y.M. Engel, R.D. Levine, Y. Chen, R. Field and J.L. Kinsey, *Journal of Chemical Physics*, **88** (1988) 5972–5974.

[103] Y. Ohsugi and N. Ohashi, *Journal of Molecular Spectroscopy*, **131** (1988) 215–222.

[104] G. Herzberg, **Spectra of Diatomic Molecules**, Second Edition, (Van Nostrand Reinhold Company, New York, 1950) pp. 295–298.

[105] A. O'Keefe and D.A.G. Deacon, *Review of Scientific Instruments*, **59**(12) (1988) 2544–2551.

[106] A. O'Keefe, J.J. Scherer, A.L. Cooksy, R. Sheeks, J. Heath and R.J. Saykally, *Chemical Physics Letters*, **172**(3,4) (1990) 214–218.

[107] G. Meijer, M.G.H. Boogaarts, R.T. Jongma, D.H. Parker and A.M. Wodtke, *Chemical Physics Letters*, **217**(1,2) (1994) 112–116.

[108] H-C. Chang and W. Klemperer, *Journal of Chemical Physics*, **98**(4) (1993) 2497–2506.

[109] G.J. Scherer, K.K. Lehmann and W. Klemperer, *Journal of Chemical Physics*, **78**(6) (1983) 2817–2832.

[110] A.P. Milce and B.J. Orr; School of Chemistry, McQuarrie University, Sydney Australia; Private Communication (1996–1997).